Application of the chiral SMS potential to selected electromagnetic processes in two- and three-nucleon systems

Vitalii Urbanevych

CONTENTS

Abstract

Lorem ipsum dolor sit amet, consectetur adipiscing elit, sed do eiusmod tempor incididunt ut labore et dolore magna aliqua. Ut enim ad minim veniam, quis nostrud exercitation ullamco laboris nisi ut aliquip ex ea commodo consequat. Duis aute irure dolor in reprehenderit in voluptate velit esse cillum dolore eu fugiat nulla pariatur. Excepteur sint occaecat cupidatat non proident, sunt in culpa qui officia deserunt mollit anim id est laborum.

CHAPTER 1

INTRODUCTION

Why we study few nucleon systems

The study of light nuclei and their reactions has been serving as an easy way to investigate particles in nuclei and the forces between them for decades. A convenient way to proceed may be to study the interaction of a nucleus with other nuclei, particles, or electroweak probes such as electrons, photons, muons, pions, neutrinos, and hyperons. In most cases, study of elastic or inelastic scattering is possible. This can be done either theoretically or by performing relevant experiments to test if the theory works. It should be taken into account that nuclear interactions may be caused by different fundamental forces, including strong, weak, or electromagnetic interactions. This depends on the type of particle being scattered and the target of the reaction and requires different theoretical approaches. Of course gravitational force is also in the game but due to its weekness it is usually omitted in the nuclear physics.

In the past many experimental efforts have been undertaken and experimentalists have been interested in electromagnetic reactions involving light nuclei for decades. There are experimental data from the second half of 20th century (e.g. [?, ?, ?, ?]) which are still useful for comparing theoretical predictions with experimental measurements. There are several facilities providing sources of gamma rays (both low- and high-energy) and other particles that have been operating for decades and still enable experiments to be conducted. Let us mention here such facilities as TUNL with HIγS [?, ?], MAMI [?].

To accurately describe nuclear reactions, two important components of the Hamiltonian must be considered. They are nuclear interactions and nuclear currents. First of all, various nuclear forces may act on the particles.

The strong nuclear force acts inside the nuclei and, among others, bound neutrons and protons together. The description of strong interactions is extremely difficult as it deals not only with the nucleons themselves, but also with their constituents: quarks and gluons. Quantum chromodynamics (QCD) is a modern theory describing strong interactions, but, at the moment, it is not applicable at low energies (e.a. at $Q^2 \lesssim 1 GeV^2$). In such situation various approaches are emerging. The most advanced are the chiral effective theory and lattice calculation [?, ?, ?]. In this work we will use results of the first approach and corresponding model is described in Sec. 2.

Study of three- (and more) nucleon systems showed that the strong two-nucleon (2N) force is not efficient in describing $N > 2$ systems, thus a 3N force was introduced. The

first applications of such a force showed that it brings a sizable contribution to observables and cannot be ignored [?]. The contribution of the 3NF can be examined by comparing binding energies of light nuclei calculated with and without this part of Hamiltonian with respect to experimental values.

For example, the binding energy for ^{3}H calculated with the Argonne V18 (AV18) 2N potential without 3NF amounts to $E_b(^3\text{H}) = -7.628$ MeV [?]. There are different models that might add a 3NF contribution to AV18 (or other potentials). Using the Tucson-Melbourne (TM) model [?] results in $E_b(^3\text{H}) = -8.478$ MeV, and Urbana IX [?] 3NF provides us with $E_b(^3\text{H}) = -8.484$ MeV. Looking at the experimental value $E_b(^3\text{H}) = -8.482$ MeV, it is clear that the 3NF contribution makes the prediction much closer to the measurement. Nevertheless, the parameters of the UrbanaIX 3NF were fitted to the experimental value for ^{3}H, so there is no surprise in good agreement.

However one can also check the binding energy for other nuclei, which were not used for the fitting. The 2NF binding energy for ^{3}He (calculated with AV18) is $E_b(^3\text{He}) = -6.917$ MeV. TM contribution makes it $E_b(^3\text{He}) = -7.706$ MeV, Urbana IX gives $E_b(^3\text{He}) = -7.739$ MeV, while the experimental value is $E_b(^3\text{He}) = -7.718$ MeV. One can see the importance of 3NF contribution also for the α-particle's (^{4}He) binding energy: AV18 alone gives $E_b(^4\text{He}) = -24.25$ MeV, while AV18 + TM leads to -28.84 MeV, AV18 + Urbana IX delivers $E_b(^4\text{He}) = -28.50$ MeV, and the experimental value is -28.30 MeV [?].

Whereas the first applications included only early simplified "realistic" 3N potential, the latter investigations, based on more advanced models, fully confirmed this statements [?, ?]. Within new models the four-nucleon (4N) interaction was constructed to improve description of ^{4}He [?]. Broader discussion of nuclear forces used in this thesis is given below.

Electromagnetic force appears between charged particles like protons, electrons or pions. That force acts also between charged particles and photons, so in photon- and electron- scatterings on the nuclei it is a necessary component of a description. However, electromagneticinteraction between particles manifests only at very low energies or for specific kinematic configurations with two photons having approximately equal momenta. Thus it rather is being skipped in lowes-order analysis.

The main conribution of electromagnetic interaction to disintegration processes in hand is due to the current's operator describing photon-nucleon vertex. The structure of the electromagnetic current have been investigated in many works by numerous groups [?] but it was H. Arenhövel who performed study of nuclear electromagnetic current in few-nucleon sector. His long-term research, reviewed in [?] demonstrated various theoretical models applied to the deuteron photodisintegration. He analyzed among others a nonrelativistic potential model, a relativistic impulse approximation, and a relativistic meson-exchange model. These models were used to calculate the differential cross section and various polarization observables, which describe the probability of the process occurring at different scattering angles, photon energies spin directions etc.

The calculated cross sections were then compared to experimental data, and it was found that the relativistic meson-exchange model provided the best agreement with the data at photon's energies up to $E_\gamma =\sim 100$ MeV. At higher energies agreement is presented but is getting worse. This model includes the exchange of virtual mesons between the interacting particles, which accounts for the strong and electromagnetic forces between them.

Overall, Arenhövel demonstrated the importance of including both strong interaction

and electromagnetic current operator in a description of the deuteron photodisintegration process, and highlighted the need for accurate theoretical models to interpret experimental data.

The weak force is of great importance in the study of nuclear processes. One of the main roles of the weak force is to mediate *check correction* beta decay, which is a process in which a neutron in a nucleus is converted into a proton, emitting an electron and an antineutrino. This process plays a crucial role in the formation of elements in the universe, as it allows for the conversion of neutron-rich isotopes into more stable, proton-rich isotopes. Additionally, the weak force plays a role in neutrino interactions with matter, which are of great interest in both astrophysics and particle physics. In nuclear physics, weak interactions can also play a role in the decay of unstable nuclei, the production of neutrinos in nuclear reactions, and the scattering of neutrinos off nuclei. The study of weak interactions is therefore an essential component of the overall understanding of nuclear physics and the behavior of matter on the subatomic scale. However, in the thesis we stick up with electromagnetic processes.

Models of strong interaction used in the thesis

In order to model the nuclear potential, physicists often use phenomenological or semi-phenomenological approaches. It allows them to combine theoretical knowledge about the studied processes and experimental findings.

?more Among many of such models, the AV18 [?] force is one of most advanced and therefore is used in current thesis. In order to construct the nucleon-nucleon (NN) force, authors combine one-pion-exchange part with phenomenological one and supplement them by electromagnetic corrections. Free parameters were fitted to the Nijmegen partial-wave analysis of pp and np data [?]. Authors showed, that the AV18 potential delivers good description of nucleon scattering data ($\chi^2/data = 1.08$ for around 4000 pp and np scattering datasets) as well as deuteron properties (estimated binding energy is $2.2247(35)\,\mathrm{MeV}$ vs experimental $2.224\,575(9)\,\mathrm{MeV}$).

Weinberg's idea of using chiral symmetry to describe nuclear interactions at low energies was first introduced in his papers published in 1990 and 1991 [?, ?]. In these papers, Weinberg argued that the low-energy dynamics of nucleons could be described using a chiral Lagrangian, which is the most general Lagrangian consistent with chiral symmetry and its spontaneous breaking. This Lagrangian is expressed in terms of nucleon and pion fields, which are the degrees of freedom that become relevant at low energies.

The chiral Lagrangian is the starting point for the development of the Chiral Effective Field Theory (χEFT), which has become one of the most advanced approaches to low-energy nuclear physics [?]. The use of the χEFT allows (at least in theory) for the calculation of nuclear properties and reactions in a model-independent way. It is also possible to quantify the uncertainties associated with the calculation. One of the key features of the χEFT is that it allows for the construction of a nuclear potential, which can then be used in relevant formalisms, e.g. to solve the Schrödinger equation and to obtain bound and scattering states properties. The accuracy of the potential can be systematically improved by including higher-order terms in the chiral expansion, which leads to a better description of experimental data.

In the χEFT there are two natural scales: so-called soft scale $Q \sim M_\pi$ - the mass of pion and the hard scale - $\Lambda_\chi \sim 0.7\,\mathrm{GeV}$ - the chiral symmetry breaking scale. The ratio between these two scales Q/Λ_χ is being used as an expansion parameter in χEFT with

power ν: $(Q/\Lambda_\chi)^\nu$. [1]

Possibility of deriving nuclear potential is an important feature of χEFT. The potential, as occurs in Lagrangian, is a perturbation expression of the same parameter Q/Λ_χ. Considering so-called irreducible diagrams (which cannot be split by cutting nucleon lines), Weinberg [?, ?] came to the expression for the powers ν_W of such diagrams

$$\nu_W = 4 - A - 2C + 2L + \sum_i \Delta_i, \tag{1.1}$$

where i specifies a vertex number and

$$\Delta_i \equiv d_i + \frac{n_i}{2} - 2. \tag{1.2}$$

In Eq. (1.1) C is a number of pieces which are connected, L - the number of loops in the graph and A is a number of nucleons in the diagram. In Eq. (1.2) n_i is a number of nucleon field operators and d_i - the number of insertions (or derivatives) of M_π.

The further analysis of Eq. (1.1) revealed some problems which occur for particular values of parameters in the equation, namely negative values of ν_W are possible while the order has to take integer values from 0 to infinity. In order to deal with that, Eq. (1.1) was slightly modified by adding $3A - 6$ to it [?, ?]:

$$\nu = \nu_W + 3A - 6 = -2 + 2A - 2C + 2L + \sum_i \Delta_i. \tag{1.3}$$

That convention above is widely used and we will also stick to it as well.

In χEFT the first order, "leading order" ($\nu = 0$) is followed by the next-to-leading order ($\nu = 2$) [2], the next-to-next-to-leading order ($\nu = 3$) and so on. At each chiral order, new interaction diagrams complete the potential. There are only two diagrams at leading order (LO): one is a contact term and the other one is a one-pion exchange, see Fig. 1.1. Both diagrams reflect only 2NF. The same is for diagrams at next-to-leading order (NLO), where more contact terms occure together with two-pion exchange topologies. Each subsequent order includes more and more sophisticated diagrams describing nucleons interaction via multiple pion exchanges and various contact verteces. 3NF appears for the first time at next-to-next-to-leading order (N^{2}LO) while 4NF contributions start from next-to-next-to-next-to-leading order (N^{3}LO). This scheme establishes for the first time a systematic way to include all the contributions to a strong nuclear force starting from the simplest diagrams at LO and gradually adding more and more terms. It is also beneficial in the way that one can obtain results using chiral potential at different orders and track which one gives large or small contribution to the final prediction. At the moment, next-to-next-to-next-to-next-to-leading order (N^{4}LO) is the highest order at which 2N interaction has been completely derived. Nevertheless leading F-wave contact interactions from N^{5}LO have been combined with N^{4}LO force leading to the N^{4}LO$^+$ potential, which is currently regarded as a best available potential on the market. The progression of the chiral orders is reflected in a $\chi^2/data$. Leading order results in $\chi^2/data = 73$ (with neutron-proton data with $E_{lab} = 0 - 100$MeV). Each subsequent order has better and better results: NLO gives $\chi^2/data = 2.2$, N^{2}LO - $\chi^2/data = 2.2$ and the highest, N^{4}LO$^+$,

---

[1]Note that exact values of some parameters are still under discussion [?]. We follow here approach proposed by E.Epelbaum and collaborators, see e.g. [?]

[2]The contributions to the potential at order $\nu = 1$ completely vanish due to parity and time-reversal invariance, so the next-to-leading order stands for the second order ($\nu = 0$) of expansion.

leads to $\chi^2/data = 1.08$ [**?**]. Similar progress is observed for wider energy range, e.g for $E_{lab} = 0 - 300$MeV $\chi^2/data$ is 75, 14, 4.2, 2.01, 1.16 and 1.06 at LO, NLO, N^{2}LO, N^{3}LO, N^{4}LO and N^{4}LO$^+$, respectively. The proton-proton data description has similar trend, so $\chi^2/data$ is 1380, 91, 41, 3.43, 1.67, 1.00 for the same energy bin and chiral orders. At N^{4}LO$^+$ $\chi^2/data$ for proton-proton data stands similar value (close to 1) as for neutron-proton, but the convergence comes a bit later and leading order has way worse description. In my work I will use chiral potentials from LO up to N^{4}LO$^+$.

Figure 1.1: *Make own diagrams, e.g. with JaxoDraw or PyFeyn [?]*

The Argonne V18 potential [**?**], mentioned earlier, has 40 adjustable parameters, while χEFT NN potential at N^{4}LO [**?**] has only three *???* low-energy constants (LECs) fitted to deuteron properties. The reduction of the number of free parameters of the χEFT-based potentials has not only a theoretical but also a practical advantage in the studies of nuclear systems.

The general scheme outlined above was developed mainly by the Bochum-Bonn and Moscow-Idaho groups. Both groups have similar approaches and were independently and almost simultaneously developing their models. In 1998 Epelbaum and collaborators from the Bochum-Bonn group presented a first version of their NN chiral potential [**?**, **?**]. Developing a more and more sophisticated versions with higher chiral orders, authors presented N^{3}LO potential in 2005 [**?**] which included a 3NF contributions. They were further developing their chiral model, taking into account more Feynmann diagrams coming to a higher chiral orders. At some moment Bochum-Bonn goup faced with a problem of potential regularisation [**?**, **?**]. Solving it was an important step and autors where struggling with finding an appropriate regularization method to handle the divergences that arise in the χEFT calculations. Different techniques were applied such as the cutoff regularization and the regulator function methods. An important point was when authors

started using a semi-local regularisation in the coordinate space. The correspondant potential is called the SCS potential (semi-local regularisation in the coordinate space) [**?**]. Later similar regularisation, but done in momentum space was introduced, resulting in the most advanced chiral potential at the moment up to N^4LO^+ chiral order [**?**]: the semilocal momentum-space regularized potential (SMS). It is developed up to N^4LO^+ at the moment.

On the other side of the planet, in Idaho, Machleidt and his group from Moscow(Idaho) were also developing a chiral interaction. Their results from 2003 [**?**], following with later investigations [**?, ?, ?**] introduced very similar model to the one from the Bochum-Bonn group with minor technical differences.

There are a number of another attempts to construct the nuclear potential from the χEFT. M.Piarulli et al [**?, ?**] contributed to quite similar approach, based on the same chiral potentials but including explicitly Δ-isobar intermadiate states up to the third chiral order and taking into account sophisticated electromagnetic corrections.

Other groups try to improve already derived forces. Let us mention here works by A. Ekström and collaborators [**?, ?**] who, by using sophisticated fitting methods combined with statistical analysis, proposed so-called optimised interaction V_{opt} which was proved to provide a good description of atom properties for radii and calcium without using 3NF.

Another approach is the pionless effective field theory, which integrates out pions and focuses on the various types of contact interactions between nucleons [**?**]. Obtained potential has a very simple form, but cannot be applied to higher energies since pions start playing an important role there.

Yet another promising approach is the Lattice Effective Field Theory (LEFT), which is based on the Lattice QCD simulations of the strong interaction. Meißner and collaborators have developed a chiral effective theory for nuclear forces based on the results of lattice QCD calculations [**?**]. This approach has the advantage of being able to predict the nuclear force directly from the first principles, without the need for phenomenological input. However, currently it is limited to small systems and low energies due to the computational resources required for calculations. Up to now, the relatively simple two-nucleon scattering problem and few-nucleon bound state have been solved within the LEFT and more complex systems are still under attack. For more details please refer to [**?**].

Technically, the chiral potential may be derived both in coordinate and momentum spaces. Nevertheless in both cases it requires regularisation which improves potential behavior at small distances or at high momenta, which allows to avoid infinities. The SMS potential is being regularized semilocally. It means that local or nonlocal regularisations are being applied for different parts of the potential. In [**?, ?**] the non-local regulation scheme was applied to both short- and long-range parts of the potential while in the next model [**?, ?**] it affected only a short range part. This regularisation is applied directly to the potential matrix elements in the coordinate space:

$$V_\pi(\vec{r}) \to V_{\pi,R}(\vec{r}) = V_\pi(\vec{r}) \left(1 - \exp\left(-r^2/R^2\right)\right), \tag{1.4}$$

or in the momentum space

$$V_\pi(\vec{p}', \vec{p}) \to V_\Lambda(\vec{p}', \vec{p}) = V_\pi(\vec{p}', \vec{p}) \exp\left[-(p'/\Lambda)^{2n} - (p/\Lambda)^{2n}\right], \tag{1.5}$$

where the cutoff R was chosen in the range of R = 0.8, ..., 1.2 fm, $\Lambda = \frac{2}{R}$ and n being adjusted with respect to the considered chiral order. For specific case of the SMS force

$\Lambda = 400 - 550 \, \text{MeV}$ and $n = 3$.

The other way of regularisation, the local one, is applied to the propagator operator, already during the derivation of potential. Namely, the Gaussian form factor $F(\vec{l}^2)$ is being used to reduce pions with higher momenta:

$$\int_{-\infty}^{\infty} \frac{\rho(\mu^2)}{\vec{l}^2 + \mu^2} d\mu^2 \to \frac{F(\vec{l}^2)}{\vec{l}^2 + \mu^2} \tag{1.6}$$

with

$$F(\vec{l}^2) = e^{-\frac{\vec{l}^2 + M_\pi^2}{\Lambda^2}}, \tag{1.7}$$

M_π is an effective pion mass, Λ - a cutoff parameter and l is a four-momentum of the exchanged pion. *Further μ is a ...* The form factor (1.7), being used together with Feynman propagator, ensures that long-range part of the forces has no singularities.

The cut-off parameter Λ is not fixed and usually calculations are being performed for its different values. The comparison of such results may reveal stronger or weaker dependance and in a perfect case, which is expected at $\nu >> 1$, one will come up with such a potential, were the cut will not affect results at all. One of aims of my thesis is to test how big cut-off dependency of predictions is observed for the best currently available forces (SCS and SMS). To illustrate a cutoff dependency of the potential, in Fig. 1.2 I show values of the matrix elements for 2N $\langle p|V|p'\rangle$ potential $^3S_1 - ^3D_1$ as a function on the momentum $|\vec{p}|$ with fixed value $|\vec{p}'|=0.054 \, \text{fm}^{-1}$. Please note, that relatively strong dependency of specific matrix element of the potential is not always leading to a strong dependency of observables, as observables comprise contributions from many matrix elements.

Yet another regularisation function is used by R. Machleidt, D.R. Entem and A. Nogga, when regulating matrix elements of the potential in momentum space with non-local regulator only. That is a main reason of the observed differences between predictions based on Epelbaum's and Machleidt's models.

Currents

The electromagnetic current operator for a few-nucleon system has both one- and many-body contributions, which can be denoted as j_μ^1, j_μ^2, j_μ^3, etc, respectively (where $\mu = 0..3$ denotes a four-vector components). The leading one-body contribution, j_μ^1, represents the photon's interaction with a single nucleon. The many-body contributions are known as meson exchange currents (MEC), and arise from the meson-exchange picture of the nucleon-nucleon (NN) interaction. In that picture the photon can couple to mesons exchanged between two nucleons, leading to two-body contributions to the nuclear current. The necessity of introducing the MEC arises from the continuity equation, which requires the inclusion of two-body interactions in the Hamiltonian. The momentum and isospin-dependent terms in the potential require, in turn, the introduction of two-body MEC. Similarly, the inclusion of the three-body force into the Hamiltonian requires the existence of three-body contributions to the nuclear current. However, the effects of the three-body MEC are likely negligible in the low-energy region. Therefore, in the thesis I will consider one- and two-body currents, only. The continuity equation, connecting the interaction <nd the current clearly shows that those both quantities should be derived consistently from the same underlying theory of nuclear phenomenas. I work with the

$$p' = 1.798 \; [\text{fm}^{-1}]$$

Figure 1.2: Matrix elements $\langle p|V|p'\rangle$ of the potential in coupled partial waves $^3S_1 - ^3D_1$ as a function on the momentum p with fixed value of the momentum $p' = 1.798\,\text{fm}^{-1}$. Potential element $V_{ll'}$ is taken between two states with angular momenta l and l' where $l = 0$ stands for $^3S_1$ state and $l = 2$ - for $^3D_1$.

SMS chiral interaction, and for that force the complete consistant MEC has not been derived yet. Consistency includes here also the same regularization as used for the interation. While the derivation of such is ongoing (H. Krebs, private communication), at the moment only SNC is well established. Thus to mimic effects of the MEC, I apply the Siegert theorem [?, ?]. In general, this theorem allows to substitute explicit MEC terms by the *O-th* component of the nuclear current (the charge density). It is less sensitive to MEC contributions (compared to spatioal components of j_μ) and thus in its case the SNC approximation is sufficient. I use here the formulation of the Siegert theorem given in [?].

A more detailed discussion of electromagnetic currents used here is given in the Section 2.6.

CHAPTER 2

FORMALISM & NUMERICAL METHODS

Despite the fact that the deuteron problem was solved long time ago, I will describe it briefly in order to introduce the notation and formalism. With that, for more complex 3N case only slight extension will be needed.

In order to calculate any observable for the deuteron photodisintegration, one has to find a nuclear matrix elements:

$$N^\mu = \langle \Psi_{final} \mid J^\mu \mid \Psi_{initial} \rangle, \tag{2.1}$$

with two-nucleon wave function of the initial state Ψ $,ie.includingtwo - andthree - nucleoninteraction, initial = \Psi_{deuteron}$; two-nucleon wave function of the final scattering state Ψ_{final} and a four-vector current operator J^μ which acts between initial and final two-nucleon states. In following I describe how to get that quantities.

2.1 Deuteron bound state

Let's find a deuteron bound state wave function $|\phi_d\rangle$. The time-independent Schrödinger equation for two particles expresses as:

$$(H_0 + V) |\phi_d\rangle = E_d |\phi_d\rangle , \tag{2.2}$$

with a kinetic energy H_0 and potential V. The kinetic energy H_0 can be represented in terms of relative and total momenta of the particles:

$$H_0 = \frac{\vec{p_1}^2}{2m_1} + \frac{\vec{p_2}^2}{2m_2} = \frac{\vec{p}^2}{2\mu} + \frac{\vec{\mathcal{P}}^2}{2M}, \tag{2.3}$$

where the relative and total momenta are defined as follows:

$$\vec{p} = \frac{(m_1\vec{p_1} - m_2\vec{p_2})}{m_1 + m_2}, \tag{2.4}$$

$$\vec{\mathcal{P}} = \vec{p_1} + \vec{p_2}, \tag{2.5}$$

where $M = m_1 + m_2$ is a total mass, $\mu = \frac{m_1 m_2}{M}$ is a reduced mass of two nucleons and $\vec{p_i}$ is a momentum of i-th particle.

Potential V is assumed to depend on the relative degrees of freedom only, so Eq. (2.2) may be decomposed into two separated equations:

$$\frac{\vec{p}^2}{2\mu}\langle \vec{p} \mid \Psi_{int}\rangle + \langle \vec{p} \mid V \mid \Psi_{int}\rangle = (E_d - E)\langle \vec{p} \mid \Psi_{int}\rangle \tag{2.6}$$

$$\frac{\vec{\mathcal{P}}^2}{2M}\langle \mathcal{P} \mid \Psi\rangle = E\langle \mathcal{P} \mid \Psi\rangle, \tag{2.7}$$

with $\left\langle \vec{p}, \vec{\mathcal{P}} \middle| H_0 \middle| \phi_d \right\rangle = \frac{\vec{p}^2}{2\mu}\langle \vec{p}|\Psi_{int}\rangle + \frac{\vec{\mathcal{P}}^2}{2M}\langle \mathcal{P}|\Psi\rangle$. So Ψ is a component of total wave function, which reflects a deuteron as a single object with momentum $\vec{\mathcal{P}}$ while Ψ_{int} is an internal wave function describing interaction between nucleons. Basis state $|\vec{p}\rangle$ obeys a completeness equation:

$$\int d^3\vec{p}\,|\vec{p}\rangle\,\langle \vec{p}| = \mathbb{1}. \tag{2.8}$$

Eq. (2.6) is basically the Schrödinger equation for a single particle with mass μ in potential V and Eq. (2.7) can be regarded as a Schrödinger equation for particle with mass M in a free motion. Assuming that deuteron is at rest ($E = 0$) we can stick to the Eq.(2.6) only. Using completeness relation (2.8) we get:

$$\frac{\vec{p}^2}{2\mu}\langle \vec{p} \mid \Psi_{int}\rangle + \int d\vec{p}'\langle \vec{p} \mid V \mid \vec{p}'\rangle\langle \vec{p}' \mid \Psi_{int}\rangle = E_d\langle \vec{p} \mid \Psi_{int}\rangle \tag{2.9}$$

Working in 3 dimensional space is difficult, especially numerically, so I follow a standard path and introduce the partial-wave decomposed representation (PWD) of the momentum state, adding spin and isospin degrees of freedom in the following form:

$$|p\alpha\rangle \equiv |p(ls)jm_j\rangle\,|tm_t\rangle, \tag{2.10}$$

where quantum numbers l, s, j, t are orbital angular momentum, total spin, total angular momentum and total isospin respectively. m_j and m_t are total angular momentum and isospin projections, respectively.

States $|p(ls)jm_j\rangle$ can be further decomposed to the more basic states than it is in (2.10), separating spin part as

$$|p(ls)jm_j\rangle = \sum_{m_l} c(lsj; m_l, m_j - m_l, m_j)\,|plm_l\rangle\,|s\ m_j - m_l\rangle. \tag{2.11}$$

Spin(isospin) states can be further represented via single-nucleon spin(isospin) states:

$$|sm_s\rangle = \sum_{m_1} c(\tfrac{1}{2}\tfrac{1}{2}s; m_1, m_s - m_1, m_s)\left|\tfrac{1}{2}m_1\right\rangle\left|\tfrac{1}{2}m_s - m_1\right\rangle, \tag{2.12}$$

$$|tm_t\rangle = \sum_{\nu_1} c(\tfrac{1}{2}\tfrac{1}{2}t; \nu_1, m_t - \nu_1, m_t)\left|\tfrac{1}{2}\nu_1\right\rangle\left|\tfrac{1}{2}m_t - \nu_1\right\rangle. \tag{2.13}$$

In Eqs.(2.11)-(2.13), $c(...)$ are Clebsh-Gordon coefficients. Nucleons are spin $\frac{1}{2}$ particles, and we also treat proton and neutron as the same particle in different isospin states, using convention in which isospin $\nu_1 = \frac{1}{2}$ stands for proton and $\nu_1 = -\frac{1}{2}$ is for neutron.

The states $|\,plm_l\rangle$ from Eq.(2.11) are orthogonal

$$\langle p'l'm'_l \mid plm_l \rangle = \frac{\delta(p-p')}{p^2}\delta_{ll'}\delta_{m_l m'_l} \tag{2.14}$$

and satisfy the completeness relation:

$$\sum_{l=0}^{\infty}\sum_{m_l=-l}^{l}\int dp p^2 \mid plm_l \rangle\langle plm_l \mid = \mathbb{1} \tag{2.15}$$

Projection of $\langle \vec{p}' \mid$ states to $\mid plm_l \rangle$ leads to

$$\langle \vec{p}' \mid plm_l \rangle = \frac{\delta(\mid\vec{p}'\mid - p)}{p^2}Y_{lm_l}(\hat{p}'), \tag{2.16}$$

where $Y_{lm_l}(\hat{p}')$ is a spherical harmonic and 'hat' denotes a unit vector $\hat{X}$ in direction of $\vec{X}$. Thus for the momentum vector:

$$\vec{p} \equiv \mid\vec{p}\mid\hat{p} \equiv p\hat{p}. \tag{2.17}$$

Nucleons are fermions so exchanging them leads to antisymmetry of the wave function. In PWD it results in additional requirement on allowed quantum numbers which is:

$$(-1)^{l+s+t} = -1. \tag{2.18}$$

In general, nuclear NN force conserves spin, parity and charge so

$$\langle p'\alpha' \mid V \mid p\alpha \rangle = \delta_{jj'}\delta_{mm'}\delta_{tt'}\delta_{m_t m_{t'}}\delta_{ss'}V_{l'l}^{sjtm_t}(p',p) \tag{2.19}$$

which introduces restrictions for particular sets of quantum numbers and α. Strong interaction allows for change of the orbital angular momenta $l = j \pm 1$, $l' = j' \pm 1$. The channels, in which $l \neq l'$ is allowed, are calld a coupled channels and for the deuteron bound state one can find only one such PWD state combination: two coupled channels which are commonly denoted as $^3S_1$ and $^3D_1$ (the naming stands for $^{2s+1}l_j$). They correspond to $l = 0$ and $l = 2$ respectively (with $s = j = 1$ and $t = m_t = 0$). We will call wave functions for these channels as $\phi_l(p)$ with $l = 0, 2$, such that:

$$\phi_l(p) = \langle p(ls)jm_j \mid \langle tm_t \mid\Psi_{int}\rangle = \langle p(l1)1m_d \mid \langle 00 \mid\Psi_{int}\rangle ; l = 0, 2. \tag{2.20}$$

In that new basis Eq.(2.9) takes a form of two coupled equations:

$$\frac{\vec{p}^2}{2\mu}\phi_l(p) + \sum_{l'=0,2}\int dp'p'^2 \langle p(l1)1m_d \mid \langle 00 \mid V\mid 00\rangle \mid p'(l'1)1m_d\rangle \phi_{l'}(p') = E_d\phi_l(p), \tag{2.21}$$

for $l = 0, 2$. In case one does not have a matrix elements for the potential $\langle plm_l \mid V \mid p'l'm'_l\rangle$ in analytical form, but only numerical values for some grid of points are given, there is still one complication in the Eq.(2.21) - integration, which has to be discretized. In order to get rid of the integral I use a Gaussian quadrature method of numerical integration [?]. It allows me to replace an integral by the weighted sum: $\int_a^b f(x)dx = \sum_{i=1}^{n}\omega_i f(x_i)$ In current work I used $N = 72$ points in the interval from 0 to $50\,\mathrm{fm}^{-1}$. Using this method, Eq.(2.21) becomes

$$\frac{p_i^2}{2\mu}\phi_l(p_i) + \sum_{l'=0,2}\sum_{j=0}^{N_P}\omega_j p_j^2 \langle p_i(l1)1m_d| \langle 00|V|00\rangle |p_j(l'1)1m_d\rangle \phi_{l'}(p_j) = E_d\phi_l(p_i). \quad (2.22)$$

In practical computations, the same grid points p_i and p_j are used in order optimize computational time. I solve this equation as an eigenvalue problem $M\Psi = E_d\Psi$ and in that way find simultaneously wave function values in grid of p points and The binding energy E_d. The binding energy E_d calculated with potentials at different chiral orders is presented in Fig. 2.1.
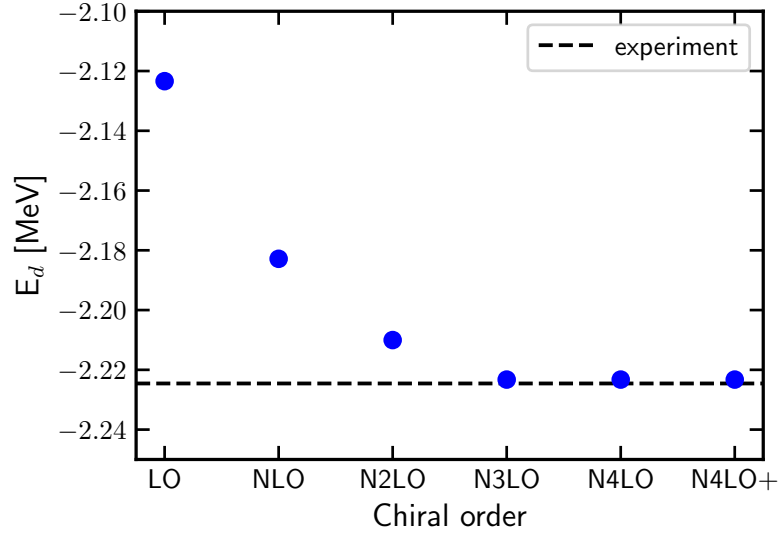
Figure 2.1: Deuteron binding energy calculated using the chiral SMS potential at different chiral orders as a mean value over all cutoffs. Experimental data is taken from [?].

An example of such wave functions is demonstrated in Fig. 2.2. The left panel demonstrate a wave function for $l = 0$ - $^3S_1$ while the right one - for $l = 2$ - $^3D_1$. Both plots consist of the curves for different cutoff values and using the chiral SMS potential at N^4LO^+. The small deviation between lines show that cutoff dependence is rather weak at this stage and further discrepancies connected to the value of Λ may appear in other components of nuclear matrix elements.

2.2 2N scattering state

I work in the time-independent formulation of the scattering process. In such a case the Hamiltonian is:

$$H = H_0 + V, \quad (2.23)$$

where again H_0 is a kinetic energy operator, $H_0 = \frac{\vec{p}^2}{2m}$, and V is a nucleon-nucleon interaction. For a free particle motion, V will be absent and we will denote a corresponding energy eigenstate as a free particle state $|\vec{p}\rangle$. The scattering state $|\psi\rangle$ fulfills similar Schrödinger equation as $|\vec{p}\rangle$, with the same energy eigenvalue, but with the presence of the potential:

Figure 2.2: The deuteron wave function ϕ_l for l=0 ($^3S_1$ partial wave)(left) and l=2 ($^3D_1$) (right). Each curve shows results obtained with different values of the cutoff parameter Λ. The chiral SMS potential at N^{4}LO$^+$ was used.

$$
\begin{cases}
H_0 \, |\vec{p}\rangle & = E \, |\vec{p}\rangle \, , \\
(H_0 + V) \, |\psi\rangle & = E \, |\psi\rangle \, .
\end{cases}
\tag{2.24}
$$

We are interested in solution for Eq. (2.24), so that $|\psi\rangle \to |\vec{p}\rangle$ as $V \to 0$ and both $|\psi\rangle$ and $|\vec{p}\rangle$ have the same energy eigenvalues E. As we have scattering process, the energy spectra for both operators H_0 and $H_0 + V$ are continuous.

From Eq. (2.24) it follows that

$$
|\psi\rangle = \frac{1}{E - H_0} V \, |\psi\rangle + |\vec{p}\rangle \, ,
\tag{2.25}
$$

which guarantees that application of the operator $(E - H_0)$ to the Eq. (2.25) results in the second equation from the set (2.24).

In order to deal with a singular operator $\frac{1}{E-H_0}$ in Eq. (2.25), the well-known technique is used to make such an operator complex by adding small imaginary number to the denominator so Eq. (2.25) becomes

$$
|\psi\rangle = G_0(E \pm i\epsilon) V \mid \psi\rangle + \mid \vec{p}\rangle,
\tag{2.26}
$$

where G_0 is a free propagator:

$$
G_0(z) = \frac{1}{z - H_0}.
\tag{2.27}
$$

Solution with $G_0(E - i\epsilon)$ corresponds to the incoming spherical wave, while $G_0(E + i\epsilon)$ - to the outgoing one. Since we are interested in the final scattering state, only the (+) sign survives.

Eq. (2.26) is known as the Lippmann-Schwinger equation (LSE). Defining the transition operator t:

$$
t \, |\vec{p}\rangle = V \, |\psi\rangle
\tag{2.28}
$$

we can rewrite it as

$$|\psi\rangle = (1 + G_0(E + i\epsilon)t)|\vec{p}\rangle. \tag{2.29}$$

With substitution of Eq. (2.26) into Eq. (2.28) we can find an explicit form of the t operator:

$$t|\vec{p}\rangle = VG_0(E + i\epsilon)V \mid \psi\rangle + V \mid \vec{p}\rangle =$$
$$= VG_0(E + i\epsilon)t|\vec{p}\rangle + V \mid \vec{p}\rangle \tag{2.30}$$

Getting rid off the initial state $|\vec{p}\rangle$ in the Eq. (2.30) we can get the LSE for the transition operator in the iterative form:

$$t = V + VG_0t =$$
$$= V + VG_0V + VG_0VG_0V + ..., \tag{2.31}$$

which constitutes an infinite series of subsequent NN interactions and free propagators of nucleons.

In the partial-wave representation, the LSE Eq. (2.30) expresses as:

$$\langle p'(l's')j'm_{j'}| \langle t'm_{t'}|t(E)|tm_t\rangle |p(ls)jm_j\rangle = \langle p'(l's')j'm_{j'}| \langle t'm_{t'}|V|tm_t\rangle |p(ls)jm_j\rangle +$$
$$+ \sum_{\alpha''} \int_0^\infty dp''p''^2 \langle p'(l's')j'm_{j'}| \langle t'm_{t'}|V|t''m_{t''}\rangle |p''(l''s'')j''m_{j''}\rangle$$
$$\times \frac{1}{E + i\epsilon - p''^2/m} \langle p''(l''s'')j''m_{j''}| \langle t''m_{t''}|t(E)|tm_t\rangle |p(ls)jm_j\rangle, \quad (2.32)$$

which after using symmetries of potential matrix elements (2.19) reduces to

$$\langle p'(l's')jt|t(E)|p(ls)jt\rangle = \langle p'(l's)jt|V|p(ls)jt\rangle +$$
$$+ \sum_{l''} \int_0^\infty dp''p''^2 \langle p'(l's)jt|V|p''(l''s)jt\rangle$$
$$\times \frac{1}{E + i\epsilon - p''^2/m} \langle p''(l''s)jt|t(E)|p(ls)jt\rangle. \quad (2.33)$$

I solve Eq. (2.33) numerically, which again requires discretisation and therefor leads to set of linear equations. Finally, using Eq. (2.29) and denoting the momentum state of two nucleons with spin projections m_p and m_n as $\langle \phi m_p m_n|$, we can write Eq. (2.1) as

$$N^\mu = \langle \phi m_p m_n| (1 + G_0(E + i\epsilon)t)J^\mu(0) \mid \Psi_{deuteron}\rangle \tag{2.34}$$

2.3   3N bound state

The 3N bound state is described by the Schrödinger equation for 3N system, ie. including two- and three- nucleon interaction, and its total wave function obeys the following equation:

$$|\Psi\rangle = G_0(E + i\epsilon) \sum_{j=1}^{3} (V_j + V_4^j) |\Psi\rangle, \qquad (2.35)$$

where G_0 is a 3N free propagator as in Eq. (2.27), V_j - is a two-body potential acting between nucleons k and l (j, k and l - numerate nucleons, $j, k, l \in 1, 2, 3$ and $j \neq k \neq l$), V_4^j is a component of three-body potential $V_4 = \sum_{j=1}^{3} V_4^j$ symmetrical under exchange of nucleons k and l, and E - is a 3N binding energy.

Eq. (2.35) can be split into three independent equations for so-called Faddeev components $|\psi_j\rangle$

$$|\Psi\rangle = \sum_{j=1}^{3} |\psi_j\rangle, \qquad (2.36)$$

which fulfills separately

$$|\psi_j\rangle = G_0(E + i\epsilon)(V_j + V_4^j) |\Psi\rangle. \qquad (2.37)$$

Next, I introduce a permutation operator P, which is a combination of operators P_{jk}:

$$P = P_{12}P_{23} + P_{13}P_{32}. \qquad (2.38)$$

The operator component P_{jk} acting on the state interchange the momenta and quantum numbers of the nucleons j and k.

Using definitions 2.38 and 2.36, one can rewrite Eq. (2.37) as:

$$|\psi_j\rangle = G_0(E + i\epsilon)t_j P |\psi_j\rangle + (1 + G_0(E + i\epsilon)t_j)G_0(E + i\epsilon)V_4^j(1 + P) |\psi_j\rangle, \qquad (2.39)$$

where t_j is a two-body t-operator which obeys Eq. (2.30) for corresponding two-body potential V_j. I solve Eq. (2.39) numerically to find $|\psi_j\rangle$ and the binding energy E. To do that, I perform PWD again.

The partial wave representation of the Eq. (2.39) is obtained using following 3N states:

$$|p, q, \alpha_{J,M_J}\rangle = \left| p, q, (ls)j, (\lambda, \frac{1}{2})I(jI)JM; (t\frac{1}{2})TM_T \right\rangle_1, \qquad (2.40)$$

where index 1 states the choice of the Jacobi momenta, such that p is a relative momentum of the nucleons 2 and 3. Values l, s and j are quantum numbers in the two-body subsystem consisted of nucleons 2 and 3. λ is the orbital angular momentum with respect to the c.m. of the particles 2 and 3, of the first particle which spin is $\frac{1}{2}$ and I is its total angular momentum. J and M_J are the total angular momentum of the 3N system and its projection on the z-axis respectively. t is a total isospin of the 2-3 subsystem whereas T and M_T are the total isospin of the 3N system and its projection on the z-axis, respectively.

2.4   3N scattering state

Let us introduce an asymptotic state $\left|\Phi_j^{3N}\right\rangle$ describing a free motion of three nucleons j, k, l with particles k and l having relative momentum $\vec{p}$ and particle j moving with

momentum $\vec{q}$ relatively to the center of mass $(k - l)$:

$$\left|\Phi_j^{3N}\right\rangle \equiv \frac{1}{\sqrt{2}}(1 - P_{kl})\left|\vec{p}(kl)\vec{q}(j)\right\rangle. \tag{2.41}$$

The Jacobi momenta $\vec{p}$ and $\vec{q}$ build the total energy of three nucleons in the 3N-c.m. system:

$$E_{3N} = \frac{|\vec{p}|^2}{m} + \frac{3|\vec{q}|^2}{4m}. \tag{2.42}$$

Using a free propagator $G(E_{3N} - i\epsilon)$ we can come up with the total 3N scattering state

$$\left|\Psi^{(-)}\right\rangle^{3N} = \frac{1}{\sqrt{3}}\sum_j\left|\Psi_j^{(-)}\right\rangle^{3N}, \tag{2.43}$$

where auxiliary scattering states $\left|\Psi_j^{(-)}\right\rangle^{3N}$ are defined as [?]

$$\left|\Psi_j^{(-)}\right\rangle^{3N} \equiv \lim_{\epsilon\to 0} i\epsilon G(E_{3N} - i\epsilon)\left|\Phi_j^{3N}\right\rangle. \tag{2.44}$$

The state $\left|\Psi_j^{(-)}\right\rangle^{3N}$ together with the state $\left|\Phi_j^{3N}\right\rangle$ fulfills an equation [?]

$$\left|\Psi_j^{(-)}\right\rangle^{3N} = \left|\Phi_j^{3N}\right\rangle + G_0\left(V_1 + V_2 + V_3 + V_4\right)\left|\Psi_j^{(-)}\right\rangle^{3N}. \tag{2.45}$$

Defining the antysymmetrized Faddeev components, and using index "i" instead of "j"

$$\left|F_i^0\right\rangle \equiv G_0\left(V_i + V_4^i\right)(1 + P)\left|\Psi_i^{(-)}\right\rangle^{3N} \tag{2.46}$$

we obtain a 3N scattering wave function as:

$$\begin{aligned}
\left|\Psi^{(-)}\right\rangle^{3N} &= \frac{1}{\sqrt{3}}\left(\sum_{i=1}^3\left|\Phi_i^{3N}\right\rangle + G_0\left(V_1 + V_2 + V_3 + V_4\right)\sum_{i=1}^3\left|\Psi_i^{(-)}\right\rangle^{3N}\right) \\
&= \frac{1}{\sqrt{3}}\left(\sum_{i=1}^3\left|\Phi_i^{3N}\right\rangle + \sum_{i=1}^3\left|F_i^0\right\rangle\right) = \frac{1}{\sqrt{3}}(1 + P)\left(\left|\Phi_1^{3N}\right\rangle + \left|F_1^0\right\rangle\right).
\end{aligned} \tag{2.47}$$

In this case the nuclear matrix element $N_\mu^{3N} = \langle\Psi^-|j^\mu|\psi_i\rangle$ (with $|\psi_i\rangle$ being the Faddeev component of the 3N bound state (2.36)) is [?,?] *???* :

$$\begin{aligned}
N_\mu^{3N} = \frac{1}{\sqrt{3}}\left\langle\Phi_1^{3N}\left|(1 + P)j_\mu\right|\Psi_i\right\rangle + \frac{1}{\sqrt{3}}\left\langle\Phi_1^{3N}\left|t_1^+G_0^+(1 + P)j_\mu\right|\Psi_i\right\rangle \\
+ \frac{1}{\sqrt{3}}\left\langle\Phi_1^{3N}\left|t_1^+G_0^+P\right|U_\mu\right\rangle + \frac{1}{\sqrt{3}}\left\langle\Phi_1^{3N}|P|U_\mu\right\rangle,
\end{aligned} \tag{2.48}$$

where U_μ fulfills the following equation:

$$|U_\mu\rangle = \left[t_1^+ G_0^+ + \frac{1}{2}(1+P)V_4^{(1)} G_0^+ \left(1 + t_1^+ G_0^+ \right) \right] (1+P)j_\mu \, |\Psi_i\rangle$$
$$+ \left[t_1^+ G_0^+ P + \frac{1}{2}(1+P)V_4^{(1)} G_0^+ \left(1 + t_1^+ G_0^+ \right) P \right] |U_\mu\rangle \,. \tag{2.49}$$

Eq. (2.49) is being solved numerically in PWD. The techniques applied closely resemble those presented in [?] for N-d elastic scattering.

2.5 Nd scattering state

Analogously to the bound state, one can express a nucleon-deuteron scattering state using a permutation operator Eq. (2.38).

$$\left| \Psi^{(-)} \right\rangle^{Nd} = \frac{1}{\sqrt{3}} \sum_j \left| \Psi_j^{(-)} \right\rangle^{Nd} \tag{2.50}$$

Further a scattering state $\left| \Psi_j^{(-)} \right\rangle^{Nd}$ can be expressed in terms of asymptotic state $\left| \Phi_j^{Nd} \right\rangle$, in which particles k and l form a deuteron and the third particle (nucleon j) propagates freely with a relative momentum $\vec{q}_0$ with respect to the deuteron:

$$\left| \Psi_j^{(-)} \right\rangle^{Nd} \equiv \lim_{\epsilon \to 0} i\epsilon G(E_{Nd} - i\epsilon) \left| \Phi_j^{Nd} \right\rangle \tag{2.51}$$
$$\left| \Phi_j^{Nd} \right\rangle \equiv \left| \Phi_{d(k,l)} \right\rangle |\vec{q}_0\rangle \,, \tag{2.52}$$

where $\left| \Phi_{d(k,l)} \right\rangle$ is a deuteron wave function and $|\vec{q}_0\rangle$ - a free particle state and $G(t)$ is a free propafator of N-d pair. E_{Nd} is a total energy of the N-d system:

$$E_{Nd} = E_d + \frac{3|\vec{q}_0|^2}{4m}, \tag{2.53}$$

where E_d is the deuteron binding energy and m denotes the nucleon mass.

$\left| \Psi^{(-)} \right\rangle^{Nd}$ can be expressed by the Faddeev components

$$\left| \Psi^{(-)} \right\rangle^{Nd} = \frac{1}{\sqrt{3}}(1+P) \left| F_1 \right\rangle \,, \tag{2.54}$$

where

$$|F_1\rangle = \left| \phi_1^{Nd} \right\rangle G_0(\nu_1 + \nu_2 + \nu_3 + \nu_4) \sum_{j=1}^3 \left| \Psi_j^{(-)} \right\rangle^{Nd} \,. \tag{2.55}$$

The nuclear matrix element $N_\mu^{Nd} =^{Nd} \langle \Psi^- | j_\mu | \Psi_i \rangle$ (with Ψ_i - bound state) is now [?,?] ??? :

$$N_\mu^{Nd} = \frac{1}{\sqrt{3}} \left\langle \Phi_1^{Nd} \right| (1+P)j_\mu \left| \Psi_i \right\rangle + \frac{1}{\sqrt{3}} \left\langle \Phi_1^{Nd} \right| P \left| U_\mu \right\rangle \tag{2.56}$$

with U_μ being a solution to

$$\begin{aligned}
|U_\mu\rangle &= \left[t_1^+ G_0^+ + \frac{1}{2}(1+P)V_4^{(1)} G_0^+ \left(1 + t_1^+ G_0^+\right)\right] (1+P) j_\mu |\Psi_i\rangle + \\
&+ \left[t_1^+ G_0^+ P + \frac{1}{2}(1+P)V_4^{(1)} G_0^+ \left(1 + t_1^+ G_0^+\right) P\right] |U_\mu\rangle
\end{aligned} \tag{2.57}$$

Eq. (2.57) is being solved numerically in a same way as Eq. (2.49), namely applying PWD as it is described in [?].

2.6 Nuclear electromagnetic current

The electromagnetic current operator for 2N (3N) system is constructed from the one- and many-body currents:

$$j_\mu = j_\mu^1 + j_\mu^2 (+ j_\mu^3). \tag{2.58}$$

In Eq. (2.58) j_μ^n is a contribution from the interaction between photon and n nucleons (j_μ^3 is presented in 3N system only) and (j_μ^1) is a sum of interactions with each nucleon in the system.

Regarding the photodisintegration process, only a single nucleon current (1NC) is used, so I stick to its definition here.. In the Hamiltonian framework, the nucleons are constrained to lie on the mass shell. The general current expression for a single nucleon at the spacetime point zero, denoted as $j_\mu^1(0)$, is computed between the initial nucleon momentum $p \equiv \left(p_0 = \sqrt{M_N^2 + \vec{p}^2}, \vec{p}\right)$ and the final momentum $p' \equiv \left(p_0' = \sqrt{M_N^2 + \vec{p}'^2}, \vec{p}'\right)$. This computation yields the following expression:

$$\begin{aligned}
\langle \vec{p}' | j_\mu^1(0) | \vec{p} \rangle &= \bar{u}\left(\vec{p}'s'\right)\left(\gamma^\mu F_1 + i\sigma^{\mu\nu}\left(p'-p\right)_\nu F_2\right) u(\vec{p}s) \\
&= \bar{u}\left(\vec{p}'s'\right)\left(G_M \gamma^\mu - F_2\left(p'+p\right)^\mu\right) u(\vec{p}s).
\end{aligned} \tag{2.59}$$

In the above equation, ie. including two- and three- nucleon interaction, the symbols $u(\vec{p}s)$ represent Dirac spinors for particle having momentum $\vec{p}$ and spin s, F_1 and F_2 are the Dirac and Pauli form factors of the nucleon, respectively, and $G_M \equiv F_1 + 2M_N F_2$ denotes the magnetic form factor of the nucleon. The proton charge e is extracted from the matrix element. In this thesis, only the nonrelativistic limit of Eq. (2.59) is considered, which leads to well-known expressions for the operators for the current:

$$\langle \vec{p}' | j_0^1 | \vec{p} \rangle = \left(G_E^p \Pi^p + G_E^n \Pi^n\right), \tag{2.60}$$

$$\langle \vec{p} | \vec{j}^1 | \vec{p} \rangle = \frac{\vec{p} + \vec{p}'}{2M_N}\left(G_E^p \Pi^p + G_E^n \Pi^n\right) + \frac{i}{2M_N}\left(G_M^p \Pi^p + G_M^n \Pi^n\right)\vec{\sigma} \times \left(\vec{p}' - \vec{p}\right). \tag{2.61}$$

The electric form factor, denoted as G_E, is defined as, $G_E \equiv F_1 + \frac{(p'-p)^2}{2M_N}F_2$ and represents the neutron (n) and proton (p) form factors. Both electric and magnetic form factors, G_E and G_M, are normalized as:

$$G_E^n(0) = 0$$
$$G_E^p(0) = 1$$
$$G_M^n(0) = -1.913$$
$$G_M^p(0) = 2.793$$

(2.62)

The above values correspond to nucleons with point-like characteristics. While all the form factors depend on the squared four-momentum transfer $(p' - p)^2$, in the nonrelativistic regime, it is common to use the squared three-momentum transfer $-(\vec{p}' - \vec{p})^2$ or even set it to zero for interactions involving real photons. Numerous authors have investigated the properties of electromagnetic nucleon form factors through theoretical and experimental approaches, as discussed in [?, ?]. Π^p (Π^n) in Eq. (2.61) is a proton (neuteron) isospin projection operator.

The two-nucleon current contribution is in that work taken into account via Siegert approach [?, ?, ?]. In order to do that we break down the single nucleon current matrix elements into multipole components and represent some of the electric multipoles using the Coulomb multipoles, which arise from the single nucleon charge density operator [?]. This is acceptable because, in low-energy situations, contributions from many nucleons to the nuclear charge density are typically insignificant. We then obtain the rest of the electric multipoles and all of the magnetic multipoles exclusively from the single nucleon current operators.

In 3N system we have following componnents of the 1NC:

$$\langle \vec{p}', \vec{q}' | j_0^1 | \vec{p}, \vec{q} \rangle = \int d\vec{p}'' d\vec{q}'' \left\langle \vec{p}', \vec{q}' \left| \frac{1}{2} (1 + \tau(1)_z) F_1^p + \frac{1}{2} (1 - \tau(1)_z) F_1^n \right| \vec{p}'', \vec{q}'' \right\rangle$$
$$\left\langle \vec{p}'', \vec{q}'' - \frac{2}{3}\vec{Q} \middle| \vec{p}, \vec{q} \right\rangle$$

(2.63)

$$\langle \vec{p}', \vec{q}' | j_{\pm}^{1, \text{ conv}} | \vec{p}, \vec{q} \rangle = \frac{1}{m} \int d\vec{p}'' d\vec{q}'' \langle \vec{p}', \vec{q}' | \left[\frac{1}{2} (1 + \tau(1)_z) F_1^p + \frac{1}{2} (1 - \tau(1)_z) F_1^n \right] q_{\pm}$$
$$|\vec{p}'', \vec{q}'' \rangle \left\langle \vec{p}'', \vec{q}'' - \frac{2}{3}\vec{Q} \middle| \vec{p}, \vec{q} \right\rangle$$

(2.64)

$$\langle \vec{p}', \vec{q}' | j_{\pm}^{1, spin} | \vec{p}, \vec{q} \rangle = \frac{i}{2m} \int d\vec{p}'' d\vec{q}'' \langle \vec{p}', \vec{q}' |$$
$$* \left[\frac{1}{2} (1 + \tau(1)_z) (F_1^p + 2m F_2^p) + \frac{1}{2} (1 - \tau(1)_z) (F_1^n + 2m F_2^n) \right]$$
$$* (\vec{\sigma}(1) \times \vec{Q})_{\pm} |\vec{p}'', \vec{q}'' \rangle \left\langle \vec{p}'', \vec{q}'' - \frac{2}{3}\vec{Q} \middle| \vec{p}, \vec{q} \right\rangle.$$

(2.65)

In Eq. (2.64) and Eq. (2.65) we present a conventional and spin currents which combined form a spatial component of the single nucleon current $\vec{j^1}(0)$. Here I use a model of M. Garu and W. Krümpelmann [?] for which:

$$F_1^p(0) = 1 \qquad\qquad 2m F_2^p(0) = 1.793 \qquad (2.66)$$
$$F_1^n(0) = 0 \qquad\qquad 2m F_2^n(0) = -1.913 \qquad (2.67)$$

2.7 Pion absorption

For the pion absorption I include explicitly two nucleon current (2NC) as well as 1NC. Thus the absorption operator $\rho = \rho(1) + \rho(1, 2)$, where obsorption on a single nucleon is included in $\rho(1)$ and $\rho(1, 2)$ plays a role of two-body charge current. The matrix element of the single nucleon pion absorption operator $\rho(1)$ in momentum-space for nucleon 1 relies on the nucleon's incoming momentum ($\mathbf{p}$) and outgoing momentum ($\mathbf{p}'$) [?]:

$$\langle \mathbf{p}' | \rho(1) | \mathbf{p} \rangle = -\frac{g_A M_\pi}{\sqrt{2} F_\pi} \frac{(\mathbf{p}' + \mathbf{p}) \cdot \boldsymbol{\sigma}_1}{2M} (\boldsymbol{\tau}_1)_- , \qquad (2.68)$$

where the values of the nucleon axial vector coupling, pion decay constant, and negative pion mass are $g_A = 1.29$, $F_\pi = 92.4 \, \text{MeV}$, and $M_\pi = 139.57 \, \frac{\text{MeV}}{c^2}$, respectively. $\rho(1)$ operates in the spin and isospin spaces and involves the Pauli spin (isospin) operator σ_1 (τ_1) for nucleon 1 and the isospin lowering operator $(\boldsymbol{\tau}_1)_- \equiv ((\boldsymbol{\tau}_1)_x - \text{i}(\boldsymbol{\tau}_1)_y)/2$. As before we use the average "nucleon mass" $M \equiv \frac{1}{2} (M_p + M_n,)$ where the proton mass is M_p and neutron mass is M_n.

The 2N part of ρ at LO has the form [?]

$$\langle \mathbf{p}'_1 \, \mathbf{p}'_2 | \rho(1, 2) | \mathbf{p}_1 \, \mathbf{p}_2 \rangle = (v(k_2) \mathbf{k}_2 \cdot \boldsymbol{\sigma}_2 - v(k_1) \mathbf{k}_1 \cdot \boldsymbol{\sigma}_1)$$
$$\times \frac{i}{\sqrt{2}} \left[(\boldsymbol{\tau}_1 \times \boldsymbol{\tau}_2)_x - i (\boldsymbol{\tau}_1 \times \boldsymbol{\tau}_2)_y \right] , \qquad (2.69)$$

where $\mathbf{k}_1 = \mathbf{p}'_1 - \mathbf{p}_1$, $\mathbf{k}_2 = \mathbf{p}'_2 - \mathbf{p}_2$ and the formfactor $v(k)$ reads

$$v(k) = \frac{1}{(2\pi)^3} \frac{g_A M_\pi}{4 F_\pi^3} \frac{1}{M_\pi^2 + k^2} . \qquad (2.70)$$

In case of the pion absorption process we follow a standard procedure including partial wave states for both 2N and 3N induced nucleus. For 2N this is $\langle \mathbf{p} + \frac{1}{2} \mathbf{P}_f | \rho(1) | \mathbf{p} - \frac{1}{2} \mathbf{P}_f + \mathbf{P}_i \rangle$ while for 3N case $\langle \mathbf{q} + \frac{1}{3} \mathbf{P}_f | \rho(1) | \mathbf{q} - \frac{2}{3} \mathbf{P}_f + \mathbf{P}_i \rangle$.

For the $\pi^- + {}^2\text{H} \rightarrow n + n$ reaction, the nuclear matrix element for the transition operator is given by:

$$N_{nn}(m_1, m_2, m_d) = {}^{(-)} \langle \mathbf{p}_0 \, m_1 \, m_2 \, \mathbf{P}_f = 0 | \rho | \phi_d \, m_d \, \mathbf{P}_i = 0 \rangle , \qquad (2.71)$$

where $| \mathbf{p}_0 \, m_1 \, m_2 \, \mathbf{P}_f = 0 \rangle^{(-)}$ denotes the 2N scattering state [?].

The total absorption rate for this matrix would be:

$$\Gamma_{nn} = \frac{(\alpha \, M'_d)^3 \, c \, M_n \, p_0}{2 M_{\pi^-}} \int d\hat{\mathbf{p}}_0 \, \frac{1}{3} \sum_{m_1, m_2, m_d} |N_{nn}(m_1, m_2, m_d)|^2 . \qquad (2.72)$$

Turning to 3N system I investigate pion absorption in ${}^3\text{He}$ or ${}^3\text{H}$ with various final states. For $\pi^- + {}^3\text{He} \rightarrow n + d$ reaction the most important step in obtaining predictions is calculating the matrix element of the 3N transition operator ρ_{3N}, which is the ρ acting between the initial ${}^3\text{He}$ and the final 3N scattering state immersed in 3N space:

$$N_{nd}(m_n, m_d, m_{^3\mathrm{He}}) \equiv {}^{(-)}\langle \Psi_{nd}\, m_n\, m_d\, \mathbf{P}_f = 0 | \rho_{3N} | \Psi_{^3\mathrm{He}}\, m_{^3\mathrm{He}}\, \mathbf{P}_i = 0 \rangle. \tag{2.73}$$

Given Eq. (2.73) the total absorption rate may be obtained from the following:

$$\Gamma_{nd} = \mathcal{R}\, \frac{16\left(\alpha^3 M'_{^3\mathrm{He}}\right)^3 c\, M q_0}{9 M_{\pi^-}} \int d\hat{\mathbf{q}}_0\, \frac{1}{2} \sum_{m_n, m_d, m_{^3\mathrm{He}}} |N_{nd}(m_n, m_d, m_{^3\mathrm{He}})|^2, \tag{2.74}$$

where $M'_{^3\mathrm{He}} = \frac{M_{^3\mathrm{He}} M_{\pi^-}}{M_{^3\mathrm{He}} + M_{\pi^-}}$ is now the reduced mass of the $\pi^- - {}^3\mathrm{He}$ system. The factor $\mathcal{R} = 0.98$ appears due to the finite volume of the ^{3}He charge [?]. The final state energy is expressed in terms of the neutron momentum $\mathbf{q}_0$

$$M_\pi + M_{^3\mathrm{He}} \approx M_n + M_d + \frac{3}{4}\frac{\mathbf{q}_0^{\,2}}{M}, \tag{2.75}$$

The full 3N breakup is calculated in a similar way and the total absorption rate for $\pi^- + {}^3\mathrm{He} \to p + n + n$ reaction is defined as follows

$$\Gamma_{pnn} = \mathcal{R}\, \frac{16\left(\alpha M'_{^3\mathrm{He}}\right)^3 c\, M}{9 M_{\pi^-}} \int d\hat{\mathbf{q}} \int_0^{2\pi} d\phi_p \int_0^\pi d\theta_p \sin\theta_p$$
$$\times \int_0^{p_{max}} dp\, p^2 \sqrt{\frac{4}{3}\left(M E_{pq} - p^2\right)}\, \frac{1}{2} \sum_{m_1, m_2, m_3, m_{^3\mathrm{He}}} |N_{pnn}(m_1, m_2, m_3, m_{^3\mathrm{He}})|^2 \tag{2.76}$$

with

$$N_{pnn}(m_1, m_2, m_3, m_{^3\mathrm{He}}) \equiv {}^{(-)}\langle \Psi_{pnn}\, m_1\, m_2\, m_3\, \mathbf{P}_f = 0 | \rho_{3N} | \Psi_{^3\mathrm{He}}\, m_{^3\mathrm{He}}\, \mathbf{P}_i = 0 \rangle \tag{2.77}$$

E_{pq} is the internal energy of the final 3N state and can be expressed in terms of the Jacobi relative momenta $\mathbf{p}$ and $\mathbf{q}$

$$M_\pi + M_{^3\mathrm{He}} \approx 3M + \frac{\mathbf{p}^2}{M} + \frac{3}{4}\frac{\mathbf{q}^2}{M} \equiv 3M + E_{pq} = 3M + \frac{p_{max}^2}{M} = 3M + \frac{3}{4}\frac{q_{max}^2}{M}. \tag{2.78}$$

In Eq. (2.78) p_{max} and q_{max} are maximal kinematically allowed values of Jacobi momenta. p and q, respectively.

Analogously, the total absorption rate for $\pi^- + {}^3\mathrm{H} \to n + n + n$ reads

$$\Gamma_{nnn} = \frac{2\left(\alpha M'_{^3\mathrm{H}}\right)^3 c\, M}{27 M_{\pi^-}} \int d\hat{\mathbf{q}} \int_0^{2\pi} d\phi_p \int_0^\pi d\theta_p \sin\theta_p$$
$$\times \int_0^{p_{max}} dp\, p^2 \sqrt{\frac{4}{3}\left(M E_{pq} - p^2\right)}\, \frac{1}{2} \sum_{m_1, m_2, m_3, m_{^3\mathrm{He}}} |N_{nnn}(m_1, m_2, m_3, m_{^3\mathrm{He}})|^2 \tag{2.79}$$

with

$$N_{nnn}(m_1, m_2, m_3, m_{^3\mathrm{H}}) \equiv {}^{(-)}\langle \Psi_{nnn}\, m_1\, m_2\, m_3\, \mathbf{P}_f = 0 |\, \rho_{3N}\, |\Psi_{^3\mathrm{H}}\, m_{^3\mathrm{H}}\, \mathbf{P}_i = 0 \rangle\, , \quad (2.80)$$

In the Results section I also demonstrate predictions of the differential absorption rates. The natural domain is that defined on energies of outgoing mucleons (E_1, E_2); in such a case the differential absorption rate $d^2\Gamma_{pnn}/(dE_1\, dE_2)$ expresses as

$$\frac{d^2\Gamma_{pnn}}{dE_1\, dE_2} = \mathcal{R}\, \frac{64\,\pi^2\, \left(\alpha\, M'_{^3\mathrm{He}}\right)^3\, c\, M^3}{3 M_{\pi^-}}$$
$$\times \frac{1}{2} \sum_{m_1, m_2, m_3, m_{^3\mathrm{He}}} |N_{pnn}(m_1, m_2, m_3, m_{^3\mathrm{He}})|^2\, . \quad (2.81)$$

The kinematically allowed region is restricted to energies fulfilling the condition $-1 \leq \frac{E - 2E_1 - 2E_2}{2\sqrt{E_1\, E_2}} \leq 1$.

One can also calculate differential absorption rate with respect to the dimensionless variables x and y which are frequemtly used in the literature, specifically to build so-called Dalitz plots [?]

$$\begin{aligned} x &= \sqrt{3}\,(E_1 + 2E_2 - E)/E\,, \\ y &= (3E_1 - E)/E\,.cutoff \end{aligned} \quad (2.82)$$

Such definition leads to simple kinematically allowed region, namely to the disk $r^2 \equiv x^2 + y^2 \leq 1$. One can evaluate $d^2\Gamma_{pnn}/(dx\, dy)$ or (using polar coordinates) $d^2\Gamma_{pnn}/(dr\, d\phi)$ and relate it with $\frac{d^2\Gamma_{pnn}}{dE_1 dE_2}$.

2.8 Theoretical uncertainties

Striving to achieve valuable theoretical results, we cannot omit the estimation of their uncertainty. There are various sources of presictions uncertainty. The three most important are: the truncation error, the cutoff dependance and the uncertainty related to various models of the nuclear interaction. The latter can be easily estimated by computing predictions arising from various models, see discussion below. The way how to estimate the first two types of uncertainies, together with a short discussion of remaining types of uncertainies are given below.

Truncation error

As it was mentioned above, each subsequent order of the chiral expansion provides us with more and more sophisticated potential which is expected to increase accuracy of data description. Starting from the leading order (LO) and coming next to N2LO, N3LO etc., we take into account more topologies (equivalents of Feynmann diagrams) and in result potential is expected to provide us with more precise predictions for the regarded process and observables. However, the chiral expansion (as any expansion) in principle can be continued up to the infinity, improving the resulting series. In practice we are limited to a finite, rather small, orders and we would like to find out the uncertainty

appearing from cutting off the remaining part of the expansion. That type of theoretical uncertainty is called a truncation error. Various methods to estimate its value have been proposed [?, ?, ?, ?, ?]. Typically predictions at lower orders serve as input information to get truncation error at given order. It is worth adding that Bayesian analysis is also used for truncation error estimation.

We use the method proposed in [?]. Let us regard some prediction $X^i(p)$ for observable X which is calculated at i-th order of the chiral expansion with the expansion parameter Q ($i = 0, 2, 3...$)[1]. Here p specifies a momentum scale of the reaction. In the case of photodisintegration p is given by a photon's momentum.

If we define the difference between observables at each subsequent orders as:

$$\Delta X^{(2)} = |X^{(2)} - X^{(0)}|, \qquad \Delta X^{(i>2)} = |X^{(i)} - X^{(i-1)}|, \qquad (2.83)$$

than chiral expansion for X can be written as:

$$X = X^{(0)} + \Delta X^{(2)} + \Delta X^{(3)} + ... + \Delta X^{(i)}. \qquad (2.84)$$

The truncation error at i-th order, $\delta X^{(i)}$, is estimated using values of the observable obtained at lower orders as following:

$$\delta X^{(0)} = Q^2 \left| X^{(0)} \right|, \qquad (2.85)$$
$$\delta X^{(i)} = \max_{2 \leq j \leq i} \left(Q^{i+1} \left| X^{(0)} \right|, Q^{i+1-j} \left| \Delta X^{(j)} \right| \right). \qquad (2.86)$$

Additionally, following [?] I use the actual high-order predictions (if known) in order to specify uncertainties at lower orders, so that:

$$\delta X^{(i)} \geq \max_{j,k}(|X^{j \geq i} - X^{k \geq i}|) \qquad (2.87)$$

and to be conservative I use additional restriction:

$$\delta X^{(i)} \geq Q \delta X^{(i-1)}. \qquad (2.88)$$

All the conditions above assume that we use the whole available information at hand. In [?] it was shown that such method is equivalent to the Bayesian approach proposed there.

Cut-off dependence

Another theoretical uncertainty comes from the choice of the cutoff parameter's value of regulator described in the Chapter 1.

In the case of the SMS interaction its free parameters have been obtained from data for four values of the cutoff parameter Λ: 400, 450, 500 and 550 MeV [?]. Using each of these values, one obtains different predictions which, of course, can further differ from actual (experimental) value. Therefore the choice of Λ value may affect a quality of the prediction.

---

[1] As mentioned in Sec. 1, we do not have a first order of expansion because this term in chiral expansion is always vanished and NLO corresponds to the quadratic term (number 2)
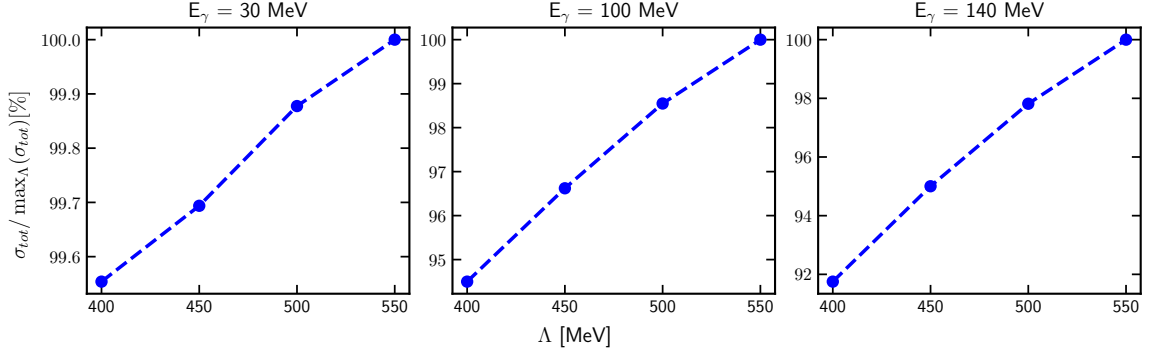
Figure 2.3: Total cross section of the deuteron photodisintegration process (normalized to the maximal cross section among all Λ) as a dependance on the cutoff parameter Λ for three photon energy E_γ values: 30, 100 and 140 MeV.

To study that I also use the same four values of the Λ parameter, obtaining in that way set of four predictions each time. That is exemplified in Fig. 2.3 for the deuteron photo-disintegration cross section for the photon's energy $E_\gamma = 30\,\text{MeV}$, $100\,\text{MeV}$ and $140\,\text{MeV}$. The SMS model at N^{4}LO$^+$ with two-nucleon force is used. Each subfigure shows predictions for the total cross section as a function of the cutoff parameter, normalized to the maximum value among all cross sections obtained with various Λ. As we can see, for that observable there is almost linear dependance with positive linearity coefficient value: with higher Λ the cross section value increases as well. Note that the higher photon's energy is, the stronger becomes the cutoff dependance: for $E_\gamma = 30\,\text{MeV}$ the maximal difference between predictions is around $0.5\,\%$ while for $140\,\text{MeV}$ it increases to more than $8\,\%$. This results are generally within our expectations that the chiral model works better at smaller energies and is therefore less sensitive to the Λ value. Let us remind that Λ governs the behavior of the potential at small internucleon distances and only higher energy transfer probes that distances.

Other theoretical uncertainies

There are obviously more sources of theoretical uncertainties. Our model has a number of either intrinsic limitations in precision or some simplifications which may be improved with further developments of the model.

Nuclear currents At the moment, our model is limited to a single nucleon current, which may not be sufficient to accurately describe the processes under consideration. This limitation will be further discussed and tested in Chapter 3. To address this issue, we utilize the Siegert theorem, which enables us to incorporate some contributions from the two-nucleon current, although it does not yet complete a job. It is worth noting that the incorporation of the two-nucleon current can significantly affect the predicted observables, as it includes additional physical effects that are not accounted for in the single nucleon current. Therefore, the ongoing development of a complete chiral two-nucleon current is of great importance for our model to improve the accuracy of the predictions.

Nonrelativistic approach All the results presented here does not include relativistic corrections. At the lower energies the relativistic contribution might not be crucial, but at the region with higher energy we may see a lack of precision. This will be also confirmed and discussed regarding the total cross section for the deuteron photodisintegration (see Fig. 3.2).

Uncertainties in the potential free parameters Since the chiral potential is of a semi-phenomenological type, the fitting procedure is applied in order to obtain the potential parameters [?]. The values of the free parameter of the SMS NN potential as well as free parameters of the 3N interaction have been obtained from the data by the least square fitting. As any fitting procedure, it introduces an uncertainty to the obtained values which depends on the algorithm's precision as these values are actually estimators of expectation values only. This errors, in principle, are being propagated to the observables as different set of parameters leads to a different predictions. Indead, in [?] the whole correlation matrix for free parameters of the SMS NN force is given. Using that knowledge, it is possible to study the propagation of the uncertainty of NN force parameters to 3N observables. It is done in [?, ?] for the elastic and inelastic nucleon-deuteron scattering. Resulting uncertainies have been found to be much smaller (typically one order of magnitude) than uncertainies arising from truncation errors or cutoff dependance. I expect the same uncertainty level in electromagnetic processes and thus I do not intend to study that theoretical error in the presented thesis. Moreover, estimation of such errors is computationally expensive, since it requires significant amount of computer processing power (separate calculations for each set of parameters). In future it could be interesting to check that type of uncertainty for photodisintegration processes but it should be done after completing all pieces of Hamiltonian specifically after including many-body electromagnetic currents.

Uncertainties from the numerical method All my results base on numerical calculations, so we can come up with a lot of places were numerical methods with limited precision come into the scene. Our approach is based on the partial wave decomposition and in practice only limited number of partial waves is included (usually for 2N scattering we use all channels up to $j^{max} = 4$ which corresponds to 18 partial waves). For 3N calculations we use $J^{max} = 15/2$ *???* which corresponds to 142 partial waves. In addition, I work with some grid of points which is used for the calculation of potential, wave function, numerical integration etc. The choice of grid affect a final results' precision. Usually, we use a grid of *72??* values which was proven to make resulting uncertainty small [?].

Model choice I focus on the SMS potential, but using another model of interaction in general leads to different predictions. That difference is also a theoretical uncertainty thus we use predictions obtained with the semiphenomenological AV18 model in order to compare the chiral results. The AV18 model is a widely used and well-established model of nuclear interaction, which has been extensively tested and benchmarked against experimental data. By comparing the predictions obtained from the SMS potential with those obtained from the AV18 model, we can assess the robustness (comparing to the AV18 results) of our results and determine the extent to which they depend on the choice of the interaction model. This comparison also helps to identify the strengths and

weaknesses of each model and provides insights into the underlying physics of nuclear interactions.

Machine precision Finally, it should be noted that every computer calculation includes limited numerical machine precision which can be noticeable for complex calculations. We perform our calculations via CPU machine, where the particular choice of the processor and memory card may lead to numerical uncertainty. However, we have found that this uncertainty is much smaller than the uncertainties discussed above, and its impact on our results is negligible. We have taken great care to ensure that our calculations are performed using appropriate numerical methods and sufficient computational resources to minimize any numerical errors that may arise.

CHAPTER 3

RESULTS

In this chapter, I will present the results of my calculations. I will begin with the deuteron photodisintegration process in Section 3.1, where I will provide predictions for the cross section (Subsection 3.1.1) and polarization observables (Subsection 3.1.2). Next, in Section 3.2, I will present my predictions for the observables in ^{3}He photodisintegration. Moving on to Section 3.3, I will illuminate the results of calculations for Triton photodisintegration observables. Finally, in Section 3.4, I will discuss the results of the calculations for the pion absorption from the lowest atomic orbital of ^{2}H, ^{3}H, and ^{3}He.

3.1 Deuteron photodisintegraion

3.1.1 Cross section

In this section I will show the results of my calculation starting from the deuteron photodisintegration process. One of the most studying observable is obviously the cross section. There is a number of papers which present measurement results for both differential and total cross section [?, ?, ?, ?, ?, ?, ?, ?, ?] and it is interesting to compare our predictions with that experimental results.

In Fig. 3.1 and Fig. 3.2 I present predictions for the total cross section σ_{tot} [μb] which I obtained using the chiral SMS potential at the N^{4}LO$^+$ order and with the cut-off parameter $\Lambda = 450$ MeV. From Fig. 3.1, we see that at low photon energies (below 50 MeV) both 1NC predictions and results which include 2N contributions to the electromagnetic current via the Siegert approach, describe experimental results quite well quantitavely. We observe that predicions based on the 1NC describe the data only up to approx. 10 MeV. Beyond that energy the 1NC current is clearly not enough to describe cross section as corresponding predictions are clearly below the data. In that region 1NC+Siegert predictions deliver better data description but overestimate the data. The difference between 1NC and 1NC+Siegert cross section grows with increasing photon energies. At 5 MeV the difference between 1NC predictions and 1NC+Siegert is 297.54 µb (10.8 %), increasing energy to 10 MeV it is 304.28 µb (20.4 %) and at 20 MeV it is 229.50 µb (39.2 %).

Here and later the relative difference between set of predictions $(x_1, x_2, ..., x_N)$ is calculated using the formula:

$$\Delta = \frac{\max(x) - \min(x)}{\frac{1}{N}\sum_{i=1}^{N} x_i} \cdot 100\%, \tag{3.1}$$

so in the specific case of comparison the date with 1NC current and "1NC + Siegert" we calculate relative difference as $\Delta = \frac{|\sigma^{1NC+Siegert} - \sigma^{1N}|}{0.5(\sigma^{1NC+Siegert} + \sigma^{1N})}$.

From Fig. 3.1 we see that the gap between these predictions continues increasing even more with larger energies. This tells us that the Siegert approach works quite well as no additional 2N contributions are taken into account. The cross section predictions corrected via Siegert 2N contribution reproduce experimental data to some extend.

Fig. 3.1 reveals the approximated charachter of the Siegert approach. It is clear that one has to take with causion Siegert predictions at very small energies. Also above 20 MeV there is a gap between Siegert results and experimental data, which points that more elaborated 2N current should be included in future. The observed discrepancy cannot be explained by the cut-off dependance (see e.g. Fig. 3.5b below) or by the low order of chiral potential (see discussion below).

While my main goal is to describe deuteron photodisintegration at energies $E_\gamma \lesssim$ 50 MeV, where predictions seem to describe experimental data reasonably well, it is also interesting to check how present theory works at higher energies. Above $E_\gamma = 50$ MeV we can notice that the discrepancy with experimental data is not only quantitative, but also qualitative see Fig. 3.2. This starts already above $E_\gamma = 50$ MeV and is especially pronounced at peak around 300 MeV seen in the experimental data from [?] which is not reflected in my predictions. The reason of such discrepancy is most likely coming from the relativistic effects which we do not take into account within this work. It is also confirmed by the calculations in [?], where authors discuss various NN potentials applied to the deuteron photodisintegration. Despite using much simpler models of the nuclear force than those used in this thesis, their predictions, which include some relativistic effects, show that such a peak appears in their predictions.

In Fig. 3.3 I present the total cross-section for the deuteron photodisintegration at three photon energy values: 30, 100 and 140 MeV as a function of the chiral order. Error bars show truncation errors calculated using Eq. 2.85 - 2.88. One can see that the truncation errors are being reduced with each consecutive chiral order. At LO uncertainty is the biggest: 29.46 % at $E_\gamma = 30$ MeV, 29.46 % at $E_\gamma = 100$ MeV and 41.82 % at $E_\gamma = 140$ MeV. At N^{4}LO$^+$ it is hardly visible at presented scale and amounts up to 1.3 % for each energy(however decreasing with the chiral order). For each energy the prediction is within the uncertainty range at lower orders. We see that at lower energy σ_{tot} already at NLO reaches valve which remains practically unchanged at higher orders. Contrary, at two higher energies, contributions from higher orders are necessary to obtain stable predictions up to approx. N^{3}LO.

Figures 3.4 and 3.5 show my predictions for the differential cross section $\frac{d\sigma}{d\Omega}$. In both figures the top, middle and bottom row shows predictions at $E_\gamma = 30$, 100 and 140 MeV, respectively. For all predictions, the contributions of the 2N current are taken into account via the Siegert theorem, and unless stated otherwise, I utilize the SMS N^{4}LO$^+$ potential. The left column of Fig. 3.4 shows the predictions obtained at different chiral orders (from LO to N^{4}LO$^+$) and with $\Lambda = 450$ MeV. Looking at the best predictions (N^{4}LO$^+$, $\Lambda = 450$ MeV) for each energy, I conclude that the higher photon energy is, the larger difference between the theoretical predictions and experimental data is. At $E_\gamma = 30$ MeV (top panel) my predictions almost perfectly match the data and the difference is almost always within the tripled experimental uncertainties. Moving to $E_\gamma = 100$ MeV (middle
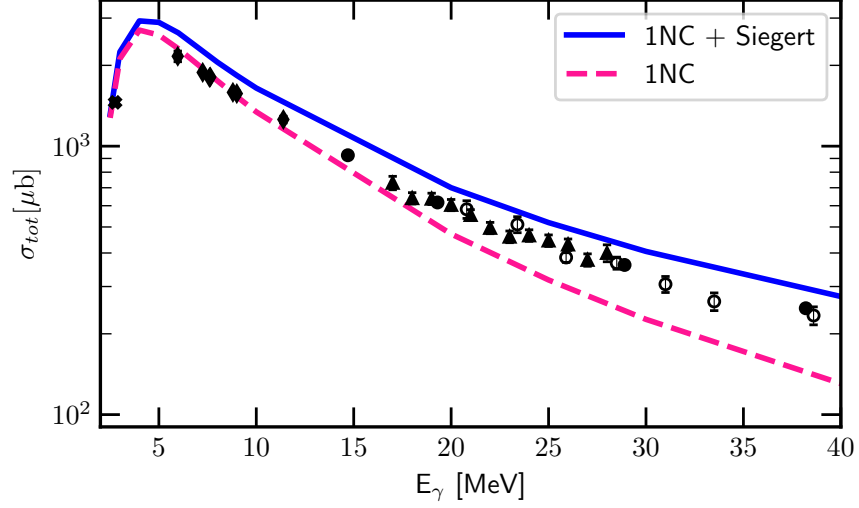
Figure 3.1: Total cross section σ_{tot} for the deuteron photodisintegration process as a function of the photon energy E_γ. Solid blue line presents results obtained with 1NC+Siegert and dashed pink line - predictions based on the 1NC. In both cases the SMS N^{4}LO$^+$ $\Lambda = 450$ MeV force is used. The experimental data are from [?] (black filled circles), [?] (empty circles), [?] (triangles), [?] (bold cross "X") and [?] (diamonds).
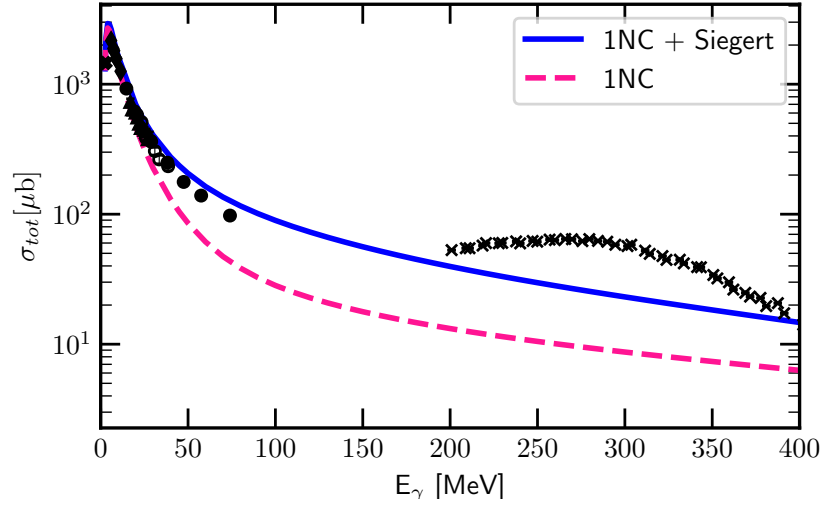

Figure 3.2: The same as in Fig. 3.1 but for the energy range 2.5 - 400 MeV. The experimental data are the same as in Fig. 3.1 but supplemented by the data above $E_\gamma = 200$ MeV from [?] (crosses).

row) the description of the data is deteriorating: theoretical predictions still match the data qualitatively, but the gap for proton emission angle θ_p in range ($60° < \theta_p < 130°$) is up to 32 % (of the predicted value) and relative difference (calculated with Eq. (3.1)) is up to 7 %. At the highest energy (bottom row), it is even hard to say about good qualitative description: the general trend of the angular dependence is presented, but the predictions are far from the experimental points. The relative difference between
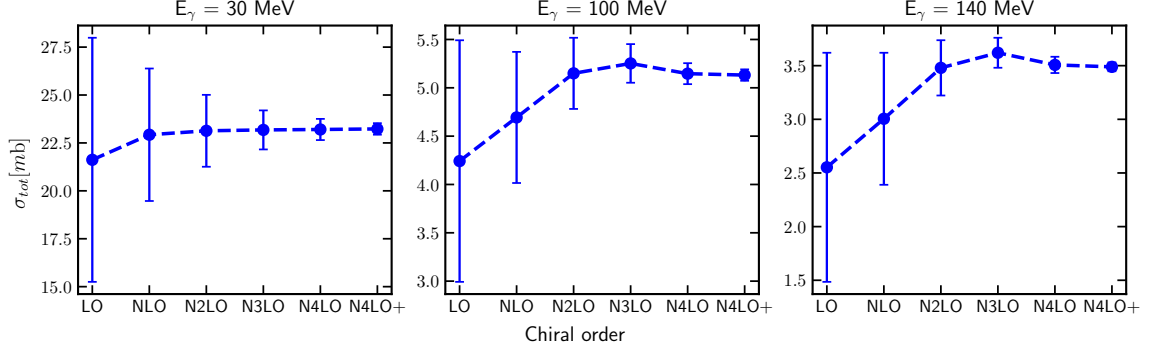
Figure 3.3: Total cross section of the deuteron photonisintegration process as a dependence on the chiral order for three photon energy E_γ values: 30, 100 and 140 MeV. Error bands show an estimated truncation error at each order.

experimental data and predictions obtained with N^4LO+ and $\Lambda = 450$ MeV at 30 MeV is less then 13 % and absulute difference is $< 3.07\,\frac{\mu b}{sr}$. At 100 MeV descripancy is larger and relative difference reaches 46% with absolute difference up to $1.39\,\frac{\mu b}{sr}$. Coming to 140 MeV the relative difference increases up to 48.6 % and absolute - $1.93\,\frac{\mu b}{sr}$. What may be helpful for a better data description is a 2N current and relativistic correction, mentioned earlier. We observe improvements introduced by each subsequent chiral order, but stabilization shows that some ingredients beyond 2N potential are missing.

Obtained results at each energy confirm the convergence of the predictions with respect to the chiral order. We see that the cross section at LO is far from both experimental data and the most advanced N^4LO^+ predictions, and the higher photon energy, the larger this difference is. With each subsequent chiral order, the curves are more closer to each other and the difference between N^4LO and N^4LO^+ is hardly visible at scale used in Fig. 3.3. The relative difference between these two predictions at $E_\gamma = 30$ MeV around the point of maximum ($\theta_p = 80°$) is 0.05 % which is $0.02\,\frac{\mu b}{sr}$; at 100 MeV and $\theta_p = 107°$ it is 0.79 % ($0.025\,\frac{\mu b}{sr}$); and at 140 MeV (same angle) it is 1.8 % ($0.043\,\frac{\mu b}{sr}$). Having such a small differences between predictions from two highest chiral orders, I can conclude that predictions are converged and using NN potential beyond N^4LO^+ chiral orders would rather not bring significant contribution to the cross section values. The difference with experimental data is systematic and is not related with the chiral order.

Predictions obtained with the AV18 potential (dashed-dotted purple line in the Fig. 3.4 left) are very similar to these from the N^4LO^+ SMS force at lower energies (relative difference at $E_\gamma = 30$ MeV is 0.06 % at the point of maximum $\theta_p = 80°$) and with increasing energy to 140 MeV it growes up to 3.1 % at the same scattering angle. It can be connected with our potential's quality loss, but AV18 can be struggling with high energies as well. That once again shows that other components of Hamiltonian become important at that energies.

In the right column of the Fig. 3.4 I compare predictions based on various assumptions on nuclear current and dynamical mechanism. I again use SMS N^4LO^+, $\Lambda = 450$ MeV force. At the lowest energy predictions comprising the plane-wave component only (without rescattering part) and taking currents as SNC+Siegert, show relatively small deviation from the full predictions, but the difference increases at larger energies. With $E_\gamma = 30$ MeV the relative difference is 10 % ($4.03\,\frac{\mu b}{sr}$) at $\theta_p = 80°$. Difference at 100 MeV and the same angle is 4 % ($0.21\,\frac{\mu b}{sr}$) and at 140 MeV it is 7 % ($0.21\,\frac{\mu b}{sr}$). In contrast,

predictions without two-body current component (1NC) have much larger gap with full prediction: the difference is 46.5% ($13.67\frac{\mu b}{sr}$) at $30\,\mathrm{MeV}$, 78.6% ($2.88\frac{\mu b}{sr}$) at $100\,\mathrm{MeV}$ and 77.8% ($1.68\frac{\mu b}{sr}$) at $140\,\mathrm{MeV}$ at the same $\theta_p = 80°$. Obviously 2NC contributions are extremely important in this case, the difference connected with them is much bigger then theoretical uncertainties or even rescattering contribution. For other scattering angles, especially $\theta_p = 0°$ or $\theta_p = 180°$, the role of two-body current or FSI is relatively even more pronounced.

The Fig. 3.5 (left) presents theoretical truncation uncertainties. That confirms our expectations that for the regarded photo reaction chiral order N^4LO^+ is able to produce converged predictions: the black band (representing truncation error at N^4LO^+) is hardly visible for the $E_\gamma = 30\,\mathrm{MeV}$ (the relative error for N^4LO^+ at $80°$ is only 0.12%) and is also quite narrow for larger energies (at $140\,\mathrm{MeV}$ the error at the same angle is 1.46%). At the lower chiral orders, this band is obviously much wider: at N^2LO it is 1.25% at $E_\gamma = 30\,\mathrm{MeV}$ and 15.0% at $E_\gamma = 140\,\mathrm{MeV}$. I note, that the magnitude of the truncation error only very tiny depends on the scattering angle.

Last but not least, in the right column of Fig. 3.5 I show the cut-off dependence of the differential cross section. In the ideal case that dependence is so weak that the choice of the parameter Λ would not introduce significant changes. In practice the choice of this parameter is important as it makes a noticeable variation in prediction at higher energies. Namely, while at $E_\gamma = 30\,\mathrm{MeV}$ the cut-off dependence is so tiny that, in fact, all the lines (for different Λ values) overlap each other and we cannot distinguish them with the naked eye: the relative difference at the maximum of the cross section is 0.08%. This is approximately $\frac{2}{3}$ smaller than truncation error discussed above. However, with increasing photon energy up to $100\,\mathrm{MeV}$ and $140\,\mathrm{MeV}$ (middle and bottom rows of the right column of Fig. 3.5) the spread becomes bigger: the uncertainty related to the Λ-dependence is 3.35% at $100\,\mathrm{MeV}$ and 5.66% at $140\,\mathrm{MeV}$ (the same θ_p). Thus at two higher energies the cut-off dependence becomes more important than truncation errors. That shows, that proper choice of the Λ is important. However, if I restrict myself to $\Lambda = 450\,\mathrm{MeV}$ and $500\,\mathrm{MeV}$, the dependence drops to 1.98% at $E_\gamma = 140\,\mathrm{MeV}$. Such a restriction is advocated by better description of the scattering data delivered by the SMS potential for that two values of Λ.

In the Fig. 2.3 we have already seen that the total cross section for the same energies has the cut-off spread around 4.5% for $100\,\mathrm{MeV}$ and 8% for $140\,\mathrm{MeV}$ For $E_\gamma = 30\,\mathrm{MeV}$ it is below 1%. It means that even cut-off dependance for that total cross section (affected by the extreme values close to $\theta_p = 0$ or $\theta_p = 180$) are relatively small, especially at the lower energies.
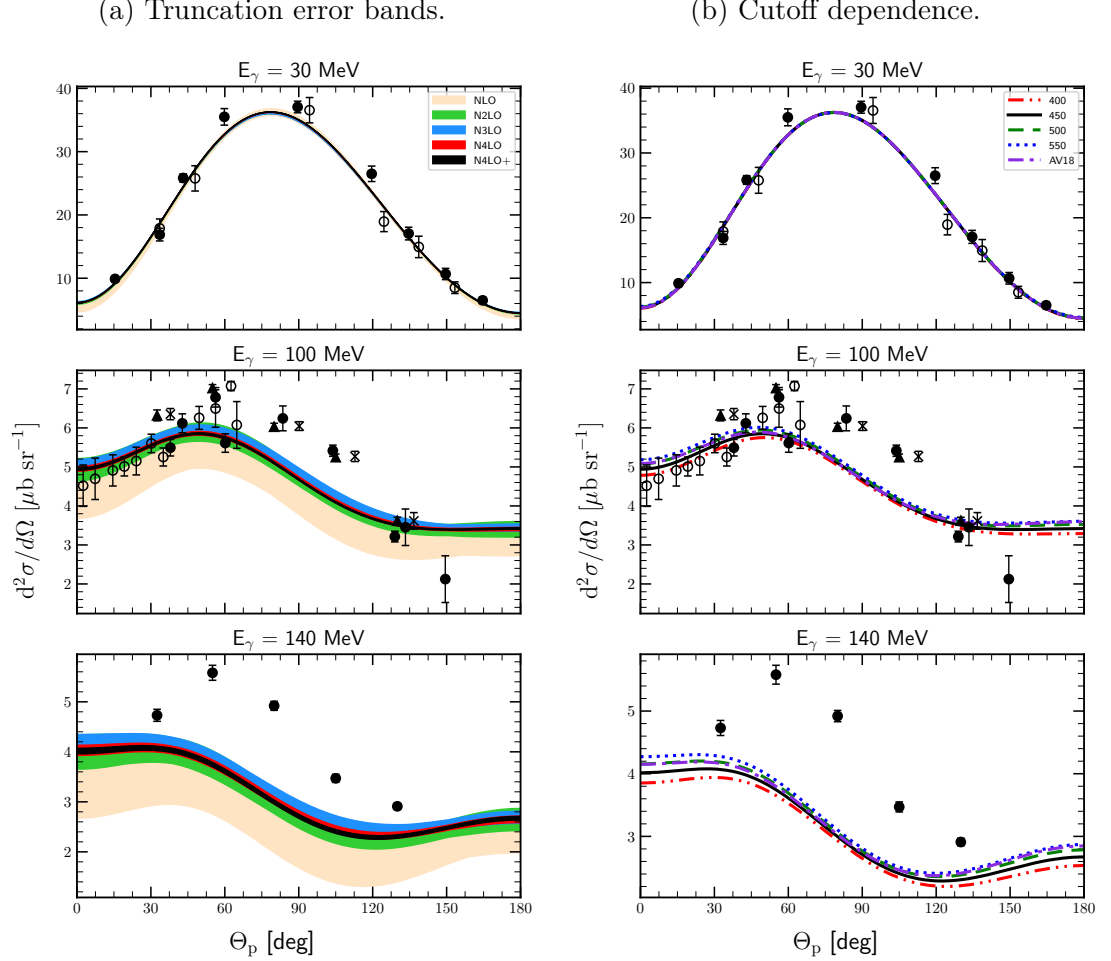
Figure 3.4: Differential cross section $\frac{d^2\sigma}{d\Omega}$ as a function of the outgoing proton momentum polar angle θ_p in the center of mass frame for the photon energy 30 MeV (top), 100 MeV (middle) and 140 MeV (bottom). **(a)** Results obtained using the SMS potential at different chiral orders (from LO to N^{4}LO$^+$) with the cut-off parameter $\Lambda = 450$ MeV and 2NC contributions taking via the Siegert theorem. For the sake of comparison, predictions obtained with the AV18 potential are shown by dashed-dotted purple line. Data points (filled and empty circles) are from [?] for E$_\gamma$ = 30 and 100 MeV and from [?] for E$_\gamma$ = 140 MeV. **(b)** Predictions obtained with the chiral N^{4}LO$^+$ potential and $\Lambda = 450$ MeV with various models of nuclear current and scattering state. The blue solid curve represents our most complete predictions comprising the plane-wave plus rescattering parts and 1NC+Siegert current propagator (the same as N^{4}LO$^+$ line in (a)). The pink dashed curve shows predictions obtained with the single-nucleon current only (without applying the Siegert theorem) and the green dashed-dotted curve represents predictions with the full current (1NC + Siegert) but plane-wave part only.

(a) Truncation error bands.

(b) Cutoff dependence.

Figure 3.5: Theoretical uncertainies for the differential cross section $\frac{d^2\sigma}{d\Omega}$ as a function of the outgoing proton's momentum polar angle θ_p in the center of mass frame for the photon energy is 30 MeV (top row), 100 MeV (middle row) and 140 MeV (bottom row). **(a)** The truncation error bands obtained using the SMS potential at different chiral orders (from NLO to N⁴LO⁺) with the cut-off parameter $\Lambda = 450$ MeV and 2NC contributions taking via the Siegert approach. **(b)** Results obtained using different values of the cut-off parameter Λ. The double-dotted-dashed red curve, the solid black line, the dashed green line and the dotted blue line represent predictions obtained with $\Lambda = 400$, 450, 500 and 550 MeV respectively and the chiral potential N⁴LO⁺. Data points are the same as in Fig. 3.4a

3.1.2 Polarization observables

In this subsection I will present my predictions for the selected polarization observables in the deuteron photodisintegration process at two photon energies: $E_\gamma = 30\,\text{MeV}$ and $E_\gamma = 100\,\text{MeV}$. A priori, various polarization states and measurements are thinkable for the $\gamma + d$ scattering. Polarization of the target deuteron leads to the deuteron analyzing power. Similarly using the polarized photons result in the photon asymmetry measurements. Using both polarized photon and deuteron allows for spin correlation measurement. Finely, detecting spin polarization of at least one nucleon in the final state would deliver final polarization or spin transfer coefficients. However, such experiments are very challenging and, up to my best knowledge, have not been done yet at regarded here photon energies. Thus, in the following I will restrict myself to results for polarization observables arising from the polarization of the initial particles.

I start with deuteron vector iT_{11} and tensor T_{20}, T_{21} and T_{22} analyzing power, which arise from various spin state of the deuteron.

Deuteron tensor analyzing powers can be calculated via cross section as it is defined in [?]:

$$\frac{d\sigma}{d\Omega} = \frac{d\sigma_0}{d\Omega} \left\{ 1 - \sqrt{3/4} P_z \sin\theta_H \sin\phi_H T_{11} + \sqrt{1/2} P_{zz} \left[\left(3/2\cos^2\theta_H - 1/2 \right) T_{20} - \right.\right.$$
$$\left.\left. -\sqrt{3/8}\sin 2\theta_H \cos\phi_H T_{21} + \sqrt{3/8}\sin^2\theta_H \cos 2\phi_H T_{22} \right] \right\}, \quad (3.2)$$

where σ_0 is the unpolarized cross section, P_z (P_{zz}) the vector (tensor) target polarization, θ_H - the angle between polarization axis and photon momentum, and ϕ_H - is the angle between the polarization plane (containing the polarization axis and momentum of the photon), and the reaction plane (containing momenta of the proton and neutron).

In the Figures 3.6 (a, b) and 3.7(a,b) I show my predictions at $E_\gamma = 30\,\text{MeV}$, for the T_{20}, T_{21}, T_{22} and iT_{11} respectively as functions of the outgoing proton momentum polar angle θ_p in the centre of the mass (CM) frame. Each of them is organized in the similar way: the top panel shows a dependence of the predictions on the chiral order of the potential. The middle subfigure is showing a correspondent truncation error for each of the predictions from a top row (except LO, because its uncertainty is too large and will spoil clarity of the figure). The last (bottom) panel shows the cut-off dependence at the chiral order N^4LO^+. All results have been obtained using 1NC+Siegert model of nuclear current.

All the analyzing powers presented here show excellent convergence upon a chiral order as it is hard to distinguish the predictions from each subsequent order starting from the N^2LO. The relative width of the N^4LO^+ truncation band for T_{20}, T_{21} and T_{22} are $0.06\,\%$, $0.05\,\%$ and $0.19\,\%$, respectively (at $\theta_p = 90°$, $60°$ and $90°$, respectively). The slowest convergence is observed for iT_{11} (Fig. 3.7b) where we can recognize N^2LO band in the figure. Nevertheless, at the N^4LO^+ the width truncation band at $\theta_p = 20°$ (maximum point) is only a $0.2\,\%$. The cut-off dependence for all regarded observables is weak and predictions for each value of the Λ are hardly separable with the naked eye. The relative spread of the predictions based on various Λ at the same angles as above are $0.87\,\%$, $0.94\,\%$, $3.42\,\%$ and $0.68\,\%$ for T_{20}, T_{21}, T_{22} and iT_{11}, respectively.

Corresponding predictions at the photon energy $E_\gamma = 100\,\text{MeV}$ (Figs. 3.8 and 3.9) preserve similar trends for each observable. In general, predictions are being converged starting even from the N^2LO and only for the iT_{11} I find that truncation error's bands

are noticeably wide even at N^4LO and N^4LO^+. Cutoff dependence at this energy is a bit stronger compared to those at $E_\gamma = 30\,\text{MeV}$, especially for T_{22} and iT_{11} analyzing powers (Fig. 3.9 vs Fig. 3.7), where one can see slightly stronger discrepancy at the maxima and minima points.

The choice of Λ does not affect predictions substantially even at that higher energy: the relative spread among all cut-offs for T_{20} is $1.54\,\%$ around the point of maximum ($\theta_p = 90°$). For other components of the tensor analyzing power spread amounts up to: $0.14\,\%$ at $\theta_p = 60°$ for T_{21}; $3.68\,\%$ at $\theta_p = 90°$ for T_{22}; and $4.91\,\%$ at $\theta_p = 75°$ for iT_{11}. We see again that iT_{11} has much larger spread in the maximum and is more sensitive to the cut-off choice. However, summarising my findings for the deuteron tensor analyzing powers, I conclude that cut-off dependence is generally weak also at $E_\gamma = 100\,\text{MeV}$.

Turning our attraction to the chiral order convergence, we observe that predictions are mostly converged starting either from N^2LO or N^3LO. The relative width of N^4LO^+ truncation band for T_{20}, T_{21} and T_{22} are $0.7\,\%$, $0.7\,\%$ and $0.04\,\%$ respectively (at the same angles as used above). Another case is iT_{11}, for which this width is much larger: $6.8\,\%$ at $\theta_p = 20°$. The truncation uncertainty for all analyzing powers is much lower than one, related to the choice of the cut-off parameter. Although, iT_{11} seems to be more sensitive both to the choice of the cut-off parameter and to the chiral order than other regarded observables. Even for iT_{11}, cut-off spread is almost twice larger than truncation error. Standing out of other tensor components, iT_{11} can be useful for the investigation of the cut-off dependence of the model. Of course, we can repeat once more that our model is less accurate at higher energies which is reflected in a stronger cut-off dependence and slower chiral convergence. However, I conclude that even at these energies tensor analyzing powers are well converged with respect to the chiral order.

Comparison of the predictions obtained using the chiral N^4LO^+ potential $\Lambda = 450\,\text{MeV}$ with ones obtained taking AV18 potential show a very good agreement: the relative difference at $E_\gamma = 30\,\text{MeV}$ is below $6\,\%$ for the regarded tensor analyzing powers at specified angles. Picture at $E_\gamma = 100\,\text{MeV}$ is even better: the difference does not exceed $4\,\%$ for all observables and whole range of scattering angles.

In Fig. 3.10 together with our most advanced "Full" predictions (N^4LO^+, $\Lambda = 450\,\text{MeV}$, the Siegert theorem), at $E_\gamma = 30\,\text{MeV}$ I show predictions obtained with 1NC only and the Siegert predictions but with plane-wave contribution without rescattering part. In the case of deuteron's tensor analyzing power components, the contribution of rescattering part is imortant for T_{20}, T_{21} and T_{22} (the relative difference is up to $20\,\%$ in extremes). and crucial for iT_{11} where the PW part equals to zero. The 2NC component taken into account via Siegert theorem has a dominant contribution here. We see that 1NC predictions are absolutely away from the "Full" predictions and in case of iT_{11} does not even reflect complete prediction qualitatively.

Fig. 3.11 presents similar results but for $E_\gamma = 100\,\text{MeV}$ and it is intersting that the difference between Full and 1NC prediction becomes smaller and it is especially visible for T_{22}. At this energy the relative difference between "Full" and 1NC predictions at $\theta_p = 90°$ is $43.6\,\%$ comparing to $122.8\,\%$ at $E_\gamma = 30\,\text{MeV}$. Similarly, the difference for T_{20} at $E_\gamma = 30\,\text{MeV}(\theta_p = 90°)$ is $91.4\,\%$ and at $E_\gamma = 100\,\text{MeV}$ it drops to $28.8\,\%$. This may also be affected by the fact that values at $\theta_p = 90°$ are quit small for the Full prediction, nevertheless the difference still becomes smaller at the $E_\gamma = 100\,\text{MeV}$. This trend is noticeable looking also on results presented below. Nevertheless, in both cases 2NC (via the Siegert) bring sufficient contributions and cannot be omitted for the full picture.

In the following figures, I will compare my predictions with experimental data. In some cases I will keep a similar way as it was done in [?] where due to experimental conditions results are given not at single photon energy, but for a specific ranges of E_γ. In the Figures 3.12 - 3.18 I show an angular dependence of the T_{2i} ($i = 0, 1, 2$) for a specific energy bands: 25–45 MeV, 45–70 MeV, 70–100 MeV, and 230–330 MeV. Solid blue line shows an average value of the observable in the specified energy intervals: obtained at N^4LO^+ with $\Lambda = 450$ MeV, while the pink dashed line is a prediction obtained with a same setup but without using a contributions from Siegert approach (single nucleon current only). Bands for each of prediction specify the spread of predictions due to the energy band.

One clearly sees that the data description is better for the predictions with Siegert contributions included and the 1NC alone is not able to describe experiment properly. Our Full model nicely describes data up to $E_\gamma = 70$ MeV. With increasing energy (above 100 MeV), the difference between predicted values and experimental data becomes larger (especially for T_{22}), which shows a neccesity of improving theoretical model befor applying it to higher energies. Nevertheless, even with approximations used, the data description remains reasonable. We observe that quite often and in particular in Fig. 3.17 and Fig. 3.18 the data description is worse for smaller angles. Especially for the tensor analyzing power T_{22} the group of data point lying closer to $\theta_p = 30°$ are farther from the theoretical prediction than second group. In Fig. 3.18 the description of data points for T_{20} seem to be better with the 1NC (dashed line), but in this case it is only accidental match as we do not observe similar trend for any other angular range or for different observable. In addition, experimental uncertainties are larger at small angles and in all cases our description is inside 3σ uncertainty.

In the Figure 3.19 the energy dependence of T_{20} and T_{22} at specific angle $\theta_p = 88°$ is presented for the energy range 0-400 MeV. Beside my predictions I also demonstrate the experimental data from [?] and [?] as well as theoretical calculations from [?]. For T_{20} all models are able to describe experimental data well even for high energies. On the other hand, T_{22} is not described so well: for the energies below 140 MeV the predictions are within uncertainties of experimental data, but further the difference with the data increases. Above 140 MeV my Full predictions do not reflect the qualitative nature of the data. Namely, I observe that data points start ascending which is not represented in my predictions. Theoretical predictions from [?] (brown dashed curve) are also not able to describe data quantitatively for T_{22}, but increasing of T_{22} towards data is present. The predictions in [?] are obtained with a one-body current using the Bonn one-boson-exchange potential in coordinate space (OBEPR) NN potential with the major part of meson exchange currents (MEC) included implicitly via the Siegert operators plus explicit pion exchange currents (MEC), isobar configurations (IC) and the leading order relativistic corrections (RC). So authors use a different potential, but probably the main difference of predictions is coming from the more advance model of the current operator and the RC included there. We see that experimental errors are quite large which is not so surprising giving that the experiment was conducted back in 1989. New experiments would be a great support in development of the nuclear interactions as we expect relativistic calculations in future [?].

The Fig. 3.20 presents similar results to the Fig. 3.19 but with various values of the cutoff parameter. The deviation between these predictions is rather small (especially below 150 MeV), while the difference with the calculation from [?] and experimental data remains as discussed above.

Similar picture is seen in the Figures 3.21 and 3.22 where I show an energy dependence of the mean of deuteron analyzing powers over specific angular ranges (following the data from [?]). In Fig. 3.21 we see that only predictions for T_{20} are able to reflect the experimental results, while for T_{21} and T_{22} my results are reasonable (quantitative-wise) only for lower energies and difference with data becomes larger when energy increases. Predictions for T_{21} and T_{22} once more confirm an insufficiency of 1NC and an importance of 2-nucleon current contributions. The description is better for bigger angles Fig. 3.22): at lower energies (below 140 MeV) the correspondence to experimental data is good for all three observables, but above that threshold, all predictions (especially for T_{22}) move away from the measurements data. Again, big uncertainty of the data calls for experiment to be repeated.

In the Fig. 3.23 I demonstrate predictions for the photon asymmetry Σ_γ for the deuteron photodisintegration with $E_\gamma = 20$ MeV (a) and 60 MeV(b) together with the experimental data of [?, ?, ?, ?]. Both (a) and (b) figures are organized similarly to the figures I showed above for the tensor analyzing powers (e.g. Fig. 3.7). That is the top panel is aimed to demonstrate predictions obtained with the chiral SMS potential at different orders of the chiral expansion, the middle one is showing a truncation errors and the bottom one shows the cut-off dependence. For that observable we see an excellent convergence with respect to the chiral order. For both regarded energies predictions at different orders are very close to each other except the LO and NLO curves. Nevertheless, at $E_\gamma = 60$ MeV the truncation error bands reveal some uncertainty connected with the chiral order and it is expected that even some higher chiral orders would still contribute to the predictions at this energy. The relative width of the truncation band are 0.26 %, 5.04 %, 5.05 %, 5.73 % and 14.96 % for N^4LO^+, N^4LO, N^3LO, N^2LO and NLO respectively and at $\theta_p = 90°$.

The cut-off dependence is also much stronger at 60 MeV. One clearly sees that predictions are different for various values of the Λ. The relative difference between predictions to the cut-off parameter at 20 MeV is 0.26 % while at the photon energy 60 MeV it is 4.41 % (both calculated at $\theta_p = 90°$). So the theoretical uncertainty related to regulator value is nearly 17 times bigger that due to the truncation error ($4.11/0.26 = 16.96$).

Comparing my predictions to experimental data, I observe that for the lower energy predictions are almost perfectly overlapping with experimental points within the error bars. For a few data points our predictions are outside data error bars, but they are still within 3σ range. For 60 MeV, experimental data points are systematically below theoretical curves, especially in the middle of angular range. It seems that some systematic uncertainty is presented in predictions and ad hoc multiplication by some factor (around 0.8) could help predictions be more similar to experimental data. But very likely the observed discrepancy points to simplified character of the model used here.

In the Fig. 3.24 the predictions obtained with Full set of components (plane wave + rescattering and 1NC + Siegert, solid blue curve) are shown versus predictions obtained without rescattering (green dashed-dotted line) and without contribution from the Siegert (pink dashed line) for the same photon energies as above: $E_\gamma = 20$ MeV (left panel) and $E_\gamma = 60$ MeV (right panel). For the $E_\gamma = 20$ MeV the difference between Full and PW is quit small, whereas 1NC is noticeably differs from the Full prediction, especially around the smallest and largest angle values. For the $E_\gamma = 60$ MeV the difference between such a predictions is larger: we see not only quantitative, but also a qualitative variations. The 1NC curve has much larger values and its shape becomes more asymmetric with respect to the $\theta_p = 90°$ point.

In the Fig. 3.25 (left) I present a dependence of the photon asymmetry Σ_γ on the photon energy at a fixed value of the outgoing proton polar direction $\theta_p = 90°$ (following the data given at [?] and [?]). It is noticeable that with increasing energy, the predictions are systematically above the experimental data and the discrepancy growths with energy. This trend was also observed in the angular dependence of the asymmetry at 60 MeV so I conclude that within our framework, Σ_γ is sensitive to the initial photon energy and some theoretical contributions are missing in order to get satisfactory predictions at higher energies. From the Fig. 3.25 we can say that large discrepancy with data starts already above $E_\gamma = 35$ MeV. [1]

The right panel of the Fig. 3.25 shows an impact of the different model components to the obtained predictions. We see that the difference between the Full predictions (solid blue line) and the one obtained with a 1NC only (without the Siegert contribution) is larger than the difference with predictions with plane-wave part only (without rescattering). Both these incomplete predictions are farther from the experimental data, (for PW at larger energies only) and have a different curve shape as well.

The proton polarization is demonstrated in Fig. 3.26 for the photon energy 30 MeV(a) and 100 MeV(b). In this case even at higher energy (such as 100 MeV) predictions do not reveal neither slower convergence with respect to the chiral order no stronger cut-off dependence. Figures for both energies show that only next-to-leading order brings relatively high contribution while taking into account other subsequent orders does not change predictions significantly. In the case of the cut-off dependence, we see that curves for each value of Λ are very close to each other. The relative difference of the predictions with respect to the cut-off parameter is 4.04 % at the minimum point $\theta_p = 130°$ of $E_\gamma = 30$ MeV and 5.62 % at $\theta_p = 160°$ and $E_\gamma = 100$ MeV. The dependence is slightly stronger for higher energy, but both values are comparable. Again, the cut-off-related uncertainty exceeds the truncation error.

Predictions for the neutron polarization at the energies 2.75 MeV and 100 MeV are shown in the Fig. 3.27. The choice of energy is conditioned by the availability of experimental data, which were taken in 1965 in Livermore [?] and in 1986 at TRIUMF facility [?]. In the case of $E_\gamma = 2.75$ MeV (Fig. 3.27a), we see that predictions reflect the behavior of experimental data points qualitatively, having more o less a constant offset of the values. Similar offset was obtained also in [?], where various approaches were presented. Authors compare different models which leads to a very similar theoretical results even though different potentials are used with and without relativistic correction. One of the theoretical predictions is included even in the experimental papers [?] and authors state that there might be a systematic error in the calibration of the analyzing power of the neutron polarimeter which could affect experimental results precision. Interesting is that predictions clearly show symmetrical form of the curve, while the experimental data have some deviations from symmetrical form. It can be a sign that some problem with data can be in this case (taking into account also that experiment had been done in 1965). In [?] authors even make a plot of theoretical curve multiplied by the factor 0.879 which is almost perfectly overlaps with experimental data afterwards.

At the energy $E_\gamma = 100$ MeV (Fig. 3.27b) my predictions describe the data very well. For most of data points, predicted values are within error bars and only some of points (e.g. around 50°) have prediction in distance more than one standard deviation. Nevertheless, these data points look like being out of general trend and may be a result

---

[1]It is worth to note that data of [?] are above these from [?] (however still inside 3σ experimental error bands) and remain in agreement with my predictions even at $E_\gamma = 60$ MeV.

of imprecise measurement. Observing the stability of my predictions on the chiral order and regulator value I conclude that nucleon polarizations are not the observables, which, even measured with much better precision, than it was done in [**?**] or [**?**] would be an indicator of the model convergence or stability.

Concluding my results of the deuteron photodisintegration predictions, I can point that predictions for $E_\gamma = 30\,\text{MeV}$ (and lower) are very stable with respect to the potential parameters (chiral order or the regulator). It shows an ability for a good data description as well. For a higher energies (especially above $100\,\text{MeV}$) the quality of predictions becomes lower: the dependency on the cut-off value is higher as well as discrepancy with experimental data. Still predictions are converged with respect to the chiral order. The general problem is a lack of 2N current and in case of higher energies - relativistic corrections are missing.

Figure 3.6: The deuteron tensor analyzing powers T_{20} **(a)** and T_{21} **(b)** as a function of the outgoing proton angle θ_p in the centre of the mass frame for the photon energy $E_\gamma = 30\,\mathrm{MeV}$. Top row presents results obtained using the SMS potential at different chiral orders (from LO to N^4LO^+) with the cut-off parameter $\Lambda = 450\,\mathrm{MeV}$. The middle row shows truncation errors for each chiral order starting from NLO and the bottom row presents a cut-off dependence at N^4LO^+. For the sake of comparison, predictions obtained with the AV18 potential are given as well. For all predictions 1NC+Siegert model is used.

Figure 3.7: The same as in Fig. 3.6 but for the deuteron tensor analyzing power T_{22} (left column **(a)**) and the deuteron vector analyzing power iT_{11} (right column **(b)**).

(a) T_{20} (b) T_{21}

Figure 3.8: The deuteron tensor analyzing powers T_{20} **(a)** and T_{21} **(b)** as a function of the outgoing proton angle θ_p in the center of mass frame for the photon energy $E_\gamma = 100\,\mathrm{MeV}$. Top row presents results obtained using the SMS potential at different chiral orders (from LO to N^{4}LO$^+$) with the cut-off parameter $\Lambda = 450\,\mathrm{MeV}$. The middle row shows truncation errors for each chiral order starting from NLO and the bottom row presents a cut-off dependence at N^{4}LO$^+$. For the sake of comparison, predictions obtained with the AV18 potential are given as well. For all predictions 1NC+Siegert model is used.

(a) T$_{22}$
(b) iT$_{11}$

Figure 3.9: The same as in Fig. 3.8 but for the deuteron tensor analyzing power T$_{22}$ (left column **(a)**) and the deuteron vector analyzing power iT$_{11}$ (right column **(b)**).

Figure 3.10: The deuteron tensor analyzing powers T_{20}, T_{21}, T_{22} and the deuteron vector analyzing power iT_{11} as a function of the outgoing proton angle θ_p in the CM frame at $E_\gamma = 30\,\text{MeV}$. Similarly to Fig. 3.4b predictions obtained with chiral N^4LO^+ potential and $\Lambda = 450\,\text{MeV}$ are presented for three theoretical models. Blue solid line is the most complete prediction we have (plane-wave plus rescattering parts, 1NC + Siegert), pink dashed line shows predictions obtained with single-nucleon current only (1NC) - without the Siegert contributions and green dashed-dotted line is a prediction in which we neglect the rescattering part and stick to the plane-wave part only but keeping the Siegert contributions.

Figure 3.11: The same as in Fig. 3.10 but for $E_\gamma = 100\,\mathrm{MeV}$.

Figure 3.12: Tensor analyzing powers T_{20}, T_{21} and T_{22} as a function of the outgoing proton angle θ_p in the CM frame. The solid blue line is a mean value of my predictions obtained at energy values from 25 to $45\,\mathrm{MeV}$ with the SMS potential at N^4LO^+ chiral order and with $\Lambda = 450$ MeV and with 1NC used together with the Siegert approach. The pink dashed line is similar prediction but with the 1NC only. The corresponding bands show the limits of predictions in the regarded energy region. Filled circles are experimental data from [?] for the same energy range.
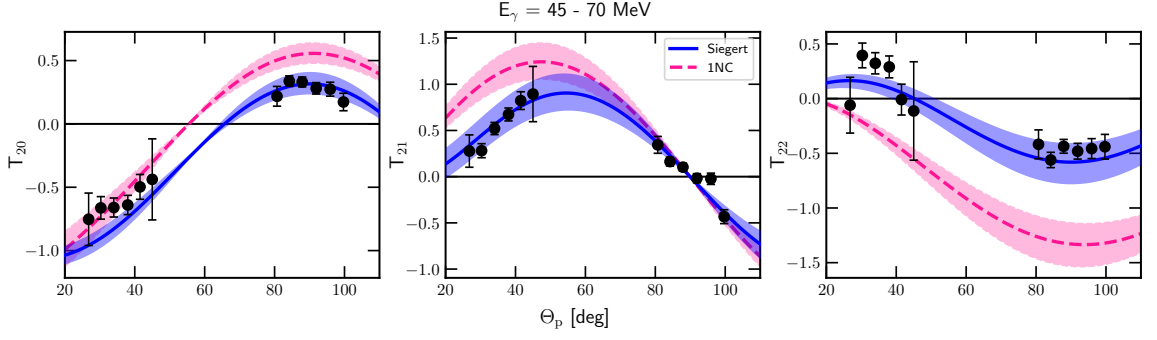
Figure 3.13: The same as in Fig. 3.12 but for energy bin $45 - 70$ MeV.
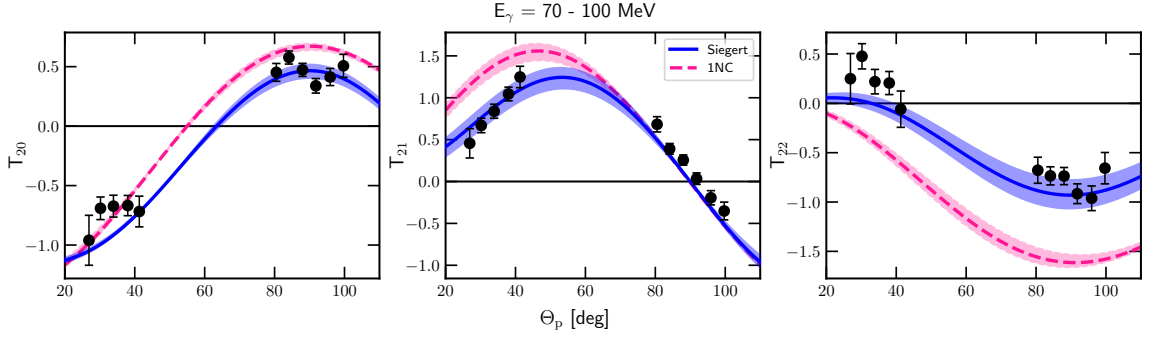
Figure 3.14: The same as in Fig. 3.12 but for energy bin $70 - 100$ MeV.
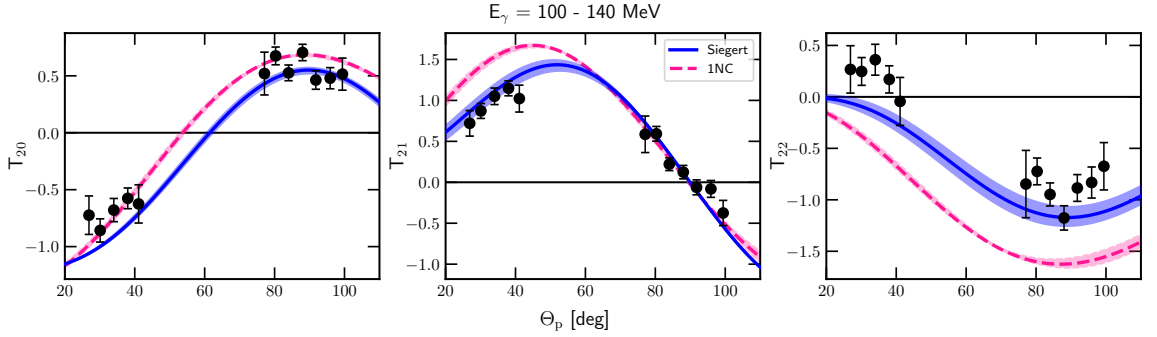
Figure 3.15: The same as in Fig. 3.12 but for energy bin $100 - 140$ MeV.
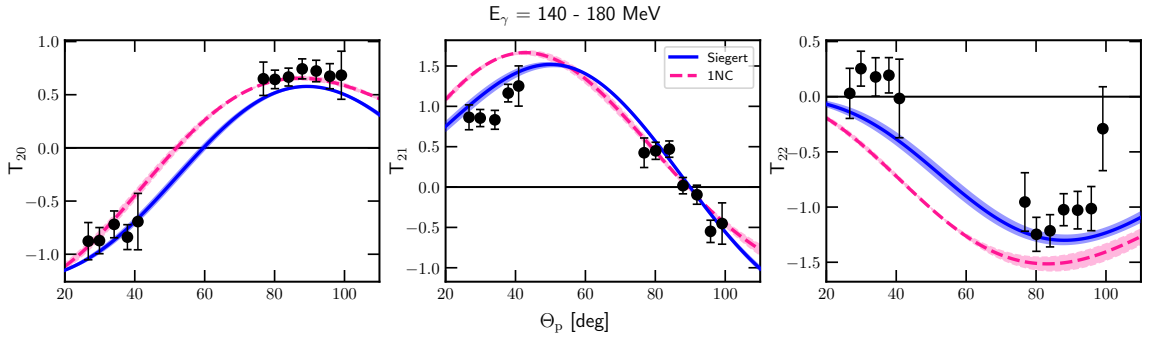
Figure 3.16: The same as in Fig. 3.12 but for energy bin $140 - 180$ MeV

Figure 3.17: The same as in Fig. 3.12 but for energy bin $180 - 230\,\text{MeV}$

Figure 3.18: The same as in Fig. 3.12 but for energy bin $230 - 330\,\text{MeV}$
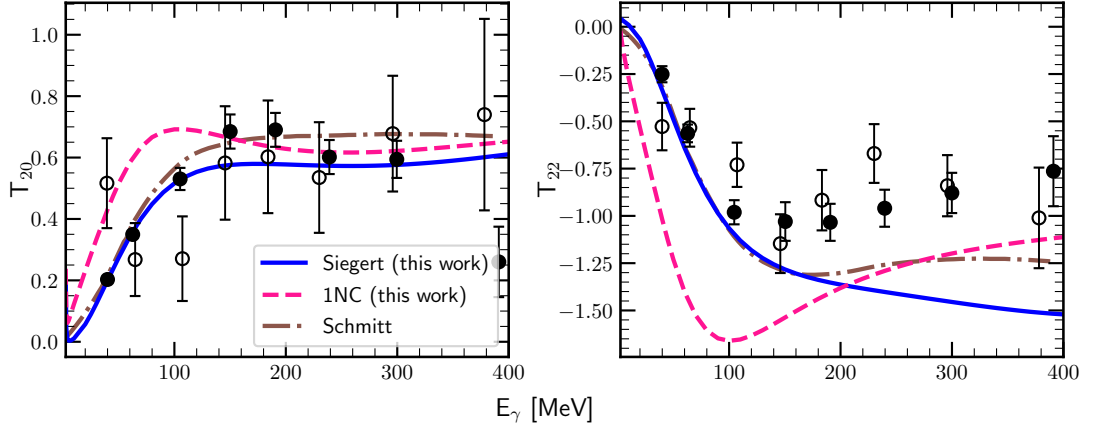
Figure 3.19: The tensor analyzing powers T_{20} (left) and T_{22} (right) as a function of the photon energy E_γ at fixed outgoing proton angle $\theta_p = 88°$ in the center of mass frame. My predictions (blue solid line) are obtained with the SMS potential at the chiral order N^{4}LO$^+$, with the cut-off parameter $\Lambda = 450\,\text{MeV}$ and with 2NC contributions included via the Siegert theorem. The dashed pink curve shows predictions obtained with the same interaction, but without 2NC contributions. The dashed-dotted brown curve presents theoretical results from [?]. Experimental data are taken from [?] (filled circles) and [?] (empty circles).

Figure 3.20: The tensor analyzing powers T_{20} (left) and T_{22} (right) as a function of the photon energy E_γ at fixed outgoing proton angle $\theta_p = 88°$ in the center of mass frame. My predictions have been obtained with the SMS potential at the chiral order N^{4}LO$^+$, with the different values of the cut-off parameter Λ (from 400 MeV to 550 MeV). The dashed-dotted brown curve presents theoretical results from [?]. Experimental data are taken from [?] (filled circles) and [?] (empty circles).

Figure 3.21: The averaged tensor analyzing powers T_{20} (left), T_{21} (middle) and T_{22} (right) as a function of the photon energy for the outgoing proton momentum polar angle θ_p in range $24° - 48°$ in the center of mass frame. The solid blue curve is a mean value of my predictions at energy values ranges from 25 to 45 MeV, obtained with the SMS potential at N^{4}LO$^+$ chiral order and with $\Lambda = 450$ MeV and with 1NC used together with the Siegert approach. The pink dashed curve represents similar predictions but with the nuclear current reduced to the 1NC only. The corresponding bands show predictions at border energies 25 and 45 MeV. The filled circles are experimental data from [?] for the same energy range.
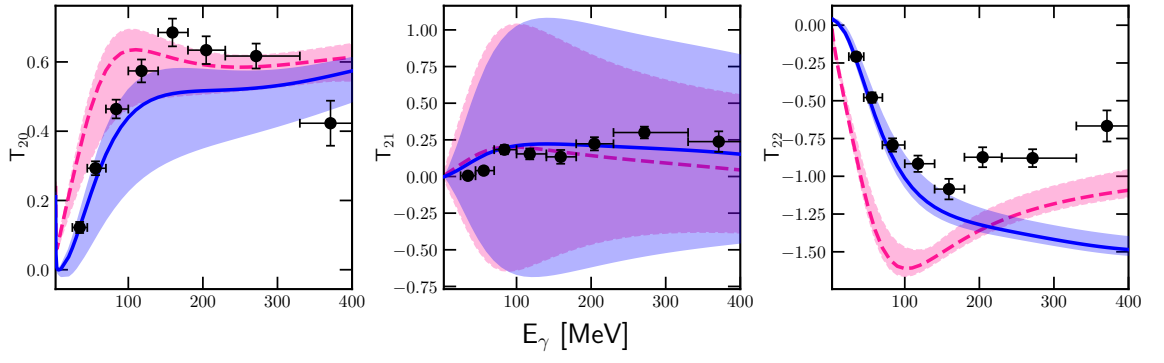
Figure 3.22: The same as in the Fig. 3.21 but for the θ_p in range $70° - 102°$.
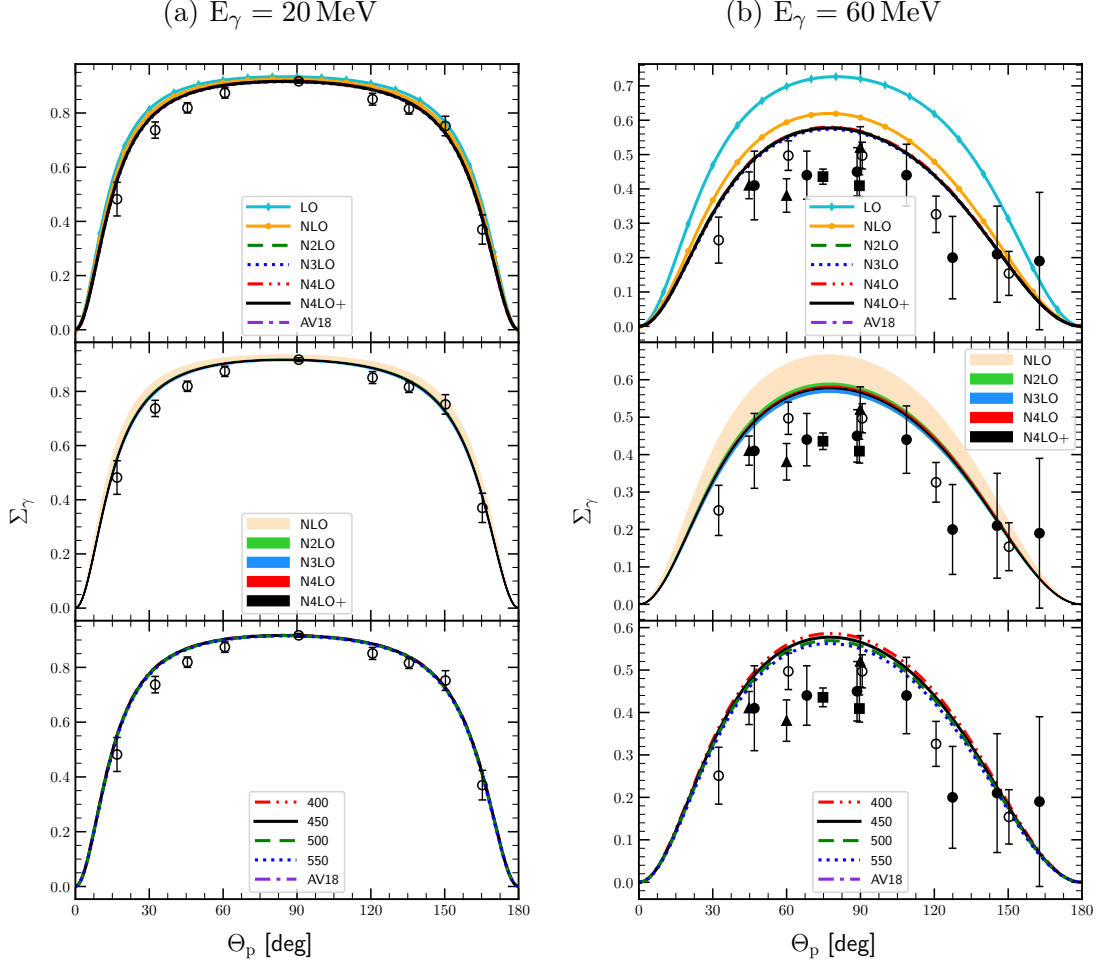
Figure 3.23: The photon asymmetry Σ_γ as a function of the outgoing proton angle in the center of mass frame for the photon energy $20\,\text{MeV}$(a) and $60\,\text{MeV}$(b). Top row presents results obtained using the SMS potential with chiral orders from LO to N^4LO^+ and with the cut-off parameter $\Lambda = 450\,\text{MeV}$. The middle row shows truncation errors for each chiral order starting from NLO and the bottom row presents a cut-off dependence for the chiral potential N^4LO^+. Filled circles are experimental data from [?], empty circles - from [?], filled squares - from [?] and triangles are from [?]. For the sake of comparison, predictions obtained with the AV18 potential are given by the dashed-dotted curve as well.

Figure 3.24: The photon asymmetry Σ_γ as a function of the outgoing proton angle θ_p in the CM frame at $E_\gamma = 20\,\text{MeV}$ (left) and $E_\gamma = 60\,\text{MeV}$(right). Similarly to Fig. 3.4b predictions obtained with chiral N^4LO^+ potential and $\Lambda = 450\,\text{MeV}$ are presented for three theoretical models. Blue solid line is the most complete prediction we have (plane-wave plus rescattering parts, 1NC + Siegert), pink dashed line shows predictions obtained with single-nucleon current only (1NC) - without the Siegert contributions and green dashed-dotted line is a prediction in which we neglect the rescattering part and stick to the plane-wave part only but keeping the Siegert contributions. Filled circles are experimental data from [?], empty circles - from [?], filled squares - from [?] and triangles are from [?].

Figure 3.25: The photon asymmetry Σ_γ as a function of the photon energy at the fixed outgoing proton's momentum polar angle $\theta_p = 90°$. On the left panel each curve corresponds to the particular value of the cut-off parameter and chiral potential used here is the N^{4}LO$^+$ one. On the right panel the blue solid curve represents our most complete predictions comprising the plane-wave plus rescattering parts and 1NC+Siegert current propagator (the same as 450 MeV line in left). The pink dashed curve shows predictions obtained with the single-nucleon current only (without applying the Siegert theorem) and the green dashed-dotted curve represents predictions with the full current (1NC + Siegert) but plane-wave part only. Filled circles are experimental data from [?], empty circles - from [?].

Figure 3.26: Proton polarization $P_y(p)$ as a function of the outgoing proton's momentum polar angle in the center of mass frame with the photon energy $30\,\mathrm{MeV}$ (a) and $100\,\mathrm{MeV}$ (b). Top figures present results obtained using potential with different chiral orders (from LO to $\mathrm{N^4LO^+}$) with cut-off parameter $\Lambda = 450\,\mathrm{MeV}$. The middle panel show truncation errors for each chiral order starting from NLO and bottom figures present a cut-off dependence of predictions based on the SMS $\mathrm{N^4LO^+}$ potential. For the sake of comparison, predictions obtained with the AV18 potential are shown as well.
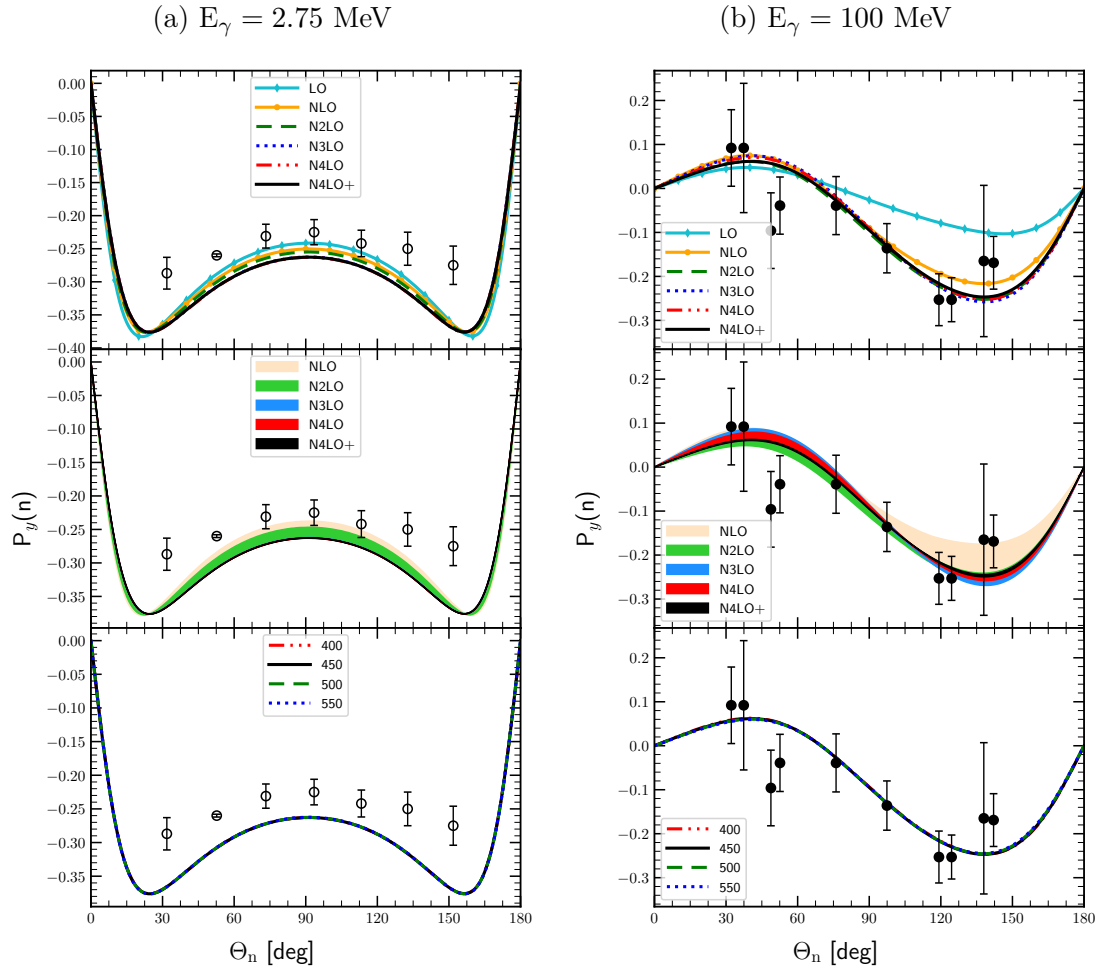
Figure 3.27: The same as in Fig. 3.26 but for the neutron polarization $P_y(n)$ and at photon energies 2.75 MeV **(a)** and 100 MeV **(b)**. Data are from [**?**] (empty circles) and [**?**] (filled circles).

3.2 Helium-3 photodisintegration

3.2.1 Three-body breakup

In this section I will discuss results for $^3\text{He} \to p+p+n$ process differential cross-section obtained with *???* model of nuclear current. For three free nuclepns in the final state it is convenient to introduce, as a kinematical variable, the arc-length of the S-curve. For giving direction of two momenta $\hat{p}_1$ and $\hat{p}_2$, the S-curve spans in the plane defined by kinetic energies of the same two nucleons, E_1 and E_2.

For three particles and known initial energy and momenta five kinematical variables[2] are required to define the final kinematics. We choose four variables as directions of outgoing nucleons no 1 and 2: $\theta_1, \phi_1, \theta_2$ and ϕ_2, with the z-axis aligned to the photon momentum. Choosing E_1 as the fiveth variable would introduce ambiguity, as in some cases two values of E_2 could be allowed. Instead, the location on the S-curve defines the kinematical configuration unambiguousely. The various possible locations of the S-curve in $E_1 - E_2$ plane, as well as the convention on choosing the $S = 0$ point in given in Fig. 1 of [**?**].

In the Fig. 3.28 I demonstrate a differential cross section $\frac{d^5\sigma}{d\Omega_1 d\Omega_2 dS}$ as a function of the S arc length and as in previous section, I study the convergence with respect to chiral order and the cut-off dependance. The photon energy is $\text{E}_\gamma = 30\,\text{MeV}$; the kinematic configuration $\theta_1 = 15°$, $\phi_1 = 0°$, $\theta_2 = 15°$, $\phi_2 = 180°$ and predictions have been obtained without 3NF.[3] On the left we see that only NLO and N^{2}LO introduce relatively large truncation error. The maximal width of a band for NLO is $37.6\,\%$ at $S = 10\,\text{MeV}$, for N^{2}LO it is $12.4\,\%$ at the same S-value and it is gradually decreasing coming to $0.13\,\%$ at N^{4}LO$^+$. The cut-off spread(right) is bigger around maxima values but remains below $3\,\%$. It reaches $0.78\,\%$ at the minimum point ($S = 10\,\text{MeV}$).

With larger energy $\text{E}_\gamma = 100\,\text{MeV}$, for which predictions are demonstrated in the Fig. 3.29, both truncation error and cut-off spread become larger. The truncation band at the maximum point at $S = 10\,\text{MeV}$ for NLO is $55.0\,\%$ decreasing to $2.2\,\%$ at N^{4}LO$^+$ which still is around 3 times larger than it was for predictions at $\text{E}_\gamma = 30\,\text{MeV}$. The cut-off spread also becomes larger with increasing energy value: $9.0\,\%$ at the same (maximum) point which is also ~ 3 times bigger than the one we observed for the lower energy.

Results for the same $\text{E}_\gamma = 100$ MeV but other angular configuration $\theta_1 = 75°$, $\phi_1 = 75°$, $\theta_2 = 75°$, $\phi_2 = 105°$ are given in Fig. 3.30. The top row shows results obtained with 2NF only, while predictions obtained with 3NF are shown on the bottom row. It seems that 3NF does not change much the convergence with respect to the chiral order: truncation error band at the point of maximum $S = 35\,\text{MeV}$ (N^{4}LO$^+$) is $1.11\,\%$ and $1.16\,\%$ with and without 3NF, respectively. As it is almost the same, I conclude that inclusion N^{2}LO 3NF practically does not affect chiral order convergence. Note, 3NF at N^{2}LO has been used for all forces above NLO.

The cut-off dependence, in turn, is affected by the presence of 3NF. Predictions with 2NF only have $13.7\,\%$ spread at the same maximum point $S = 35\,\text{MeV}$, while predictions with 3NF have only $1.23\,\%$ relative spread, so the difference is tremendous.

Similar trends are present also in other configurations, demonstrated for the comparison: Figs.3.31, Figs.3.32 and Figs.3.33.

---

[2]Among nine variables describing final state $\vec{p}_1, \vec{p}_2$ and $\vec{p}_3$, four can be derived from energy and momentum conservation laws.

[3]Different kinematic configurations θ_1, ϕ_1, θ_2 and ϕ_2 have been tested with a step of $15°$ and most interesting cases(showing largest descripancies) are presented in this work.
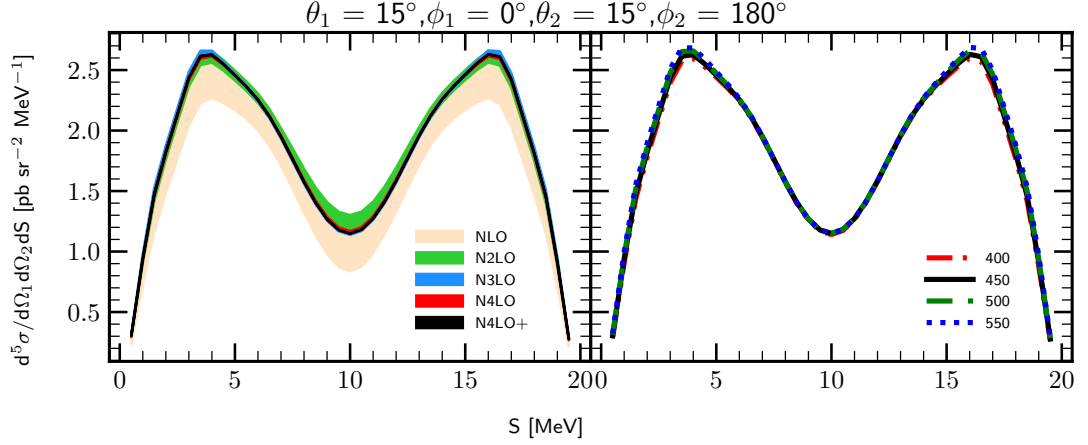
Figure 3.28: The five-fold differential cross section for the photon energy $E_\gamma = 30\,\mathrm{MeV}$ for the kinematic configuration $\theta_1 = 15°$, $\phi_1 = 0°$, $\theta_2 = 15°$, $\phi_2 = 180°$. The left figure presents truncation error bands obtained using the SMS potential with chiral orders from NLO to N^4LO^+, and with cut-off parameter $\Lambda = 450\,\mathrm{MeV}$. The right figure presents a cut-off dependence at N^4LO^+. Results are obtained with two-nucleon force only and 1NC current and Siegert theorem used for a 2NC contributions.

The exclusive cross-sections shown above, in Figs. 3.28-3.33 are small and unfortunately below the possibilities of current experimental techniques. The semi-inclusive measurement is more likely to be performed, thus in Figs 3.34 and 3.35 I show the differential cross section $\frac{d^3\sigma}{d\Omega_p dE_p}$. I choose the same photon energies as above: $E_\gamma = 30\,\mathrm{MeV}$ and $E_\gamma = 100\,\mathrm{MeV}$. Each figure consists of subfigures where each row presents results for a proton momenta polar angle $\theta_p = 10°, 50°, 90°, 130°$ and $170°$. The left part of each subfigure shows detected chiral order dependence while the right - the cut-off dependence.

At the photon energy $30\,\mathrm{MeV}$ the chiral dependence is relatively weak: at the maximum point ($E_p \simeq 3.8\,\mathrm{MeV}$) the relative difference varies between $12\,\%$ and $28\,\%$ at LO for different angles. This difference decreases with each subsequent order resulting in maximum $0.15\,\%$ at N^4LO+. At the energy $E_\gamma = 100\,\mathrm{MeV}$ truncation errors are larger: at the maximum around $E_p \simeq 1.46\,\mathrm{MeV}$ the discrepancy is around $40\,\%$ (NLO), $15\,\%$ (N2LO), coming to $1.5\,\%$ at N^4LO^+.

A typical cut-off uncertainty at $E_\gamma = 30\,\mathrm{MeV}$ is around $2\,\%$ and at $E_\gamma = 100\,\mathrm{MeV}$ increases up to $8\,\%$ for all angles and at the same values of E_p as regarded above.

Observed small uncertainties allow me to conclude that the semi-inclusive cross-section $\frac{d^3\sigma}{d\Omega_p dE_p}$ is not useful in studies aiming on pin-down the details of the chiral force. *do we have prediction with othe current?*

Figure 3.29: The same as in Fig. 3.28 but for the photon energy $E_\gamma = 100$ MeV

Figure 3.30: The same as in the Fig. 3.29 but for the kinematic configuration at $\theta_1 = 75°$, $\phi_1 = 75°$, $\theta_2 = 75°$ and $\phi_2 = 105°$. Results obtained with the chiral SMS 2N force are presented on the top row. The same, but with the N^{2}LO 3NF included is presented on the bottom row (starting from the N^{2}LO - where 3NF appears for the first time).
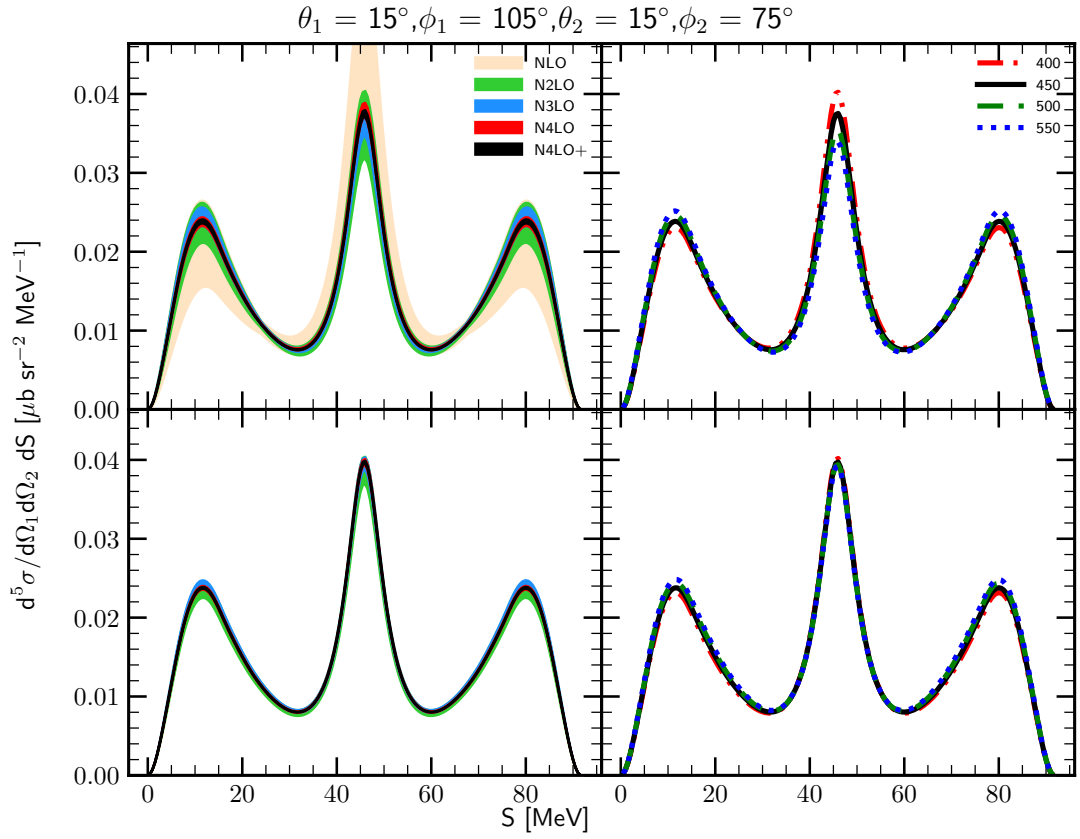
Figure 3.31: The same as in the Fig. 3.30 but for the kinematic configuration at $\theta_1 = 15°$, $\phi_1 = 105°$, $\theta_2 = 15°$ and $\phi_2 = 75°$.
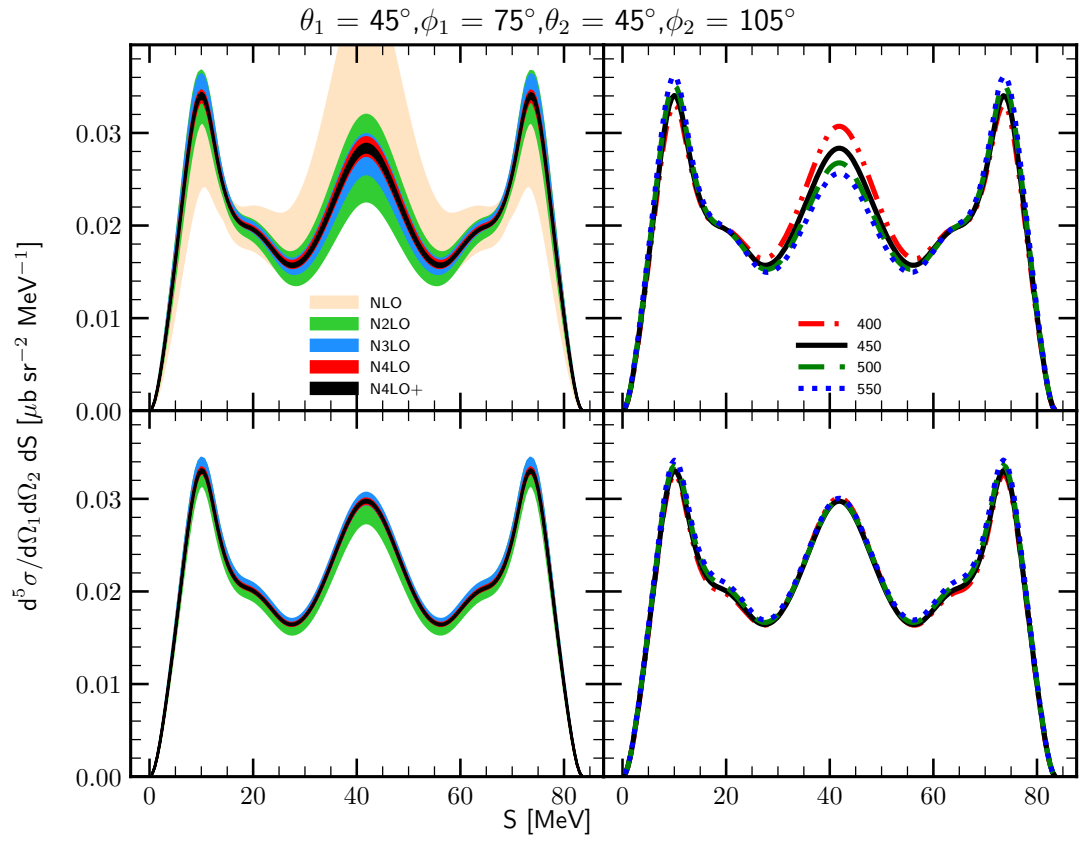
Figure 3.32: The same as in the Fig. 3.31 but for the different kinematic configuration.
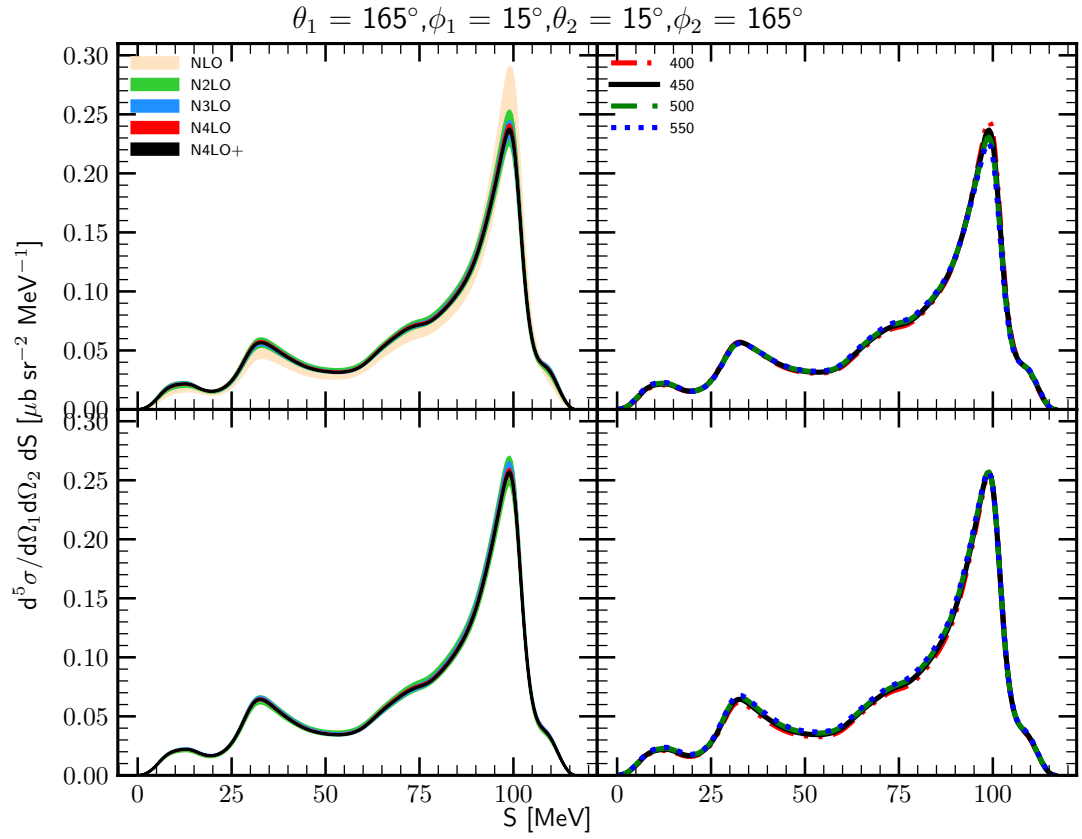
Figure 3.33: The same as in the Fig. 3.32 but for the kinematic configuration at $\theta_1 = 165°$, $\phi_1 = 15°$, $\theta_2 = 15°$ and $\phi_2 = 165°$.
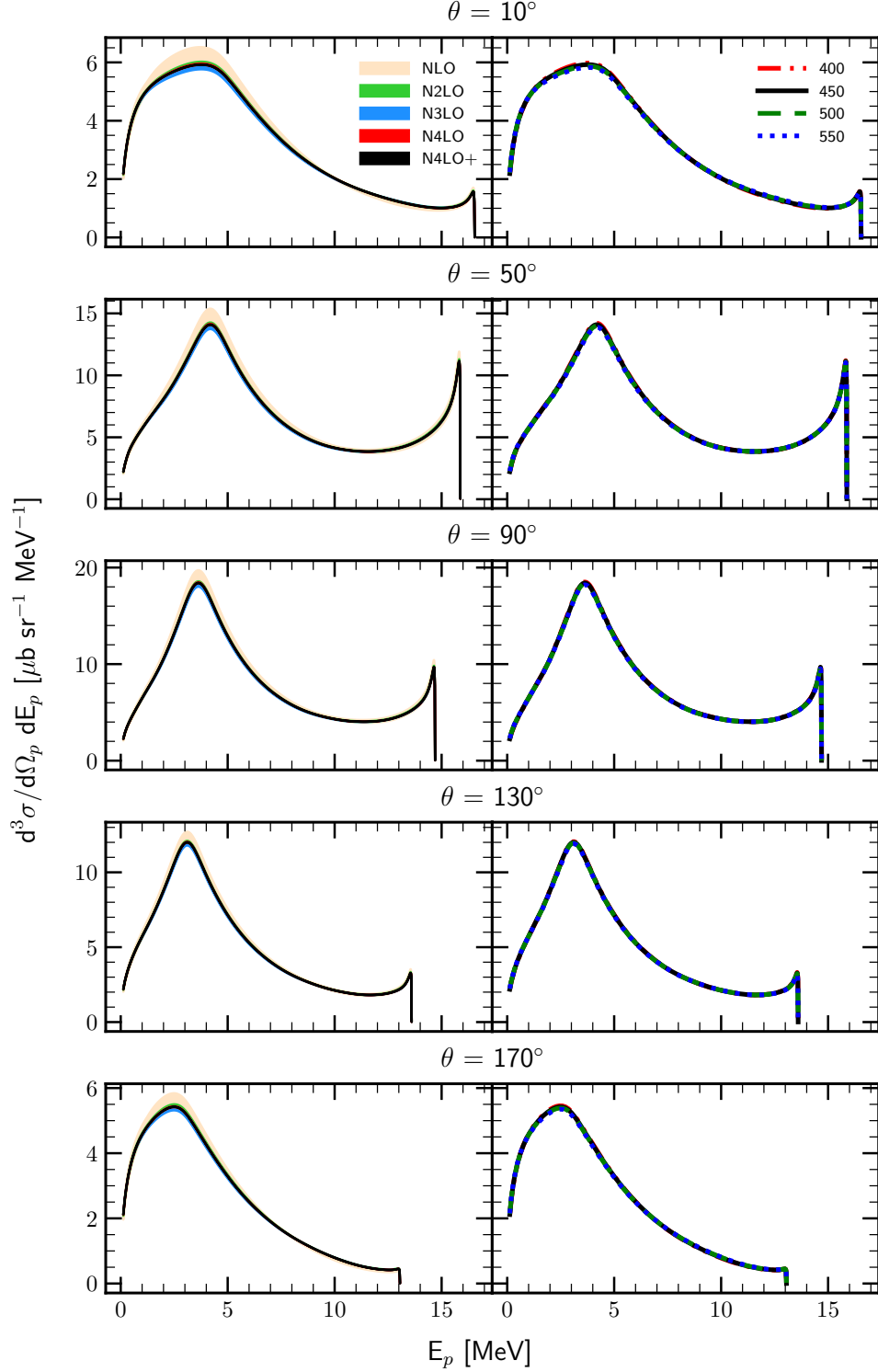
Figure 3.34: The semi-inclusive differential cross section $\frac{d^3\sigma}{d\Omega_p dE_p}$ at $E_\gamma = 30\,\text{MeV}$ $\phi_1 = 0°$ as a function of outgoing proton energy E_p. Each row represents predictions for different values of the outgoing proton's momentum polar angle θ_p: $10°$, $50°$, $90°$, $130°$ and $170°$. The left figure presents truncation error bands obtained using the SMS potential with chiral orders from NLO to N^4LO^+, and with cut-off parameter $\Lambda = 450\,\text{MeV}$. The right figure presents a cut-off dependence at N^4LO^+. Predictions have been obtained with the SMS NN potential but neglecting 3NF.

Figure 3.35: The same as in Fig. 3.34 but for $E_\gamma = 100\,\text{MeV}$.

3.2.2 Two-body breakup

The differential cross section $d\sigma/d\Omega_d$ for the ^{3}He$+\gamma \rightarrow d+p$ reaction is presented in the Fig. 3.36 (for the photon energy $E_\gamma = 30$ MeV) and in the Fig. 3.37 (for $E_\gamma = 100$ MeV). We see a significant enlargement of both truncation and cut-off uncertainties with increasing photon energy. The relative spread of the truncation error at the maximum point ($\theta_p = 105°$) for the lower energy is $0.05\,\%$ at N^{4}LO$^+$, while for the larger energy similar spread is $0.45\,\%$ (at N^{4}LO$^+$, $\theta_p = 120°$).

The cut-off dependence is also stronger for the larger energy: it is $1.45\,\%$ at 30 MeV and $4.01\,\%$ at 100 MeV (at the points of maximum).
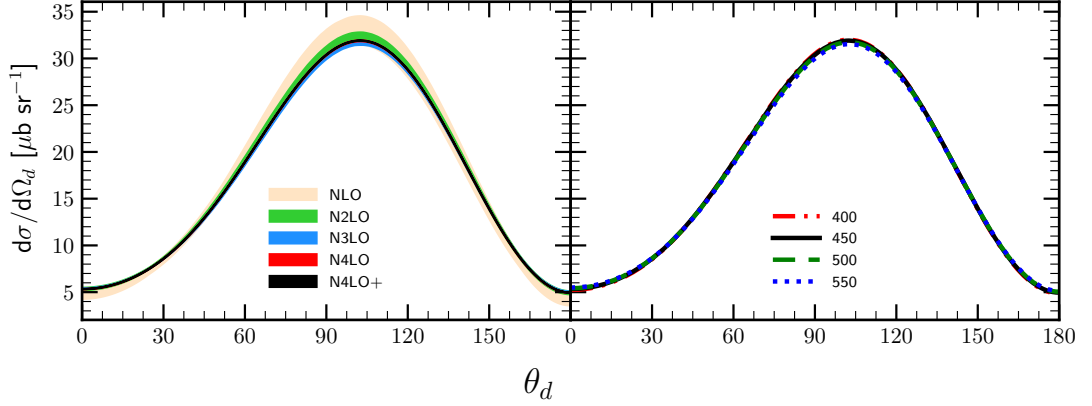
Figure 3.36: Differential cross section for the two-body photodisintegration of ^{3}He as a function of the $d-\gamma$ angle in c.m.. The initial photon energy $E_\gamma = 30$ MeV and NN with 2NF was used.
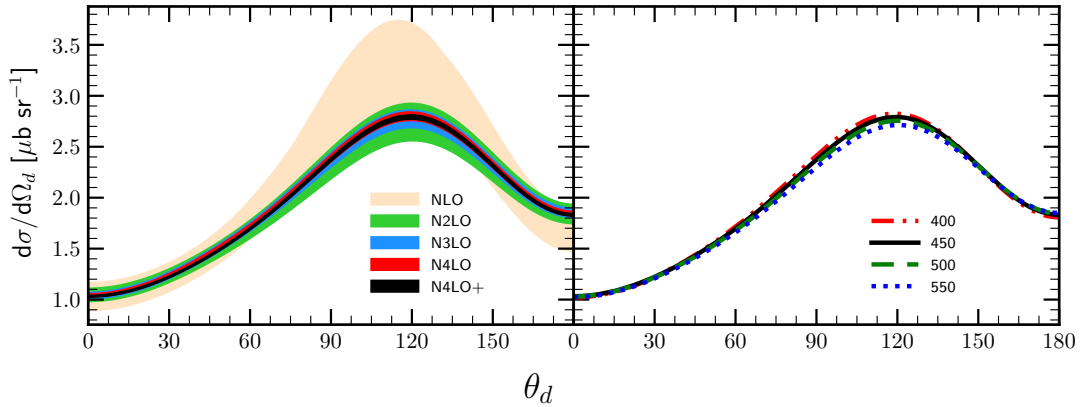
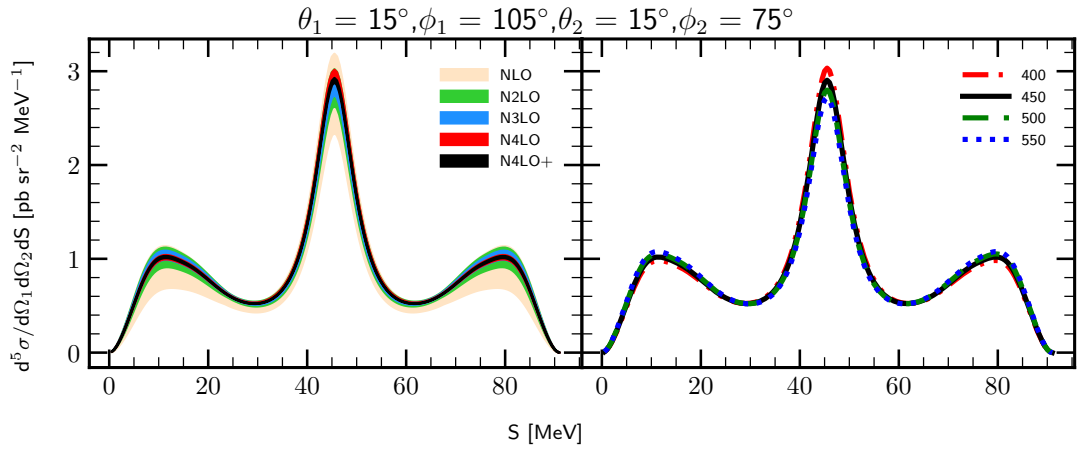Figure 3.37: The same as in the Fig. 3.36 but for the photon energy $E_\gamma = 100$ MeV

3.3 Triton photodisintegration

In this section I will discuss results for $^3\text{H} \rightarrow n + n + p$ process in the case when two neutrons are detected and similarly to the previous chapter I present the convergence of predictions and their cut-off dependence.

In the Fig. 3.38 I present a differential cross section $\frac{d^5\sigma}{d\Omega_1 d\Omega_2 dS}$ as a function of the S arc length. The photon energy is $E_\gamma = 30\,\text{MeV}$ and the kinematic configuration $\theta_1 = 15°$, $\phi_1 = 0°$, $\theta_2 = 15°$, $\phi_2 = 180°$; predictions have been obtained without 3NF. We see that only NLO and N^{2}LO introduce relatively large truncation error. The maximal width of a band for NLO is $30.95\,\%$ at $S = 10\,\text{MeV}$, for N^{2}LO it is $6.79\,\%$ at the same point and it is gradually decreasing coming to $0.10\,\%$ at N^{4}LO$^+$. The cut-off spread around maxima values is $6.25\,\%$ (at $S = 4\,\text{MeV}$) and it is $1.81\,\%$ at $S = 10\,\text{MeV}$.
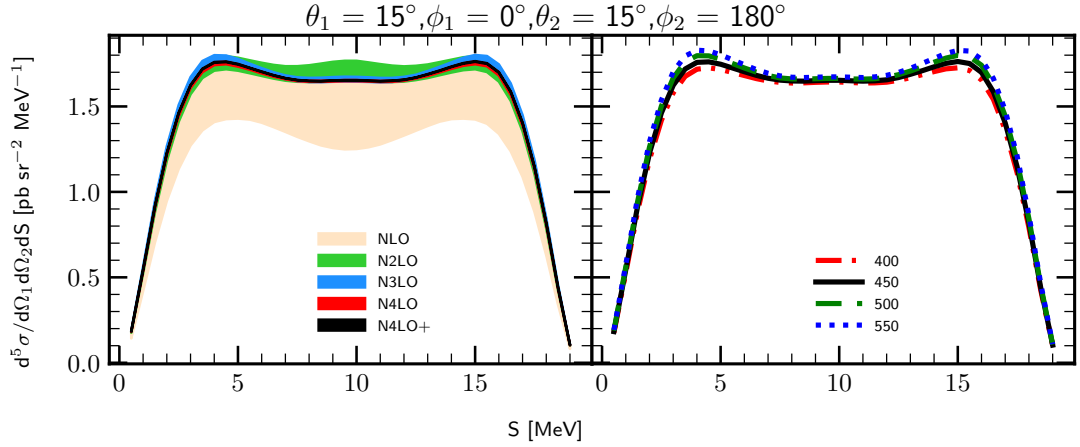
Figure 3.38: The five-fold differential cross section for the photon energy $E_\gamma = 30\,\text{MeV}$ for the kinematic configuration $\theta_1 = 15°$, $\phi_1 = 0°$, $\theta_2 = 15°$, $\phi_2 = 180°$ with two neutrons detected *check ???* . The left figure presents truncation error bands obtained using potential with chiral orders from NLO to N^{4}LO$^+$, and with cut-off parameter $\Lambda = 450\,\text{MeV}$. The right figure presents a cut-off dependence at N^{4}LO$^+$. Results are obtained with two-nucleon force only and 1NC current plus Siegert.

At bigger energy $E_\gamma = 100\,\text{MeV}$ demonstrated in the Fig. 3.39, the truncation band at the maximum point $S = 10\,\text{MeV}$ for NLO is $50.26\,\%$ decreases to $2.00\,\%$ at N^{4}LO$^+$. The cut-off spread also becomes larger with increasing energy value: $9.52\,\%$ at the same maximum.

The truncation error bands and cut-off dependance is very similar to what it was found for the three-body Helium-3 photodisintegration and the relative errors have a similar magnitudes.

Results for other angular configurations with $E_\gamma = 30\,\text{MeV}$ and at $\theta_1 = 75°$, $\phi_1 = 75°$, $\theta_2 = 75°$, $\phi_2 = 105°$ are demonstrated in Fig. 3.40. Both truncation errors and cut-off dependance are smaller at this configuration: the relative width of the truncation band at NLO is $9.39\,\%$ (at the maximum point $S = 8\,\text{MeV}$) and drops to only $0.1\,\%$ at N^{4}LO$^+$. The relative cut-off spread is $0.93\,\%$ at the same point.

At the bigger energy $E_\gamma = 100\,\text{MeV}$ demonstrated in Fig. 3.41 uncertainties grow. The truncation bands are $44.42\,\%$ and $2.09\,\%$ (at NLO and N^{4}LO$^+$ respectively) and the cut-off spread is $13.04\,\%$ (all at $S = 35\,\text{MeV}$ in maximum).

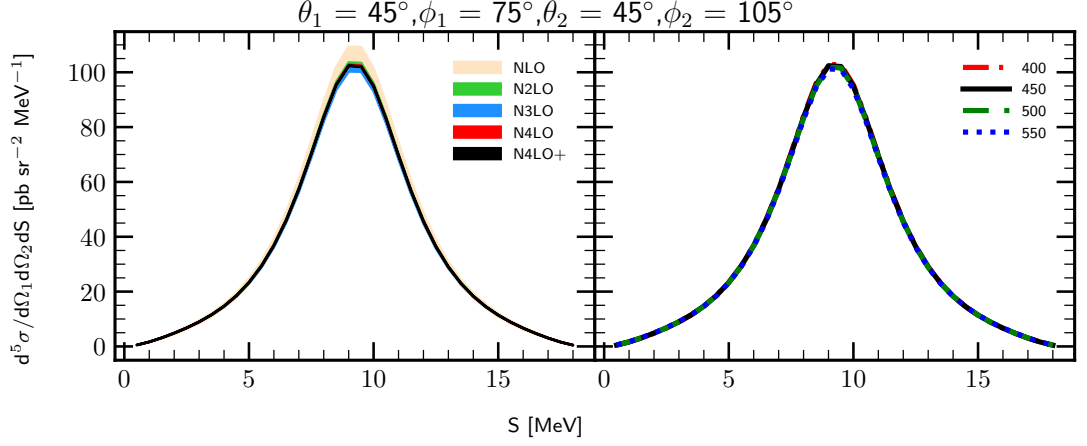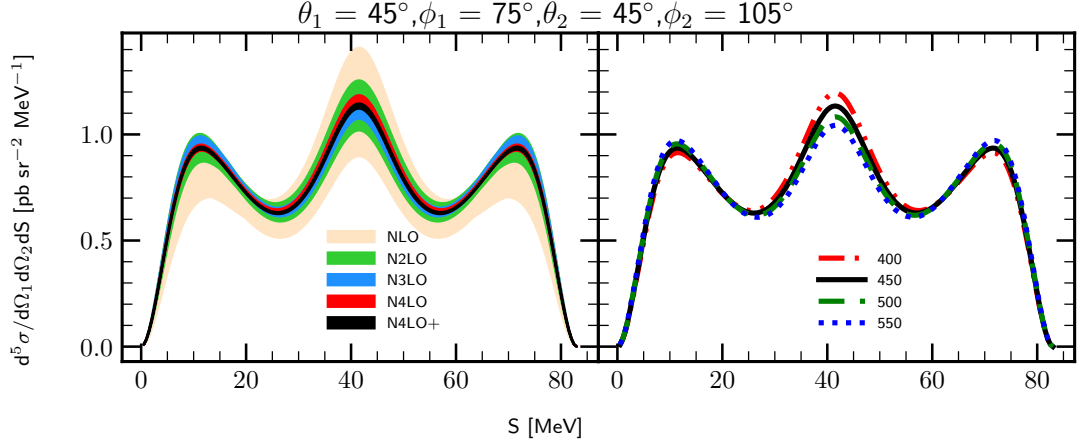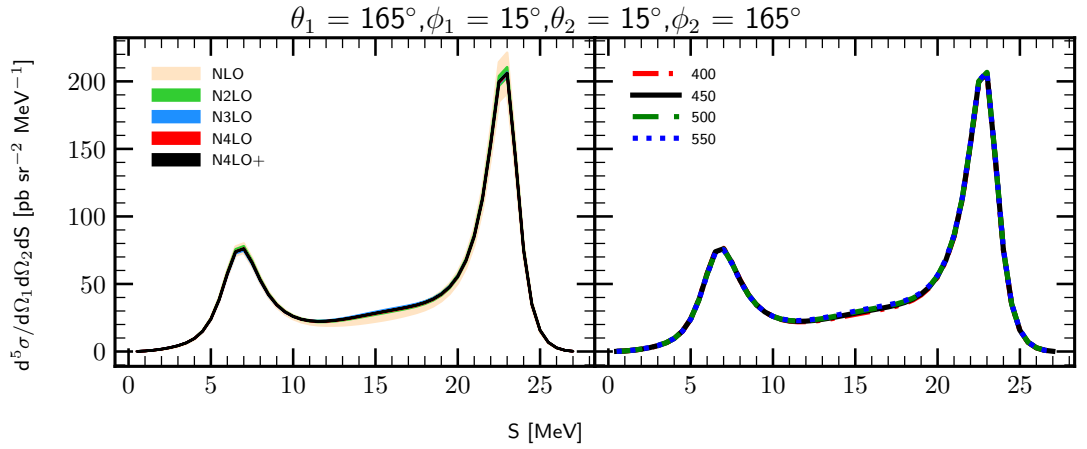Figure 3.39: The same as in the Fig. 3.38 but for the photon energy $E_\gamma = 100\,\text{MeV}$.
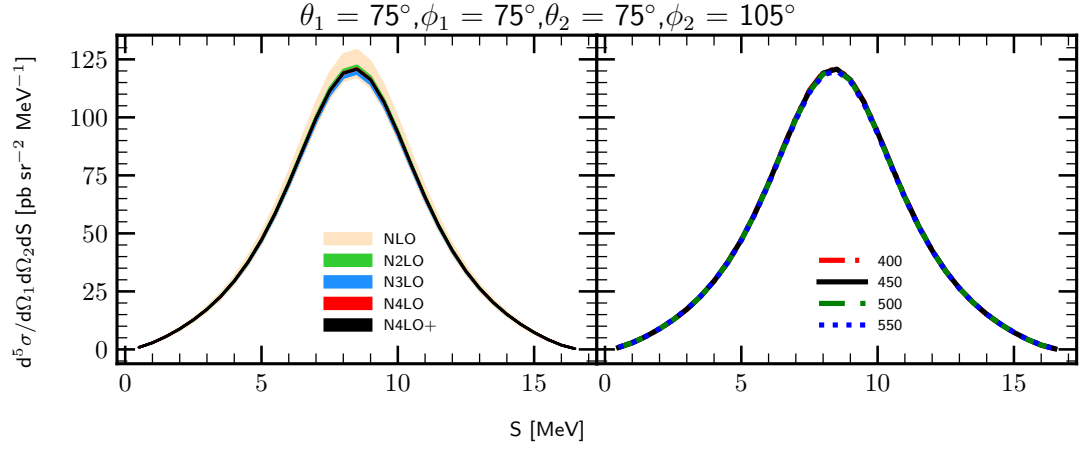
Figure 3.40: The same as in the Fig. 3.38 but for the kinematic configuration with $\theta_1 = 75°$, $\phi_1 = 75°$, $\theta_2 = 75°$, $\phi_2 = 105°$.

Similar trends are present also in other examples, demonstrated for the comparison in Figs. 3.42-3.47.
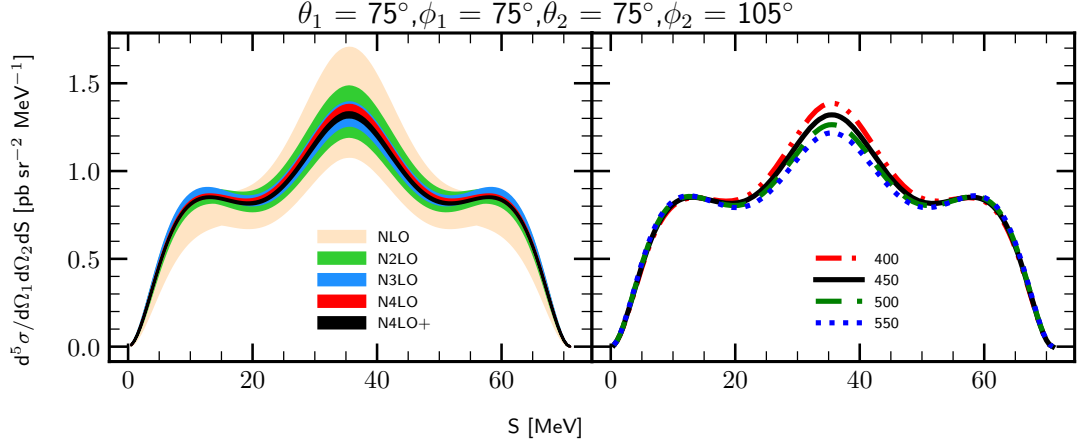
Figure 3.41: The same as in the Fig. 3.40 but for the photon energy $E_\gamma = 100\,\text{MeV}$.
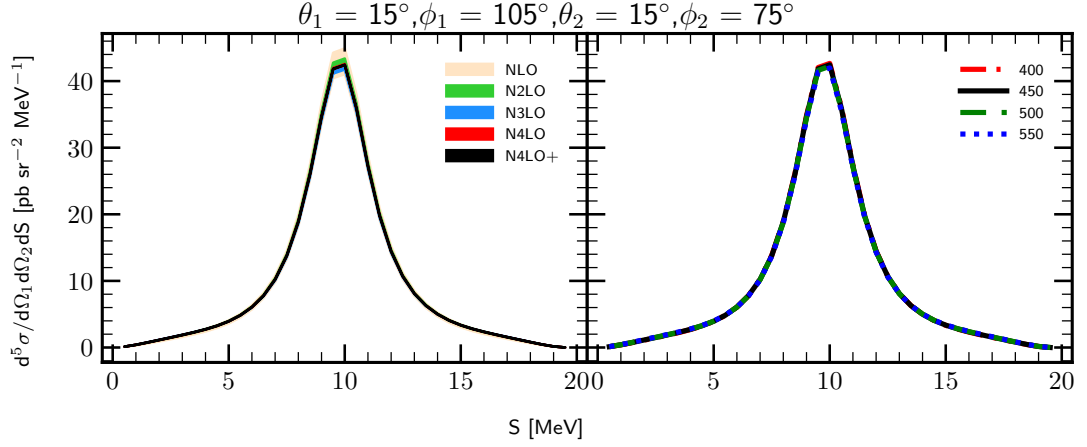
Figure 3.42: The same as in the Fig. 3.40 but for the kinematic configuration with $\theta_1 = 15°$, $\phi_1 = 105°$, $\theta_2 = 15°$, $\phi_2 = 75°$.

Figure 3.43: The same as in the Fig. 3.42 but for the photon energy $E_\gamma = 100\,\text{MeV}$.

Figure 3.44: The same as in the Fig. 3.42 but for the kinematic configuration with $\theta_1 = 45°$, $\phi_1 = 75°$, $\theta_2 = 45°$, $\phi_2 = 105°$.

Figure 3.45: The same as in the Fig. 3.44 but for the photon energy $E_\gamma = 100\,\text{MeV}$.

Figure 3.46: The same as in the Fig. 3.44 but for the kinematic configuration with $\theta_1 = 165°$, $\phi_1 = 15°$, $\theta_2 = 15°$, $\phi_2 = 165°$.
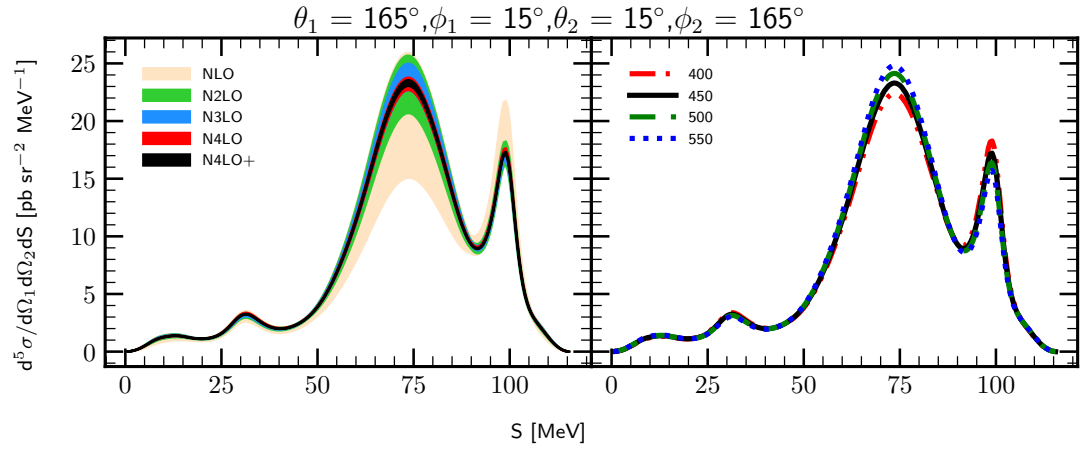
Figure 3.47: The same as in the Fig. 3.46 but for the photon energy $E_\gamma = 100\,\text{MeV}$.

3.4 Pion absorption from the lowest atomic orbital

3.4.1 Pion absorption in ^{2}H
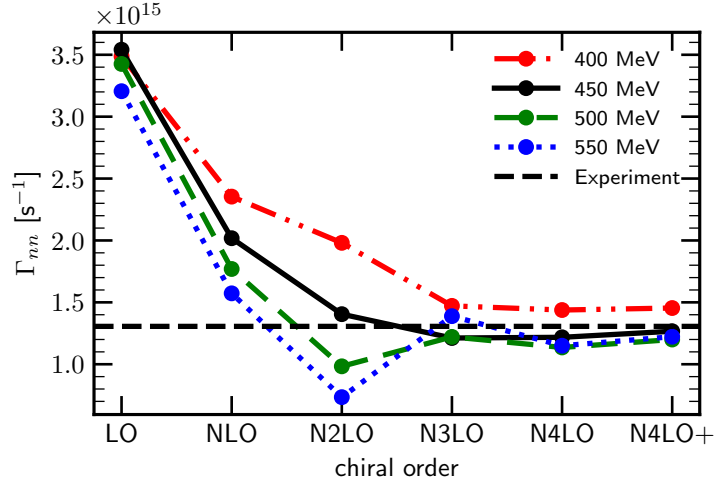
Figure 3.48: Absorption rate for the reaction $\pi^- + {}^2\text{H} \to n + n$. The rates were calculated using the SMS force with different chiral orders and cut-off values. The results were obtained using the single-nucleon transition operator and including two-nucleon contributions at the leading order. The figure shows the results obtained using plane wave (PW) plus two-neutron rescattering (Full) parts. The experimental value is obtained from the hadronic ground-state broadening in pionic deuterium [?, ?].

3.4.2 Pion absorption in ^{3}He

in Fig. 3.49 and 3.50 the pion absorption rates are presented as a function of the chiral order with different values of the cut-off parameter (for $\pi^- + {}^3\text{He} \to p + n + n$ and $\pi^- + {}^3\text{He} \to n + d$ reactions, respectively). Both figures show that with fixed chiral order the arrangement of values with respect of the cut-off parameter remains the same, namely with increasing Λ, absorption rate decreases. The only exception in both cases appears at N^{3}LO where prediction with $\Lambda = 550\,\text{MeV}$ goes above other predictions. At the next order, N^{4}LO, it corrects to the normal arrangement. This behavior may be connected to the 3NF used for the calculation and in order to check that I show a similar figure for a proton radius r_p in Fig. 3.51 calculated with and without 3NF (left and right panels respectively). Results obtained with 3NF show similar deviation at N^{3}LO while data obtained without 3NF does not have that. Nevertheless, the spread of predictions with respect to the cut-off values is much smaller with 3NF and deviation seems to be not crucial as total difference between predictions in this case is very small.

In Figs. 3.52 and 3.53 I show intensity plots for the double differential absorption rates $d^2\Gamma_{pnn}/dE_1 dE_2$ for the $\pi^- + {}^3\text{He} \to p + n + n$ process as functions of the nucleons energies (nucleon number 1 is a proton) and of Dalitz coordinates (x and y), respectively.

In Fig. 3.53 coordinates x and y are defined as:
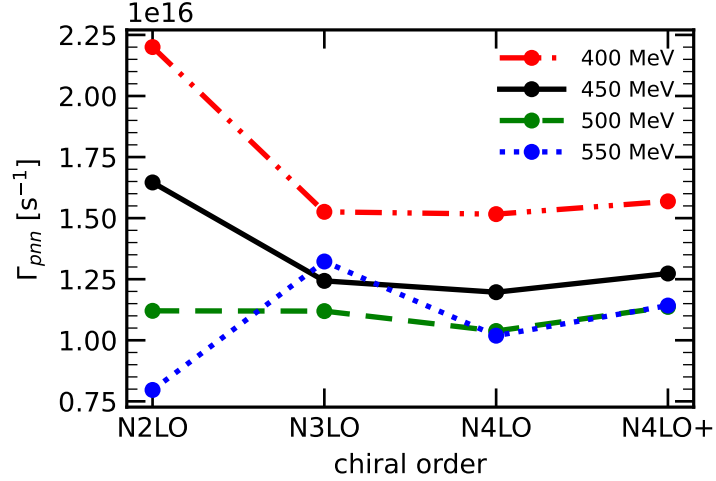
Figure 3.49: Absorption rate for $\pi^- + {}^3\text{He} \to p+n+n$ reaction as a function of the chiral order with different values of the cut-off parameter Λ. Predictions were obtained with 3NF.

$$x = 3(E_1 + 2E_2 - E)/E,$$
$$y = (3E_1 - E)/E, \tag{3.3}$$

taking the region where $r^2 \equiv x^2 + y^2 \leq 1$.

Each of two figures consists of four panels representing predictions obtained with different values of the cut-off parameter Λ. The difference between predictions which can be noticed with the naked eye - is that area of the central region (corresponding to smallest values) becomes larger with increasing Λ. It coheres to what we saw in Fig. 3.49 where total absorption rate was inversely correlated with cut-off parameter. The dominant contribution comes from the region with lowest proton energy values of $E_1 \to 0$ where both neutrons have similar large values. This is a situation when proton is a spectator while both neutrons share all energy - quasi-free scattering(QFS).

Another region with high absorption rate is neutron-neutron final state interaction (FSI(nn)). It is located at high E_1 when proton gets one third part of total energy while neutrons both get one sixth.

Next I show similar colormaps but for the predictions obtained with plane wave component only (without rescattering part) in Figs. 3.54 and 3.55. Presented plots show that the difference of predictions obtained without rescattering part with full is very large. Predicted values are few times larger and the distribution is completely different. The FSI(nn) region is not presented here in a sense that there is no peak with respect to other values. The QFS region is, on the contrary, which obviously tells us that one has to take into account rescattering pat in order to obtain relevant results.

Results obtained with Plane wave plus rescattering part and with single nucleon current only are presented in Figs. 3.56 and 3.57. As previously, each panel in figures presents predictions obtained with different values of the cut-off parameter Λ. In contrast to the configurations shown above, the change of the cut-off value has larger impact here: we see that there is a different pattern in each panel. I does not change dramatically, but two peaks inside the figure become more or less clear. On the other hand, the distribu-
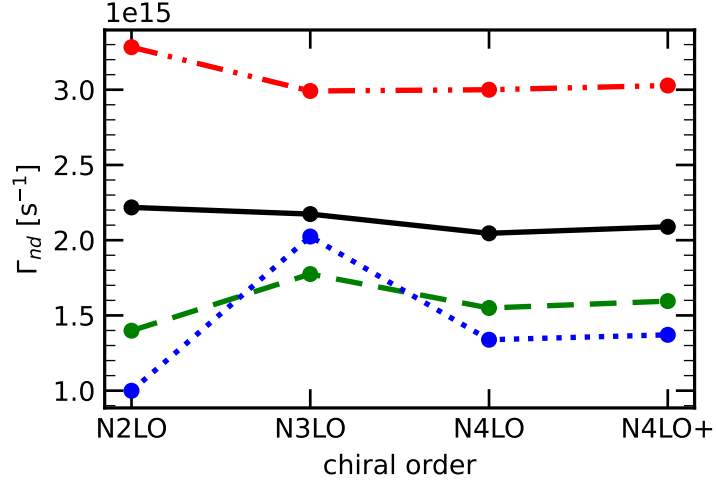
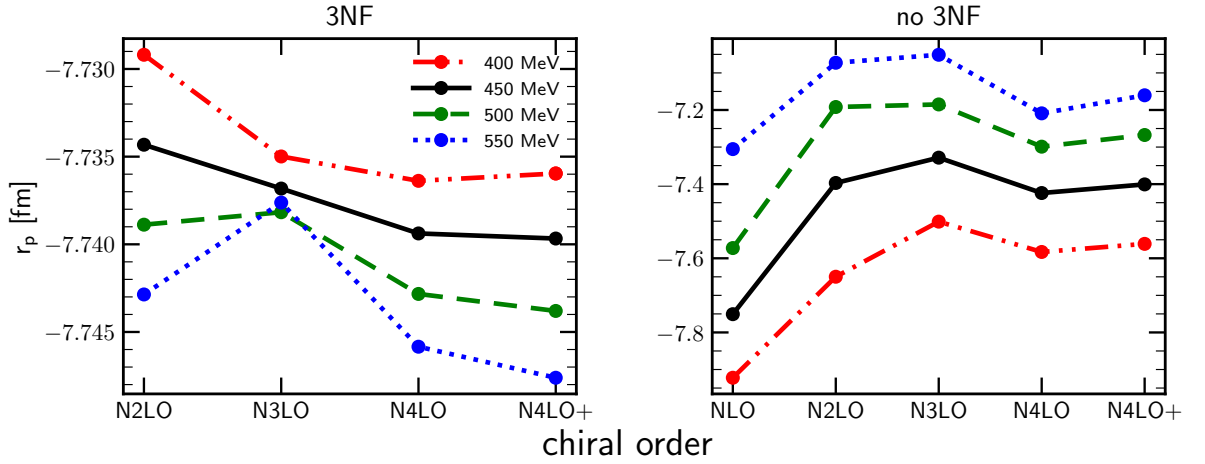Figure 3.50: The same as in Fig. 3.49, but for $\pi^- +^3\mathrm{He} \to n + d$ reaction.

Figure 3.51: *check mt3* Proton radius r_p as a function of the chiral order calculated with different values of the cut-off parameter Λ. The radius was calculated with 2NF and 3NF (left panel) and with 2NF only (right panel).

tion of the absorption rate is very different from the one, obtained with more complete components setup (Figs. 3.52 and 3.53).

Figs. 3.58 and 3.59 show prediction obtained using similar configuration as in Figs. 3.52 and 3.53, but each panel includes predictions obtained with different chiral orders of the SMS potential. We see that predictions are not sensitive to the chiral order and even $\mathrm{N^2LO}$ predictions are pretty much similar to ones obtained with the most advanced $\mathrm{N^4LO}$ potential.

Following figures demonstrate the same results but from the different prospective. Namely in Fig. 3.60 I show differential absorption rate $d\Gamma_{pnn}/d\mathrm{E}_p$ that is the same as in e.g. Fig. 3.58, but integrated over E_n. All the results are obtained with the most advanced setup (plane wave + rescattering, 1NC + 2N, 2NF+3NF). The left panel consists of the results with $\Lambda = 450\,\mathrm{MeV}$ and each curve correspond to a particular chiral order. Interesting region here is a maximum point which corresponds to a bottom part of the circles from Fig. 3.58. At the point of maximum $\mathrm{N^2LO}$ outstands from other results as its
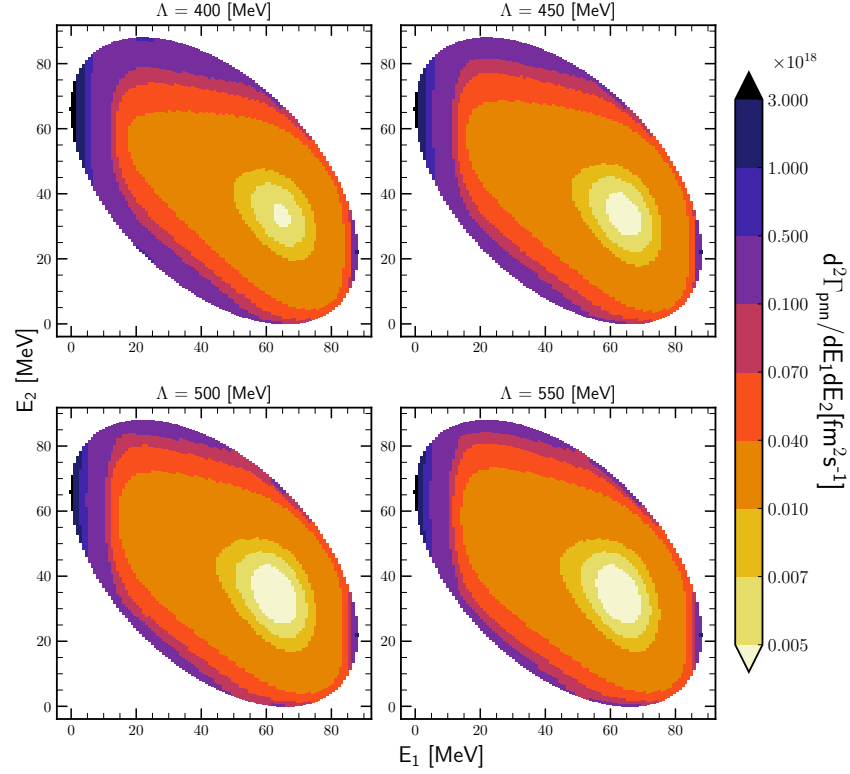
Figure 3.52: Intensity plots for the double differential absorption rates $d^2\Gamma_{pnn}/dE_1dE_2$ for the $\pi^- + {}^3\text{He} \to p + n + n$ process, obtained using the SMS potential at N^4LO^+ with all contributions possible: plane wave + rescattering, 1NC + 2N, 2NF+3NF. Each panel present predictions obtained with different values of the cut-off parameter Λ: from 400 MeV (upper left) to 550 MeV (lower right). Nucleon 1 is a proton.

point of maximum is noticeably higher. At $\text{E}_p = 0.92$ MeV (maximum point) the value of N^2LO is 1.37 times larger than one from N^4LO^+ ($3.44 \times 10^{17}\,\text{fm}\,\text{s}^{-1}$ vs $2.52 \times 10^{17}\,\text{fm}\,\text{s}^{-1}$) - the relative difference is 31.1 %. At the same time, the relative difference between all the predictions except for N^2LO is 8.3 %

The right panel of the Fig. 3.60 shows a cut-off dependance of the predictions obtained with the SMS chiral potential at N^4LO^+. In this case maximum point is interesting as well. We see that predictions with $\Lambda = 500$ MeV and 550 MeV are quite close to each other: the relative difference between them at $\text{E}_p = 0.92$ MeV is only 1.5 %. In turn the spread between $\Lambda = 400$ MeV, 450 MeV and 500 MeV is 40 % (at the same point). This cut-off dependance is hidden looking at the colormaps Fig. 3.52, but from this prospective it is clearly presented.

Similarly in Fig. 3.61 $d\Gamma_{pnn}/d\text{E}_n$ is presented. We observe similar trends which are also shown up at the extremum point which is around $\text{E}_n = 66.9$ MeV now. The difference between N^2LO and N^4LO^+ predictions at this point is 29.0 %. The relative difference between all the predictions except for N^2LO is 7.5 %. The cut-off predictions are also very similar for $\Lambda = 500$ MeV and 550 MeV (the spread is 1.6 %) while all the rest predictions are quit distinguished - the spread is 39.1 %.

Coming to the next figures Fig. 3.62 and Fig. 3.63 which show 1D dependance of the absorption rate on the Dalitz coordinates $r = \sqrt{x^2 + y^2}$ and $\phi = \arctan \frac{y}{x}$. The similar trend is preserved, namely chiral order figures show that N^2LO predictions outstand from
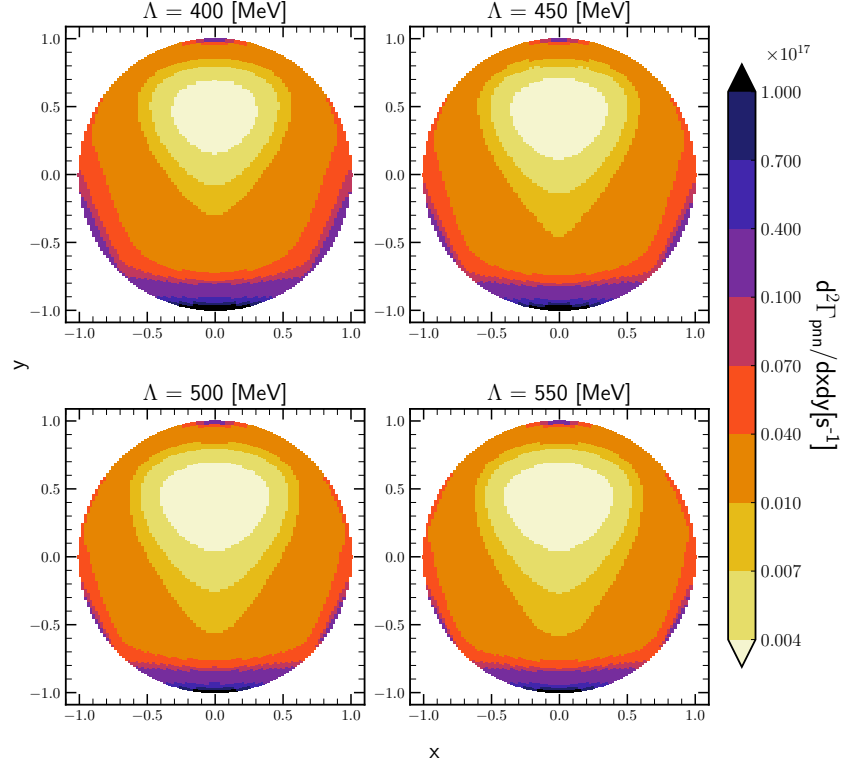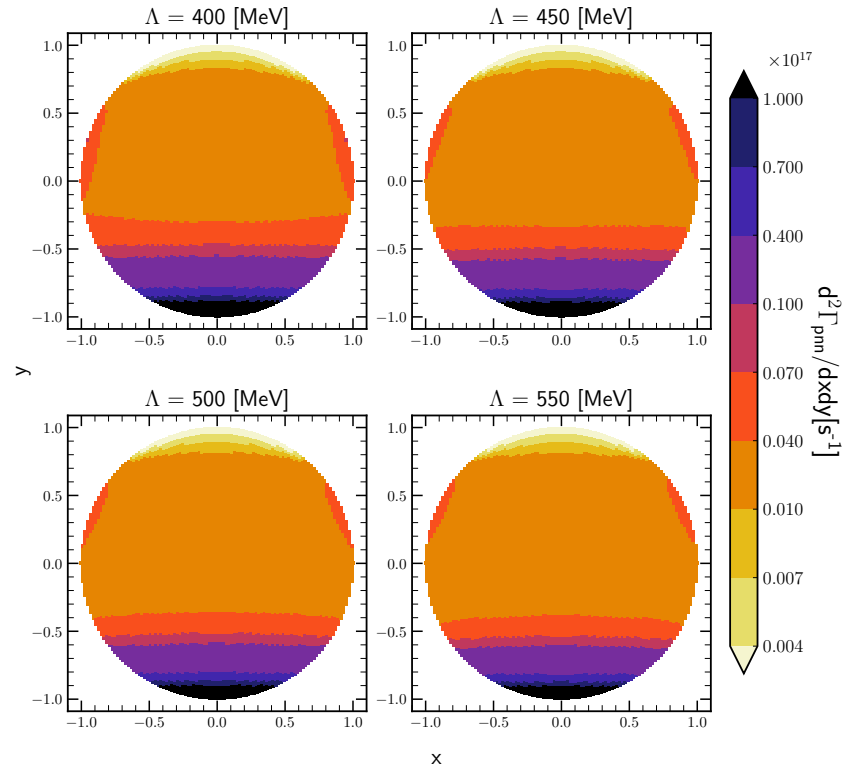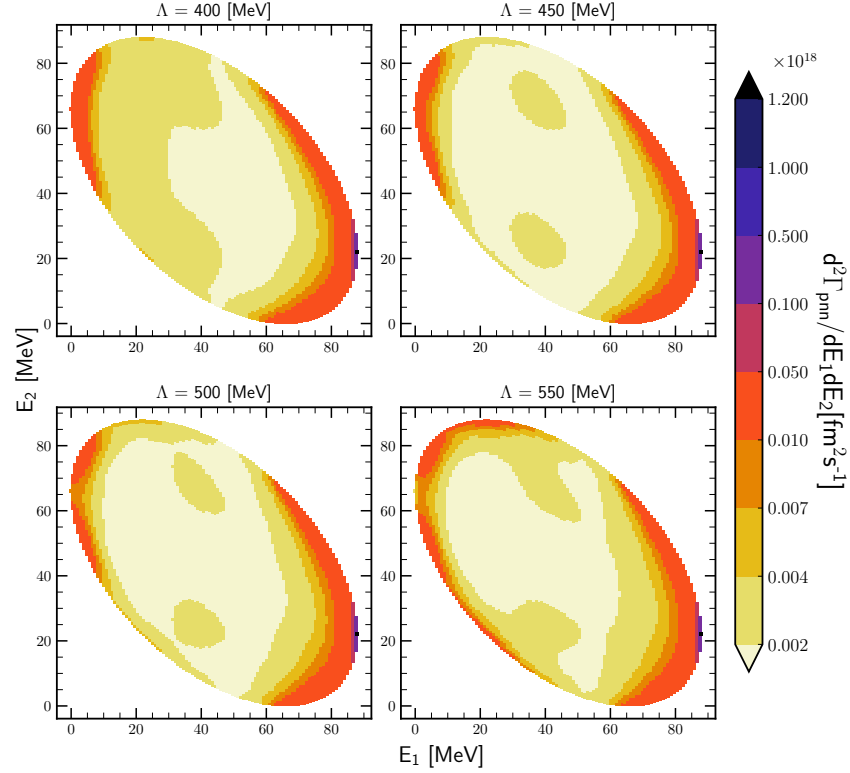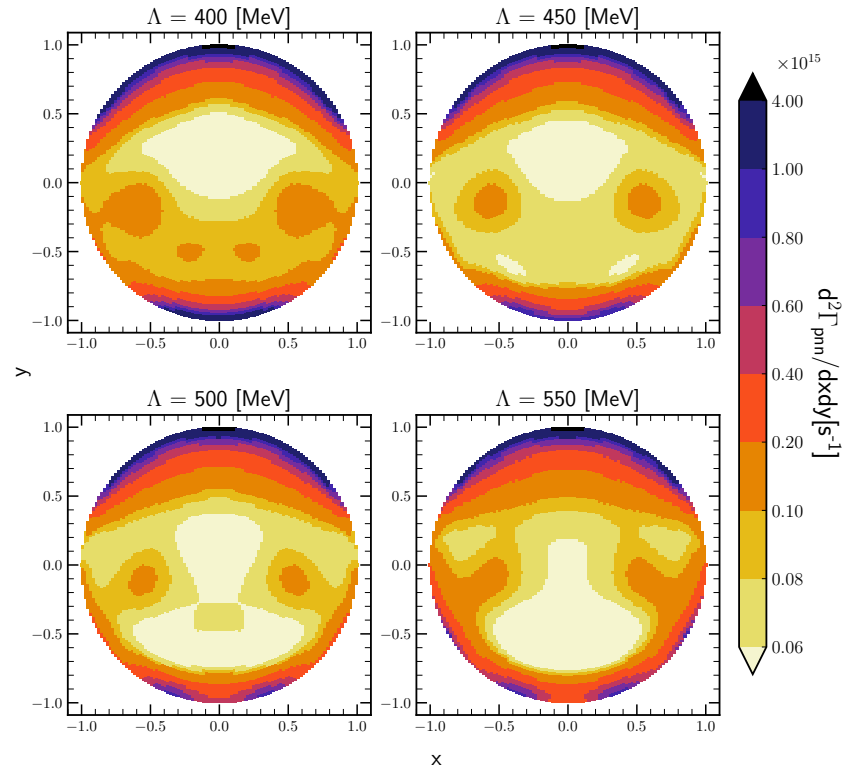
Figure 3.53: The same as in Fig. 3.52 but for the double differential absorption rates $d^2\Gamma_{pnn}/dxdy$.

all other predictions, and noticeable cut-off dependance is observed.

In general we can conclude that predictions are converged starting from the N³LO chiral order as most of the demonstrated results show that the difference between N³LO, N⁴LO and N⁴LO⁺ is negligible. At the same time we observe a cut-off dependance where predictions obtained with $\Lambda = 500\,\text{MeV}$ and $550\,\text{MeV}$ are very similar, but the spread with all the rest values is there. This nature of the cut-off dependance is also reflected in the total absorption rate, presented in Fig. 3.49.
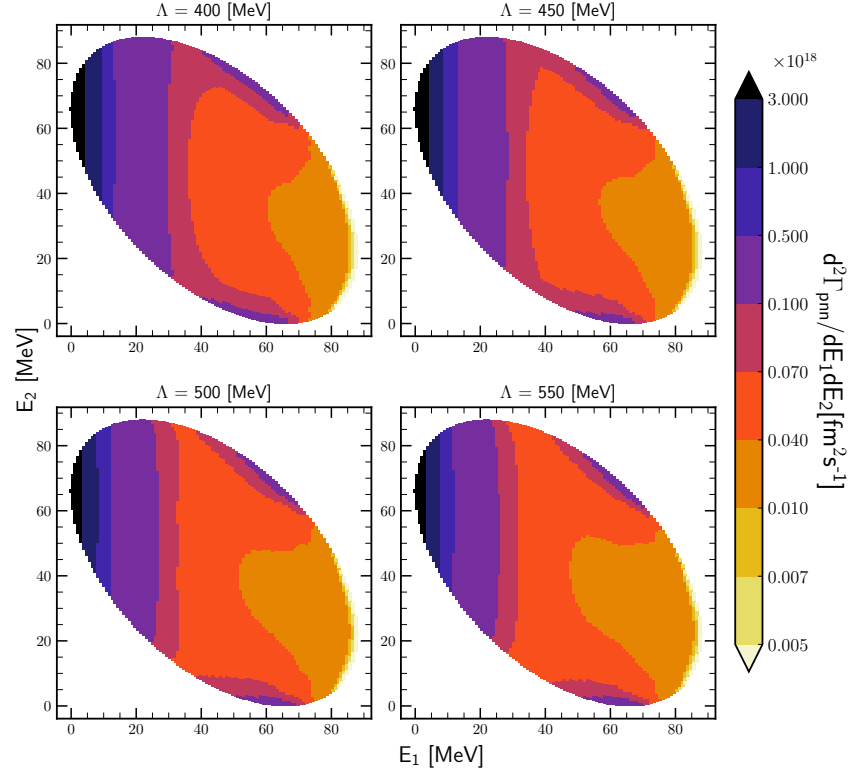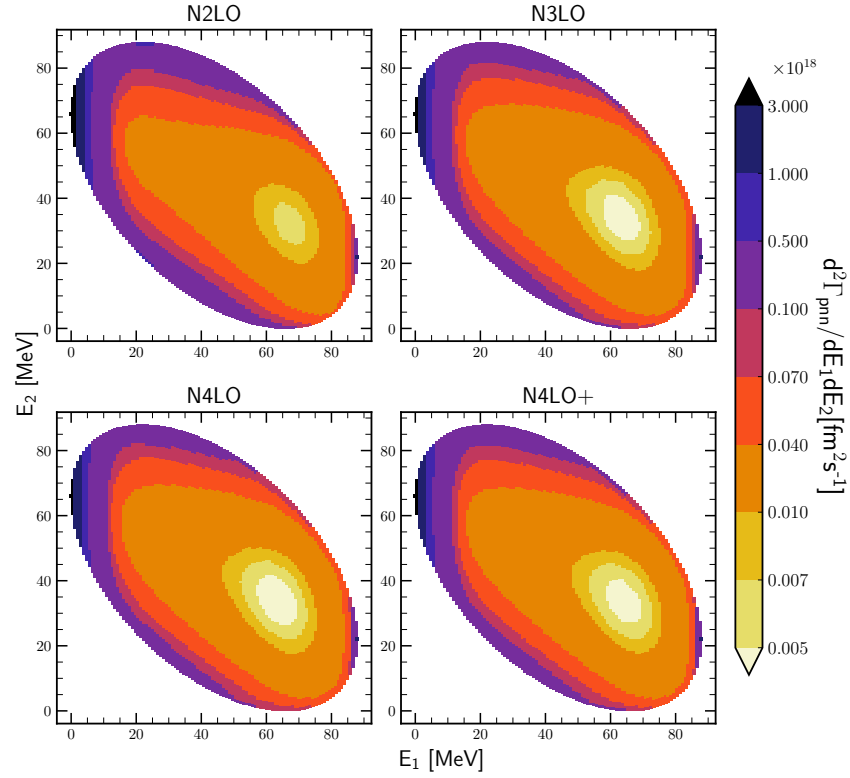
Figure 3.54: Intensity plots for the double differential absorption rates $d^2\Gamma_{pnn}/dE_1dE_2$ for the $\pi^- +^3$ He $\rightarrow p + n + n$ process, obtained using the SMS potential at N^{4}LO$^+$ with plane wave part only (without rescattering). All other contributions are the same as in Fig. 3.52: 1NC + 2N and 2NF+3NF. Each panel present predictions obtained with different values of the cut-off parameter Λ: from $400\,\mathrm{MeV}$ (upper left) to $550\,\mathrm{MeV}$ (lower right). Nucleon 1 is a proton.
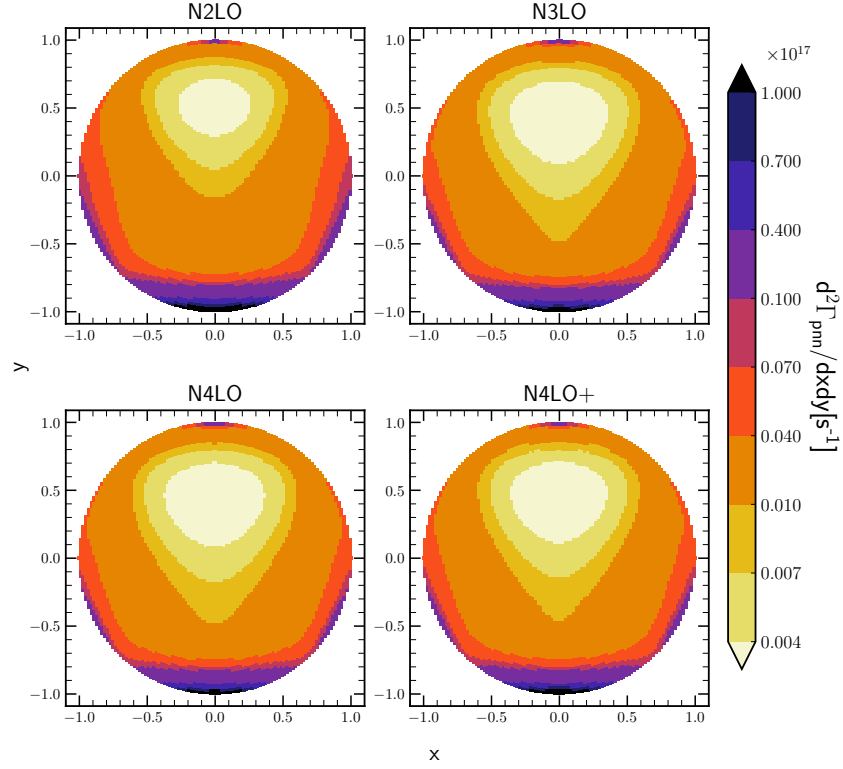
Figure 3.55: The same as in Fig. 3.54 but for the double differential absorption rates $d^2\Gamma_{pnn}/dxdy$.

Figure 3.56: Intensity plots for the double differential absorption rates $d^2\Gamma_{pnn}/dE_1dE_2$ for the $\pi^- + {}^3\text{He} \to p + n + n$ process, obtained using the SMS potential at N^{4}LO$^+$ with 1NC only (without 2N). All other contributions are the same as in Fig. 3.52: PWIAS+RESC and 2NF+3NF. Each panel present predictions obtained with different values of the cut-off parameter Λ: from 400 MeV (upper left) to 550 MeV (lower right). Nucleon 1 is a proton.

Figure 3.57: The same as in Fig. 3.56 but for the double differential absorption rates $d^2\Gamma_{pnn}/dxdy$.

Figure 3.58: Intensity plots for the double differential absorption rates $d^2\Gamma_{pnn}/dE_1dE_2$ for the $\pi^- + ^3\mathrm{He} \to p + n + n$ process, obtained using the SMS potential at N^{4}LO$^+$ with all contributions possible: plane wave + rescattering, 1NC + 2N, 2NF+3NF. Each panel present predictions obtained with different chiral orders of the SMS potential: from N^{2}LO (upper left) to N^{4}LO$^+$ (lower right) and with $\Lambda = 450\,\mathrm{MeV}$. Nucleon 1 is a proton.

Figure 3.59: The same as in Fig. 3.58 but for the double differential absorption rates $d^2\Gamma_{pnn}/dxdy$.
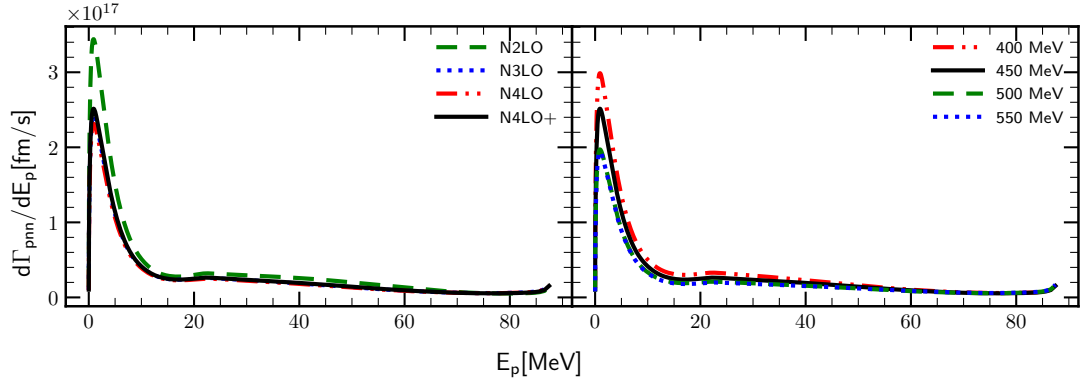
Figure 3.60: Differential absorption rate $d\Gamma_{pnn}/dE_p$ as a function of the proton energy E_p for the $\pi^- + 3\text{He} \rightarrow p + n + n$ process. Left panel shows results obtained with N^{2}LO (green dashed line), N^{3}LO (blue dotted line), N^{4}LO (red dashed-double-dotted line) and N^{4}LO$^+$ (black solid line) chiral orders, and with $\Lambda = 450\,\text{MeV}$. The right panel includes results obtained with the N^{4}LO$^+$ SMS potential with different values of the Λ: $400\,\text{MeV}$ (red dashed-double-dotted line), Λ: $450\,\text{MeV}$ (black solid line), Λ: $500\,\text{MeV}$ (green dashed line line) and Λ: $550\,\text{MeV}$ (blue dotted line). All predictions were obtained with "FULL-(1NC+2N)-(2NF+3NF)" setup.
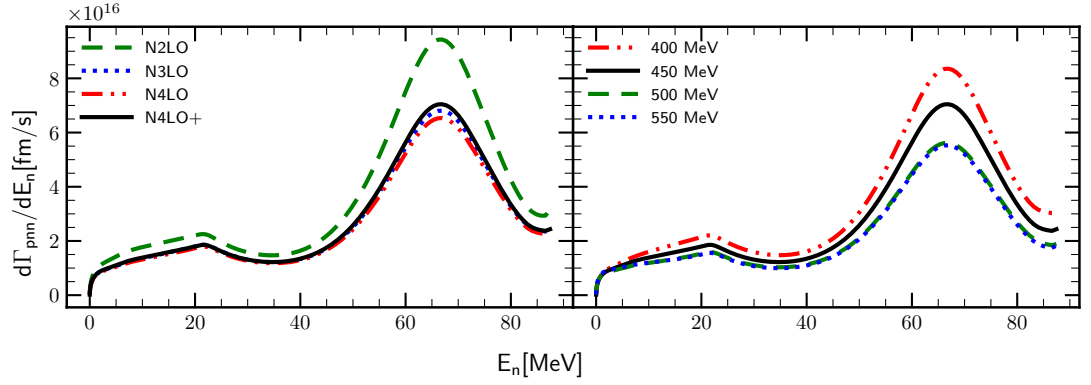
Figure 3.61: The same as in Fig. 3.60 but for the differential absorption rate $d\Gamma_{pnn}/dE_n$ as a function of the neutron energy E_n.
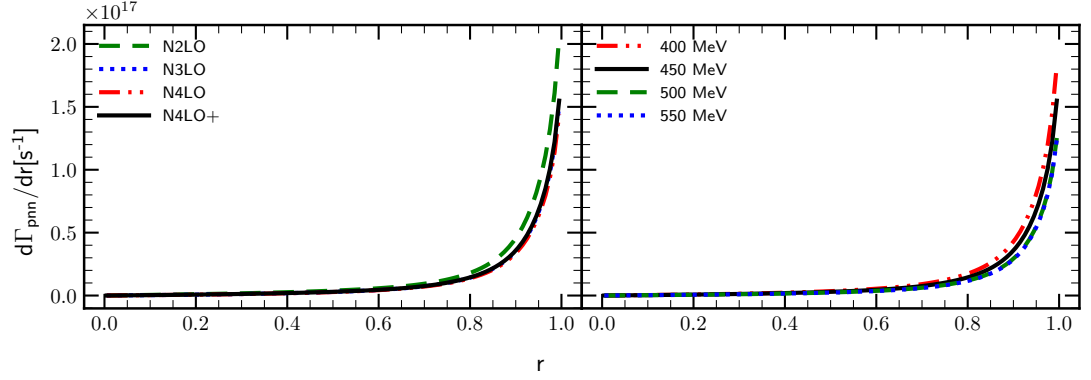
Figure 3.62: The same as in Fig. 3.60 but for the differential absorption rate $d\Gamma_{pnn}/dr$ as a function of the parameter r of the Dalitz coordinates: $r = \sqrt{x^2 + y^2}$.
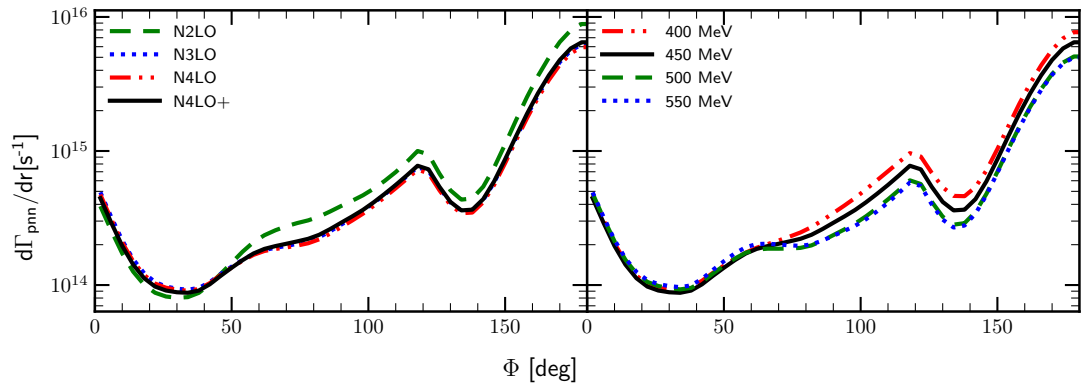

Figure 3.63: The same as in Fig. 3.62 but for the differential absorption rate $d\Gamma_{pnn}/d\phi$ as a function of the azimuthal angle ϕ of the Dalitz coordinates: $\phi = \arctan\frac{y}{x}$.

3.4.3   Pion absorption in ^{3}H

In this subsection I will show results of calculations for the $\pi^- +^3\mathrm{H} \to n+n+n$ process. In this case we have only a three-body breakup as no two-body configuration can be composed out of three neutrons.

The total absorption rate $\pi^- +^3\mathrm{H} \to n+n+n$ is shown in Fig. 3.64 as a function on the chiral order of the SMS potential while each curve represents different cut-off values used to obtain the prediction. THe most advanced configuration was used in this case, namely Plane wave plus rescattering part, both single- and two-nucleon currents and two-nucleon plus three-nucleon forces.

Similarly to the process with ^{3}He, we see that with each subsequent chiral order predictions become closer to each other, so cut-off dependence gets weaker. Also, the prediction with $\Lambda = 550\,\mathrm{MeV}$ at N^{3}LO is strangely above the prediction with $\Lambda = 500\,\mathrm{MeV}$. We can also notice, that at N^{4}LO predictions with cut-off values $500\,\mathrm{MeV}$ and $550\,\mathrm{MeV}$ are much closer to each other than to other values.
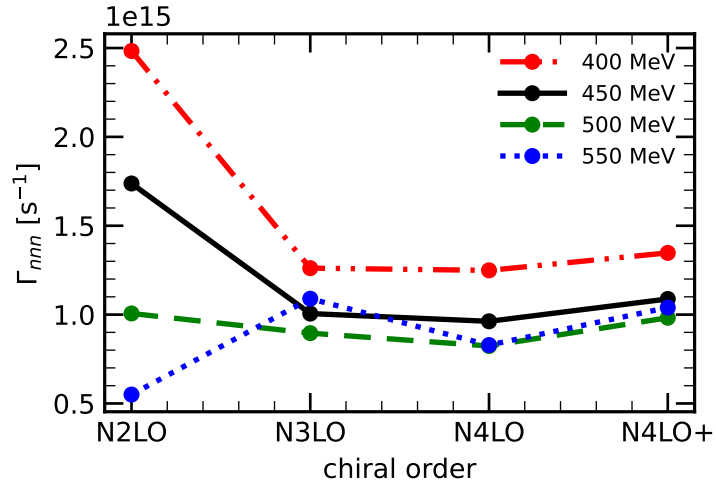

Figure 3.64: Absorption rate for $\pi^- +^3\mathrm{H} \to n+n+n$ reaction as a function of the chiral order with different values of the cut-off parameter Λ. Predictions were obtained with 3NF.
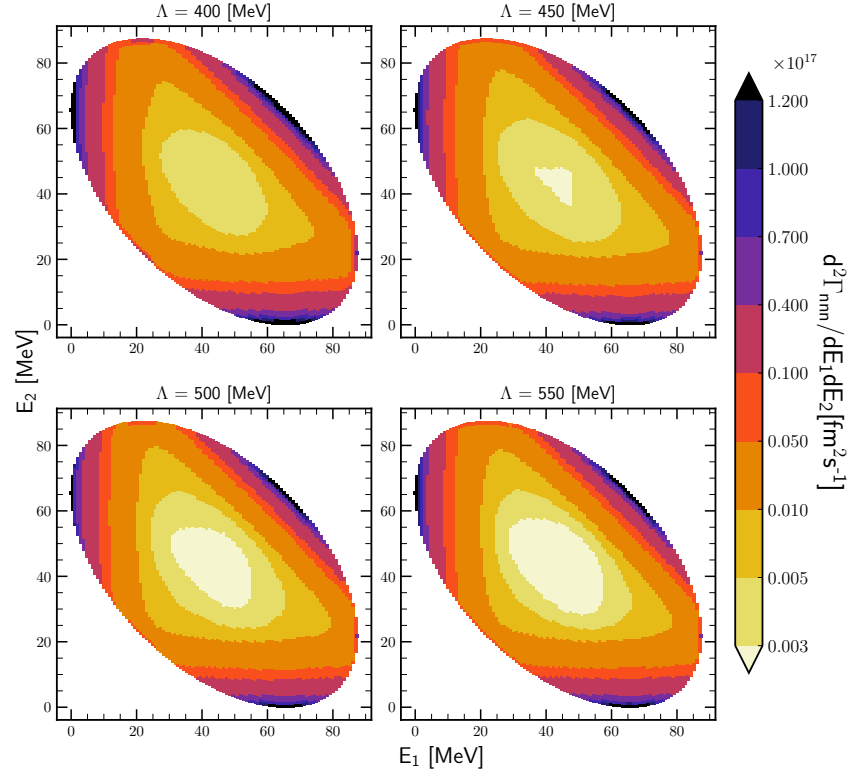
Figure 3.65: Intensity plots for the double differential absorption rates $d^2\Gamma_{nnn}/dE_1dE_2$ for the $\pi^- + {}^3\mathrm{H} \to n + n + n$ process, obtained using the SMS potential at $\mathrm{N^4LO^+}$ with all contributions possible: plane wave + rescattering, 1NC + 2N, 2NF+3NF. Each panel present predictions obtained with different values of the cut-off parameter Λ: from 400 MeV (upper left) to 550 MeV (lower right).
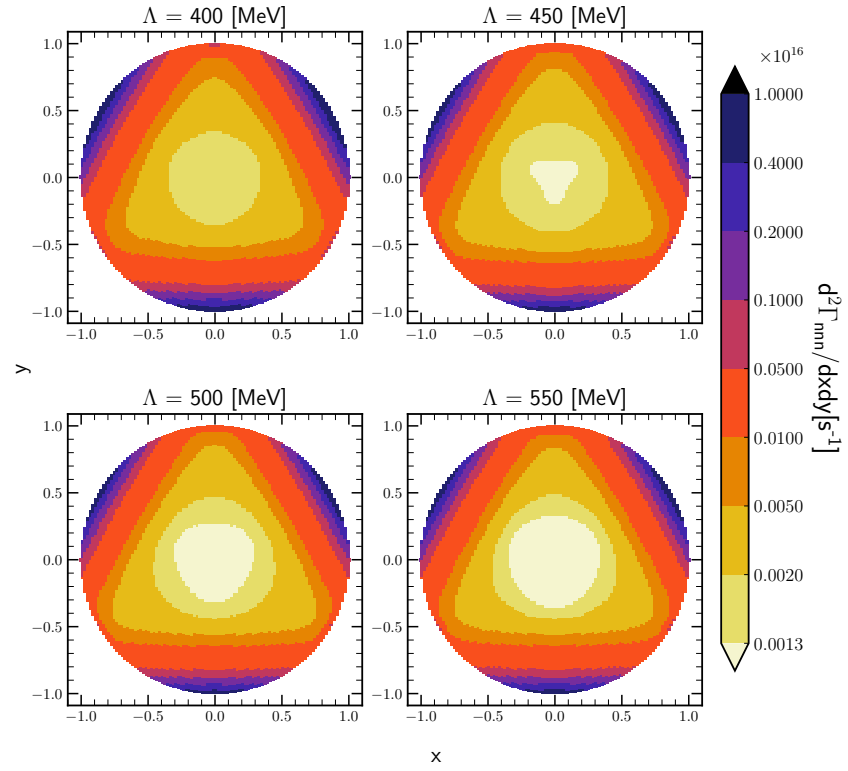
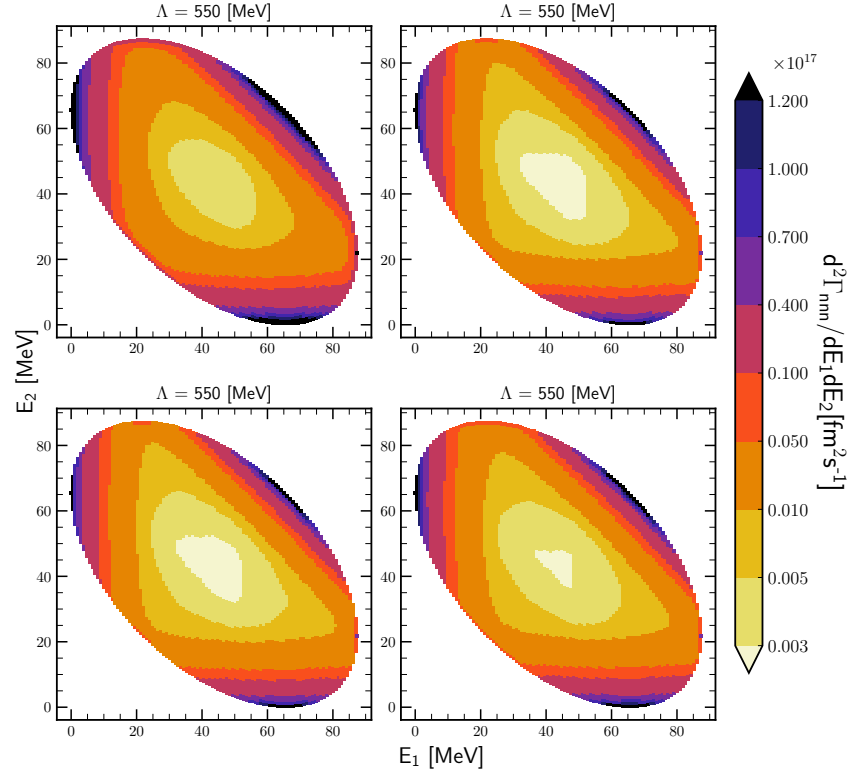Figure 3.66: The same as in Fig. 3.65 but for the double differential absorption rates $d^2\Gamma_{nnn}/dxdy$.

Figure 3.67: Intensity plots for the double differential absorption rates $d^2\Gamma_{nnn}/dE_1dE_2$ for the $\pi^- +^3\text{H} \to n + n + n$ process, obtained using the SMS potential at N^4LO^+ with all contributions possible: plane wave + rescattering, 1NC + 2N, 2NF+3NF. Each panel present predictions obtained with different chiral orders of the SMS potential: from N^2LO (upper left) to N^4LO^+ (lower right) and with $\Lambda = 450\,\text{MeV}$.
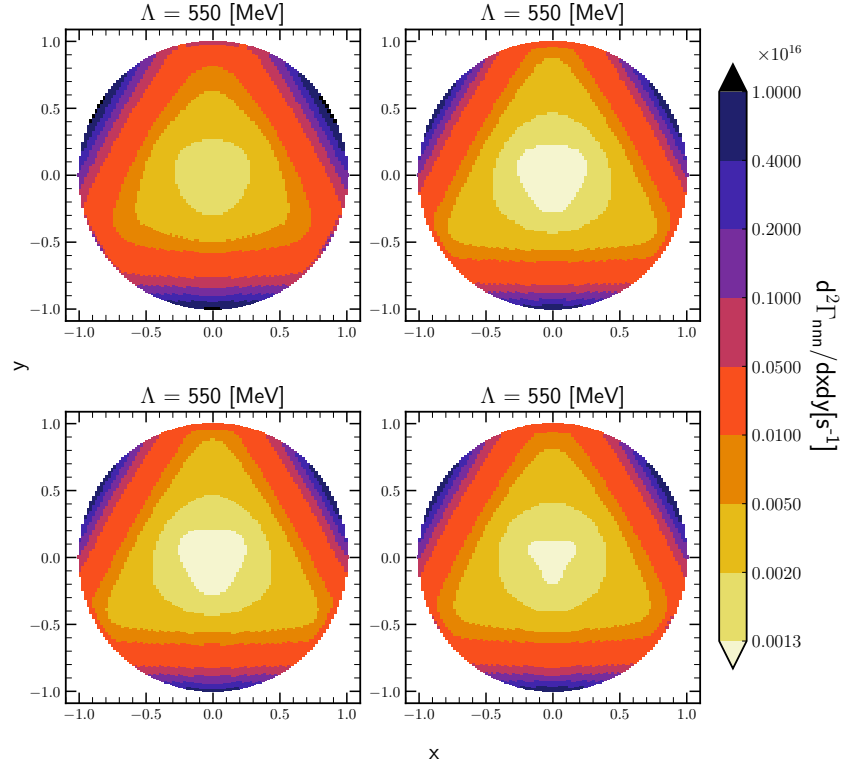
Figure 3.68: The same as in Fig. 3.67 but for the double differential absorption rates $d^2\Gamma_{nnn}/dxdy$.
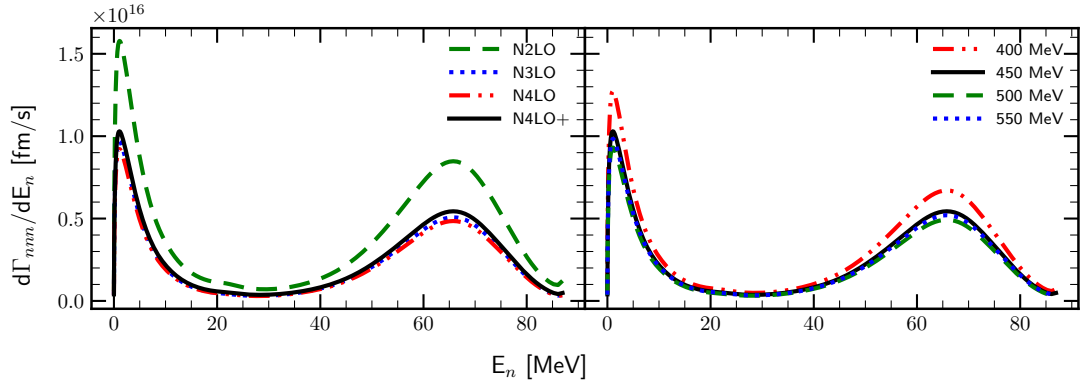

Figure 3.69: Differential absorption rate $d\Gamma_{nnn}/dE_n$ as a function of the neutron energy E_n for the $\pi^- + 3H \rightarrow n + n + n$ process. Left panel shows results obtained with N^2LO (green dashed line), N^3LO (blue dotted line), N^4LO (red dashed-double-dotted line) and N^4LO^+ (black solid line) chiral orders, and with $\Lambda = 450\,MeV$. The right panel includes results obtained with the N^4LO^+ SMS potential with different values of the Λ: 400 MeV (red dashed-double-dotted line), Λ: 450 MeV (black solid line), Λ: 500 MeV (green dashed line line) and Λ: 550 MeV (blue dotted line). All predictions were obtained with "FULL-(1NC+2N)-(2NF+3NF)" setup.
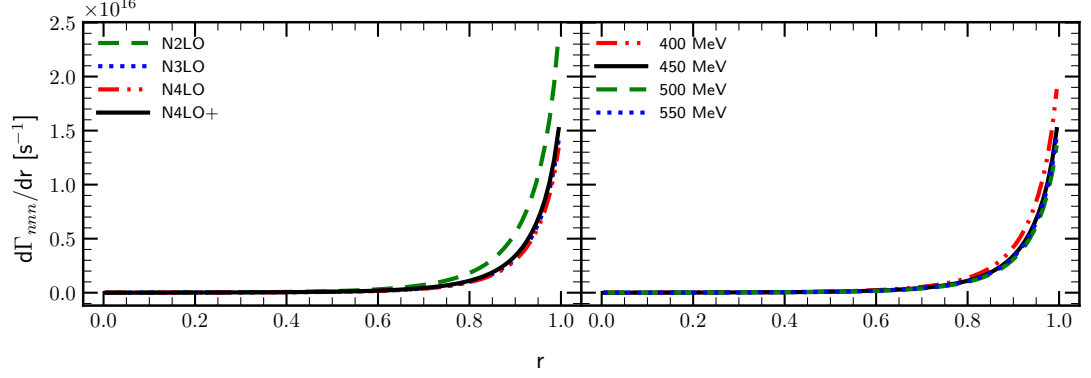
Figure 3.70: The same as in Fig. 3.69 but for the differential absorption rate $d\Gamma_{nnn}/dr$ as a function of the parameter r of the Dalitz coordinates: $r = \sqrt{x^2 + y^2}$.
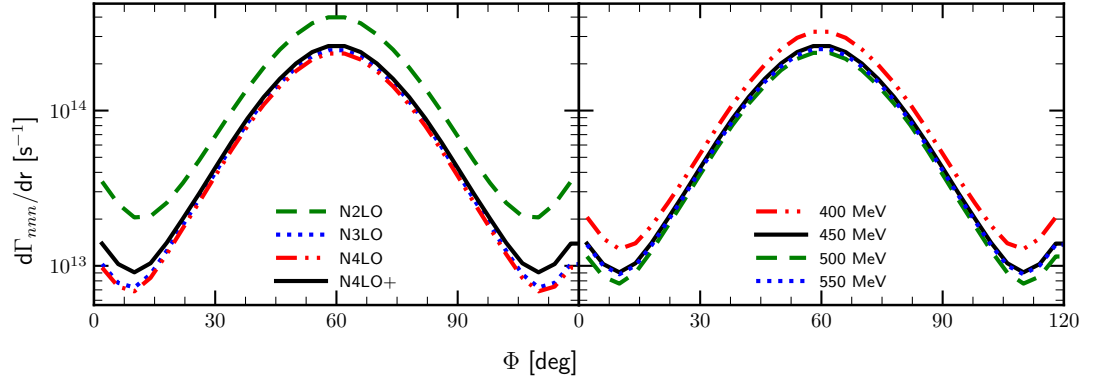

Figure 3.71: The same as in Fig. 3.70 but for the differential absorption rate $d\Gamma_{nnn}/d\phi$ as a function of the azimuthal angle ϕ of the Dalitz coordinates: $\phi = \arctan \frac{y}{x}$.

CHAPTER 4

SUMMARY

In this thesis I investigated ^{2}H, ^{3}H and ^{3}He photodisintegrations as well as pion absorption by the same nuclei. In order to analyze these reactions and calculate predictions for observables I used a chiral model of interaction namely the most advanced SMS chiral potential up to N^{4}LO$^+$ order. Results prepared with AV18 potential have been shown as a reference point.

The first goal of this work was to investigate if the SMS potential is converged with respect to the chiral order. It would then be a hint whether the development of higher orders is required. In most of the results we observed a very converged predictions which was confirmed by a small difference between the last two chiral orders: N^{4}LO and N^{4}LO$^+$. This difference in most of regarded situations did not exceed a few percent. Another evidence is a width of the truncation band for N^{4}LO$^+$ predictions. For the deuteron photodisintegration process, observables have a maximum width always below 1% for the regarded photon energies ($E_\gamma = 30\,\text{MeV}$ and $E_\gamma = 100\,\text{MeV}$). The same trend is presented also for other regarded reactions as well. This hints us towards a conclusion that further chiral orders would not improve the predictions much and current potential is converged already. This is also confirmed by the AV18 predictions which are always very close to N^{4}LO$^+$ (see e.g. Fig. 3.8, Fig. 3.26 etc.).

The other interesting point in the investigated chiral potential is its dependance on the value of the cutoff parameter Λ, the four values of which (400, 450, 500 and 550 MeV) were investigated. We have observed that the relative spread of predictions with respect to the cutoff value is higher for the larger energies. For example the spread of the differential cross section for ^{3}He photodisintegration at $E_\gamma = 30\,\text{MeV}$ at the characteristic point (maximum) is around 3% while at $E_\gamma = 100\,\text{MeV}$ it is three times larger - around 3% (see Fig. 3.28, Fig. 3.29 and discussions). Nevertheless, usually for higher energies the difference between the predictions obtained with different values of Λ is smaller than the difference with experimental data (when it is available) which is evidently visible in Fig. 3.5(b).

We have also checked contributions from the various model components to the predicted values. Namely, predictions obtained with plane wave part only (first term in the Eq. (2.31)), as well as predictions with and without 2N current contributions (obtained via the Siegert approach). For example, in the Fig. 3.4b we see predictions for the deuteron photodisintegration obtained without rescattering part(pink line), without 2N contributions (green line) and full predictions (blue line). Evidently the rescattering

part contribution is relatively small for the $E_\gamma = 30\,\text{MeV}$, but is increasing with larger energies. The analysis of the relative difference at the specific θ_p value does not show this trend (the differences are $10\,\%$, $7\,\%$ and $4\,\%$ for $E_\gamma = 30$, 100 and $140\,\text{MeV}$ respectively at $\theta_p = 80\,\%$), but we see that at the lower energy curves are qualitatively very similar and the difference is mainly around the maximum point(which is close to the analyzed point). In contrast, for the larger energies, curves differ qualitatively and analyzed point is rather depicting the region were the difference is minimal. The difference between the full predictions and the ones, where only 1NC was used is much higher: even for the lowest energy it is around $50\,\%$ and for the larger two it grows up to $\sim 78\,\%$ (at the same angle value). Clearly, both rescattering part and 2NC contributions are very important and bring significant contribution. The latter one is taken into account not completely, since there is no proper 2NC current available yet, but even using the Siegert approach proves that this part is very important in described process. Similar trend is visible at other observables(see e.g. Fig. 3.10) and other processes (see Figs.3.52, 3.54, 3.56 to compare contributions for the pion absorption at ${}^3\text{He}$).

Giving mentioned above results, we can conclude that current version of the chiral potential is good: it rather does not require any additional development in a sens of chiral orders or regularization, but 2NC is expected to bring a large improvements to the predictions.

Our Full model nicely describes data up to $E_\gamma = 70\,\text{MeV}$.